Investigations of Structure and Dynamics at Phase Transitions of Various Types

A Thesis

Submitted for the Degree of

DOCTOR OF PHILOSOPHY

in the Faculty of Science

by

Jiarul Midya

THEORETICAL SCIENCES UNIT
JAWAHARLAL NEHRU CENTRE FOR ADVANCED SCIENTIFIC RESEARCH
Bangalore – 560 064

FEBRUARY 2017

To my family

DECLARATION

I hereby declare that the matter embodied in the thesis entitled "**Investigations of Structure and Dynamics at Phase Transitions of Various Types**" is the result of investigations carried out by me at the Theoretical Sciences Unit, Jawaharlal Nehru Centre for Advanced Scientific Research, Bangalore, India under the supervision of Prof. Subir K. Das and that it has not been submitted elsewhere for the award of any degree or diploma.

In keeping with the general practice in reporting scientific observations, due acknowledgement has been made whenever the work described is based on the findings of other investigators.

Jiarul Midya

20.02.2017

Jiarul Midya

CERTIFICATE

I hereby certify that the matter embodied in this thesis entitled "**Investigations of Structure and Dynamics at Phase Transitions of Various Types**" has been carried out by Mr. Jiarul Midya at the Theoretical Sciences Unit, Jawaharlal Nehru Centre for Advanced Scientific Research, Bangalore, India under my supervision and that it has not been submitted elsewhere for the award of any degree or diploma.

20.02.2017

Prof. Subir K. Das
(Research Supervisor)

Acknowledgements

I would like to take this opportunity to acknowledge the contributions of individuals who helped shaping my career in academics.

First and foremost, I would like to express my warmest gratitude towards my thesis supervisor Prof. Subir K. Das, for giving me the opportunity to pursue Ph.D. with him at the Jawaharlal Nehru Centre for Advanced Scientific Research (JNCASR). I would like to thank him for his kind help, inspiration, important suggestions and careful guidance throughout my Ph.D. years. He introduced me to a diverse set of problems and provided the environment of academic freedom. Working with him was really a great experience.

I would like to acknowledge Prof. Jürgen Horbach with whom a collaboration has recently started. Insights on important simulation techniques that I gained from discussions with him will be useful in future.

Acknowledgements are due to all the faculty members of Theoretical Sciences Unit (TSU) - Prof. Swapan K. Pati, Prof. N.S. Vidhyadhiraja, Prof. Kavita Jain, Prof. Shobhana Narasimhan, Prof. Umesh V. Waghmare, Prof. K.B. Sinha, Prof. Srikanth Sastry and Dr. Meher K. Prakash. I benefited from various scientific and nonscientific discussions with them.

I am grateful to all my course instructors from JNCASR - Prof. Subir K. Das, Prof. Swapan K. Pati, Prof. N.S. Vidhyadhiraja, Prof. Kavita Jain, Prof. Shobhana Narasimhan, Prof. Umesh V. Waghmare, Prof. Balasubramanian and Prof. Rajesh Ganapathy. Lessons learned from their courses were useful in my research work.

Sincere thanks to my former teacher Mr. Debasis Bhattacharyya, for his constant inspiration. He has always been available to provide me directions and inspired me to study physics. I am also grateful to all my school teachers. Particular mention must be made of Mr. Swapan Kumar Ghosh, Mr. Sandeep Basani, Mr. Abhijit Bhattacharyya, Mr. Subimol Chakraborty, Mr. Biswanath Kundu and Mr. Lakshan Ruidas, who motivated me to pursue science.

I am thankful to all JNCASR staff members, from Complab, Dhanvantari, Administration, Academic section and other departments, for their generous help whenever needed.

I acknowledge JNCASR, University Grand Commission (UGC) and Marie Curie Actions Plan of European Union for financial supports.

I would like to thank all the past and present lab members - Dr. Suman Majumder, Dr. Sutapa Roy, Dr. Shaista Ahmed, Saugata Patra, Saikat Charaborty, Subhajit Paul, Nalina V., Koyel Das and Arabinda Bera - for all the scientific and nonscientific discussions. They always kept the environment inside the lab intellectually vibrant. In addition, I have gained from academic discussions with Sunita K., Sudeshna Sen, Prianka Singh, Koushik Pal, Dibyajyoti Ghosh, Anshul Singh Parmar, Bradraj Pandey, Anirban Mondal, Wasim Raja Mondal and Gaurav Shrivastav. I am also thankful to

all my other friends from JNCASR, particularly to Somnath Ghara, Arpan De, Chandan De, Sisir Maity and Abhijit Sen, for making my stay enjoyable here. I thank my long time friend Kartik Sau for being helpful at various occasions.

Finally, it is time to express my deepest gratitude towards my parents and all the other family members for their unflagging love, unconditional support and encouragement. Special thanks to my wife Jahanara for being with me in all slopes of life. Her unfailing love, constant mental support and encouragement made this dissertation possible.

I thank all others who helped me directly or indirectly.

Synopsis

Objective of this thesis has been to understand a few equilibrium and nonequilibrium properties of materials, in connection with phase transitions of different types, viz., paramagnetic to ferromagnetic transition, solid-solid transition, vapor-solid transition and vapor-liquid transition. The **first chapter** provides theoretical background on various structural and dynamical aspects of first and second order phase transitions; describes important models and necessary tools for computational studies of problems associated with dynamic critical phenomena, kinetics of phase transitions and aging properties; introduces a few methods to analyze related simulation data. Below we provide a brief overview of the problems that will be discussed in the subsequent chapters.

In **Chapter 2** we have studied the phase behavior and the dynamic critical phenomena for a single component three-dimensional Lennard-Jones (LJ) fluid that exhibits vapor-liquid transition. The phase diagram is obtained via Gibbs ensemble Monte Carlo (GEMC) simulation method. For the dynamics, we have computed the bulk viscosity and thermal conductivity using Green-Kubo relations, by taking inputs from molecular dynamics simulations in microcanonical ensemble. The critical singularities of these transport properties were quantified via the application of finite-size scaling theory and compared with the existing theoretical predictions.

Chapter 3 contains the results for the kinetics of vapor-liquid phase transitions in a single component two-dimensional LJ fluid. Again, the phase diagram has been obtained via the GEMC simulation method. We quench

very low density homogeneous systems inside the miscibility gap. Following such quenches, disconnected circular liquid clusters appear in the system. We identified that these clusters exhibit diffusive motion in the background vapor phase and grow via sticky collisions among them. The growth has been quantified as a function of time and is found to be in nice agreement with a theoretical prediction. In this chapter we also present some results for the quenches with critical density.

In **Chapter 4** we have studied the kinetics of vapor-solid phase transition for the same model and dimension as in Chapter 3. Systems with overall density close to the vapor branch of the coexistence curve have been quenched to very low temperatures. Following such quenches, we observe appearance of disconnected liquid clusters (of circular shape) at early time. Growth of these clusters occur due to the deposition of particles on them from the background vapor phase. Gradually, crystallization occurs inside the clusters and at the same time the density of the vapor phase saturates to a very low value. These solid clusters move ballistically through the low density vapor phase and grow via inter-cluster sticky collisions. The slow relaxation inside these solid clusters cannot compete with the fast growth via such ballistic aggregation mechanism. This gives rise to fractality in the structure which as well plays important role in further enhancement of the growth rate. We provide quantitative understanding of the structure-dynamics relation, as a function of temperature.

In **Chapter 5** we have studied aging property during ordering in ferromagnets, using the time dependent Ginzburg-Landau equations, in space dimensions $d = 2$ and 3. Our focus has been on the behavior of the two

time order-parameter autocorrelation function, $C(t, t_w)$. We have observed scaling of $C(t, t_w)$ with respect to ℓ/ℓ_w, where ℓ and ℓ_w are the characteristic length scales at times t (observation time) and t_w (waiting time), respectively. We have obtained a full form of the scaling function from appropriate analyses of the simulation data. The scaling function has the late time form $(\ell/\ell_w)^{-\lambda^{ag}}$. In both the dimensions, we have accurately estimated the values of the exponent λ^{ag}, via first application of the finite-size-scaling theory. These results are compared with those from the Ising model with nonconserved order-parameter dynamics.

Finally, in the **last (6th) Chapter** we have presented the results for aging dynamics during demixing transitions in solid binary mixtures, obtained via the numerical solutions of the Cahn-Hilliard equations, in space dimensions $d = 2$ and 3. Here also, as in the previous chapter, we have observed scaling of $C(t, t_w)$ with respect to ℓ/ℓ_w. An empirical full form is obtained which again exhibits power-law decay at late time. The exponents in different dimensions have been calculated via the finite-size scaling analyses. In both the chapters, 5 and 6, it has been shown that the estimated values of the exponents satisfy the theoretically predicted (dimension dependent) bounds.

List of Publications

- "Aging in ferromagnetic ordering: Full decay and finite-size scaling of autocorrelation." **Jiarul Midya**, Suman Majumder and Subir K. Das, J. Phys.: Condens. Matter **26**, 452202 (2014).

- "Dimensionality dependence of aging in kinetics of diffusive phase separation: Behavior of order-parameter autocorrelation" **Jiarul Midya**, Suman Majumder and Subir K. Das, Phys. Rev. E **92**, 022124 (2015).

- "Coarsening in fluid phase transitions", Subir K. Das, Sutapa Roy and **Jiarul Midya**, C. R. Physique **16**, 303315 (2015).

- "Droplet growth during vapor-liquid transition in a 2D Lennard-Jones fluid", **Jiarul Midya** and Subir K. Das, J. Chem. Phys. **146**, 024503 (2017).

- "Finite-size scaling study of dynamic critical phenomena in a vapor-liquid transition", **Jiarul Midya** and Subir K. Das, J. Chem. Phys. **146**, 044503 (2017).

- "Kinetics of vapor-solid phase transitions: Structure, growth and mechanism", **Jiarul Midya** and Subir K. Das, submitted.

List of Figures

Contents

Chapter 1

Introduction

1.1 Phase transitions

Phase transitions are very commonly observed in nature and related topics are of much research interest [1–26]. The change of phase in a system takes place due to variation in different thermodynamic variables, like pressure (P), temperature (T), magnetic field (h), etc. In addition to being fundamental to the understanding of matter, knowledge of it is important in technological developments. In Fig. 1.1 we show a schematic phase diagram [1] of a normal chemical substance in the $P-T$ plane. The three distinct phases, viz., solid, liquid and gas, in this figure, are separated by different coexistence curves, along each of which two phases coexist with each other in equilibrium. For example, along the red curve, referred to as the fusion curve [1], solid and liquid phases coexist. The gas-solid (pink curve) and gas-liquid (green curve) coexistence curves are referred to as the sublimation and the vaporization curves, respectively [1]. All these curves meet at a point, referred to as

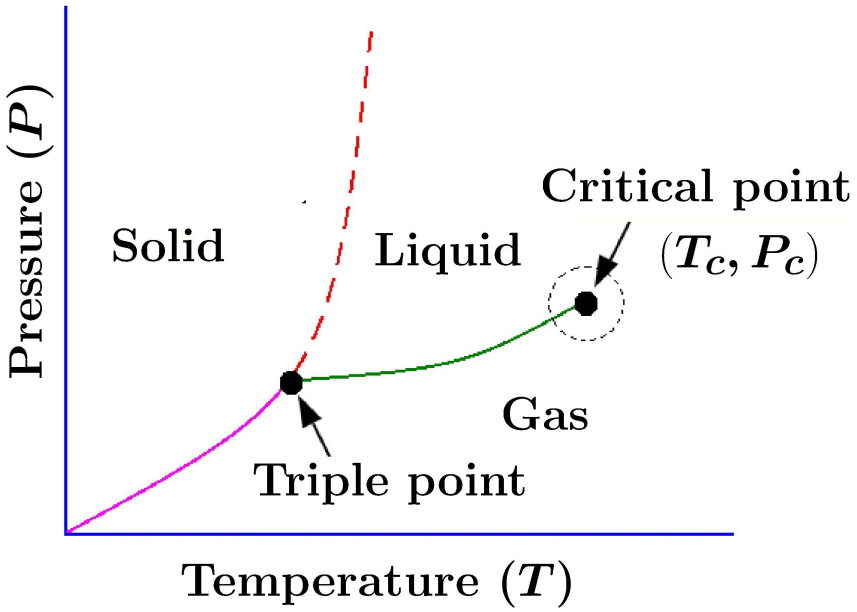

Figure 1.1: A schematic phase diagram of a normal chemical substance in the $P - T$ plane. Various phases are separated from each other by the coexistence curves. The point (T_c, P_c) represents the critical point for the gas-liquid transition.

the *triple point* [1], implying coexistence of all the three phases. Unlike the fusion curve, which does not terminate, the vaporization curve terminates at a *critical point* (T_c, P_c), T_c and P_c being respectively the critical temperature and pressure [1]. At this point the value of the order-parameter [2–8] ψ, the density difference between liquid (ρ_ℓ) and gas (ρ_g) phases, vanishes. On the other hand, ψ is nonzero in the coexistence region, implying a jump in density (ρ) as one moves from one phase to another. Such a transition is referred to as the *first order phase transition* [1–8], since the jump is related to the first derivative of an appropriate free energy. In the case of a transition at the critical point, the first derivative is continuous; however, various second derivatives exhibit nontrivial singularities or divergences. This is referred to

as the *continuous or second order phase transition* [1–8].

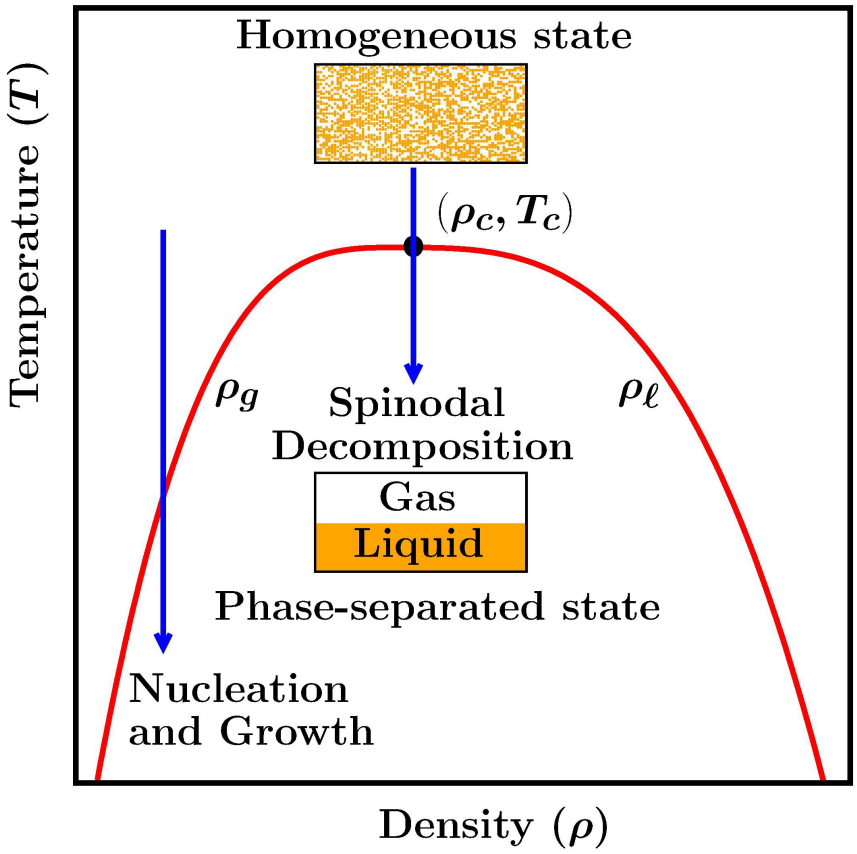

Figure 1.2: Phase diagram of a normal chemical system in the temperature vs density plane. The regions outside and inside the coexistence curve provide homogeneous and phase-separated states, respectively.

In Fig. 1.2 we have shown the phase diagram related to vapor-liquid coexistence in $T-\rho$ plane [1]. Here, (ρ_c, T_c) is the critical point, ρ_c being the critical density of the system. Above T_c the system is in a homogeneous state, i.e., a state where the gas and liquid phases are not separately identifiable. As stated, inside the curve we observe phase coexistence of gas and liquid, as depicted in the figure. There the right and left branches of the coexistence curve correspond to the high density liquid and the low density gas phases,

respectively. In the case of a binary $(A + B)$ mixture (binary alloy or fluid) also the coexistence curve [6, 13] is very similar. However, the density in the abscissa has to be replaced by the concentration of any one of the species, say x_A $(= \frac{N_A}{N}$, N_A being the number of A particles and N the total number of particles). In that case, the right branch will correspond to the concentration of the A-type of particles in the A-rich phase and the left branch will be the concentration of A-type of particles in the B-rich phase.

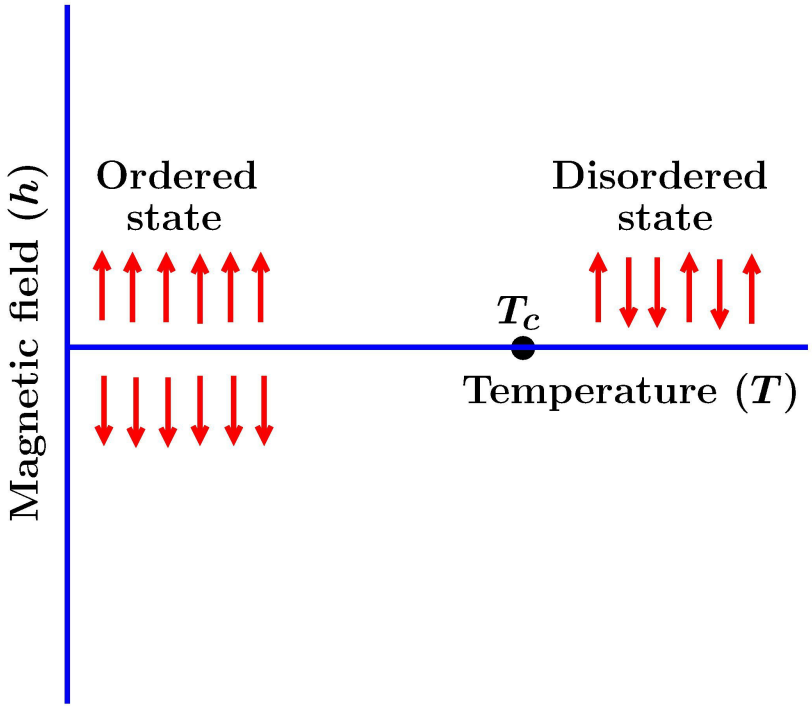

Figure 1.3: Schematic phase diagram for a para- to ferromagnetic transition in the $h - T$ plane. In the figure the large black dot is the location of Curie temperature, T_c. Below the Curie temperature the system acquires a spontaneous magnetization.

For a magnetic system, exhibiting para- to ferromagnetic transition [4,6], the phase diagram is shown Fig. 1.3, in the $h - T$ plane. (The T vs ψ

diagram again has a look similar to the one in Fig. 1.2). In this case, the critical temperature T_c is often referred as the *Curie temperature*. Above T_c the system is in a disordered paramagnetic state with net magnetization (ψ) zero, if $h = 0$. On the other hand, for $T < T_c$ one observes a ferromagnetic state, even for $h = 0$, where most of the spins are aligned in a particular direction. This means that the system acquires a spontaneous magnetization $\psi \neq 0$.

In the vicinity of a critical point various interesting phenomena happen which are referred to as the "critical phenomena" [1, 3, 7, 8, 12–16]. Some details of these are given below.

1.2 Critical phenomena

The central quantity in critical phenomena is the correlation length (ξ) that provides an understanding of the crucial fact of order-parameter fluctuation [1]. In the thermodynamic limit of the system size, ξ diverges at the critical point. In addition, number of other static and dynamic quantities also show singular behavior [1, 3, 12, 13, 15, 16, 27–38]. These singularities are mathematically expressed as power-laws in terms of the reduced temperature ϵ ($= |T - T_c|/T_c$). In Table 1.1, we have listed some of the static quantities, along with the values of the corresponding exponents as classified according to different universalities (to be discussed below) [1, 12], which show such anomalous behavior at T_c. All of these critical exponents are not independent of each other, they follow certain scaling relations [1, 7, 8]. E.g., some

relations connecting the static exponents are [1, 7, 8]

Rushbrooke relation: $\alpha + 2\beta + \gamma = 2$; Fisher relation: $\gamma = \nu(2 - \eta)$

Josephson relation: $\nu d = 2 - \alpha$; Widom relation: $\gamma = \beta(\delta - 1)$.

Table 1.1		
Static quantities	$3-d$ Ising universality class	Classical universality class
Order-parameter: $\psi \sim \epsilon^{\beta}$	$\beta = 0.325$	$\beta = \frac{1}{2}$
Susceptibility: $\chi \sim \epsilon^{-\gamma}$	$\gamma = 1.239$	$\gamma = 1$
Specific heat: $C \sim \epsilon^{-\alpha}$	$\alpha = 0.11$	$\alpha = 0$
Correlation length: $\xi \sim \epsilon^{-\nu}$	$\nu = 0.63$	$\nu = \frac{1}{2}$

Table 1.1: Power-law singularities of the static quantities at the critical point, along with the exponent values in different universality classes.

The exponents are universal in the sense that their values do not depend much on the microscopic details of the system, understanding of which advanced significantly due to the Renormalization Group (RG) theory [7, 8]. Depending upon the type of interaction, short- or long-range, there exits two universality classes for static quantities, viz., Ising universality class and the classical universality class [7, 8], for a scalar order parameter. The values of the static exponents for $3 - d$ Ising universality class as well as for classical universality class have been quoted in Table 1.1. The universality picture holds irrespective of the choice of materials and type of transition, e.g., all of vapor-liquid, liquid-liquid, para-to-ferromagnetic transitions will have the

same set of exponent values.

Table 1.2
Dynamics exponents for $3-d$ fluid universality class
Relaxation time: $\tau \sim \xi^z$; $z = 3.068$
Diffusivity: $D \sim \xi^{-x_D}$; $x_D = 1.068$
Shear viscosity: $\eta \sim \xi^{x_\eta}$; $x_\eta = 0.068$
Bulk viscosity: $\zeta \sim \xi^{x_\zeta}$; $x_\zeta = 2.893$

Table 1.2: Singularities and exponents for dynamic quantities for $3-d$ fluid-fluid transitions.

The dynamic universality is not as robust as static [12, 39]. For example, the value of the exponent z, providing information on the relaxation time ($\tau \sim \xi^z$), can vary from ensemble to ensemble [12, 39]. The dynamic exponents also follow scaling relations [1, 3] such as

$$x_D = 1 + x_\eta; \qquad z = 3 + x_\eta; \qquad x_\zeta = z - \frac{\alpha}{\nu}. \tag{1.1}$$

According to the theories based on a field theoretic model, referred to as the model H [4, 6, 12], the values of the dynamic critical exponents will be same for all materials if the transitions are of fluid-fluid type. These values are quoted in Table 1.2.

1.3 Phase ordering dynamics

When a system, prepared at temperature $T > T_c$, is quenched inside the coexistence curve, it becomes unstable to fluctuations. Such an out-of-equilibrium system, during a first order transition, evolves towards a new (ordered) equilibrium state via the formation and growth of domains of like particles or spins. Dynamics of such evolution is referred to as the "phase ordering dynamics" or "coarsening dynamics" [3–6]. This can be illustrated via the Landau free energy function [4, 7, 8]

$$F[\psi, T] = a_0(T - T_c)\psi^2 + b_0\psi^4, \tag{1.2}$$

plots of which for various temperatures are shown in Fig. 1.4. Here, a_0 and b_0 are positive constants. From Eq. (1.2) it is clear that the minimization of F with respect to ψ provides two lowest energy states, as marked by "P" and "Q" (see Fig. 1.4), for $T < T_c$. These correspond to nonzero values of ψ and imply ordering. For $T > T_c$, on the other hand, there exists one minimum at the equilibrium order-parameter value $\psi = 0$, corresponding to a homogeneous configuration. The latter becomes a maximum for $T < T_c$. Thus, when a homogeneous system is quenched below T_c, it moves towards the ordered states with $\psi \neq 0$. The length scale of the ordered phases, following a quench, increases [4] with the progress of time, as different broken-symmetry phases compete with each other to select the final equilibrium state. During this evolution process, ψ is thus a function of space ($\vec{r}$) and time (t).

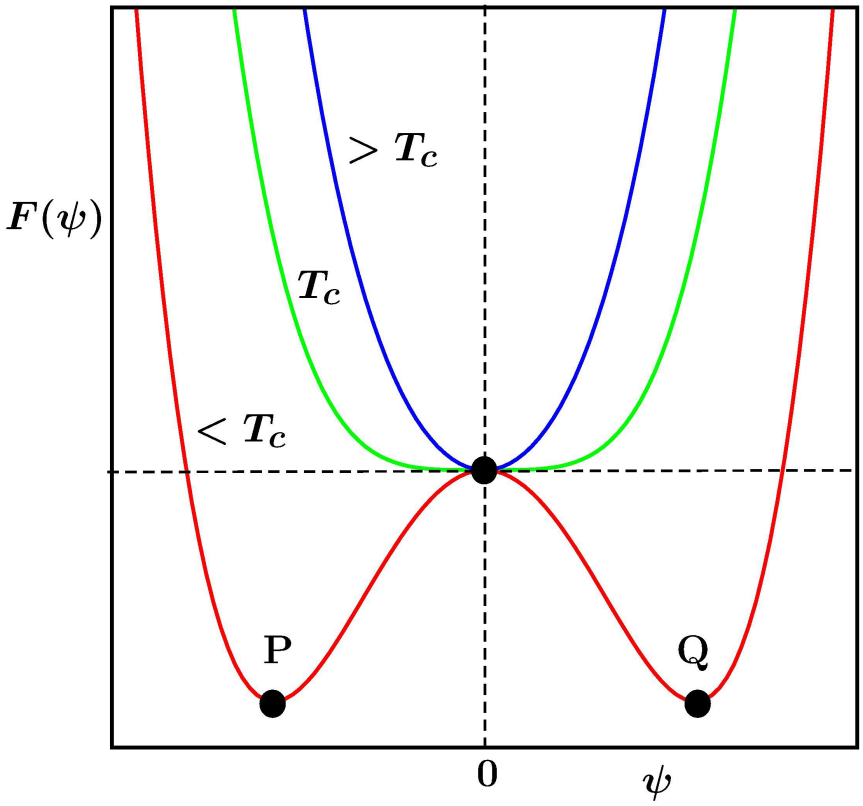

Figure 1.4: Plots of the Landau free energy, $F(\psi)$, vs ψ, for three different temperatures, viz., $T > T_c$, $T = T_c$ and $T < T_c$.

Depending upon the type of transition, the total value of the order-parameter may or may not remain conserved with time [4]. While the ordering in a ferromagnet is an example of nonconserved order-parameter dynamics, kinetics of phase separation in a binary mixture belongs to the category of conserved order-parameter dynamics. For conserved case, depending upon the regions inside coexistence curve, the coarsening can occur via "spinodal decomposition" or "nucleation and growth" [3–6, 40], which we discuss below.

1.3.1 Spinodal decomposition

Spinodal decomposition [3–6] is observed if a system is quenched with an overall density or composition close to the critical value, as shown in Fig. 1.2 with one of the down-arrows. In this case, the system falls out-of-equilibrium almost instantaneously. So, the phase ordering or coarsening starts immediately after the quench.

Let us consider the phase separation in a solid binary $(A + B)$ mixture. Starting from a homogeneous state, say, with critical composition (mixture of 50% A-type and 50% B-type of particles), the system is quenched inside the coexistence curve. The system will then evolve towards the new equilibrium state via the formation and growth of domains of A-rich and B-rich phases. In Fig. 1.5 we show some snapshots during such a evolution, obtained from the numerical solutions of the Cahn-Hilliard equation (will be discussed later) [6]. It is clear from these snapshots that the growing domains are percolating in nature.

Typically, coarsening phenomena are multiplicatively self-similar in nature [4, 6], which may as well be appreciated from these snapshots. This property provides a power-law growth of the average domain size ℓ [4, 6] as

$$\ell(t) \sim t^{\alpha}. \tag{1.3}$$

The value of α depends upon the number of components of the order parameter, the range of interaction, the conservation of order-parameter, space dimension, hydrodynamics, proximity to the coexistence curve, etc. [4, 6, 40]. Shortly we will discuss some of the growth laws, which are relevant for this

thesis.

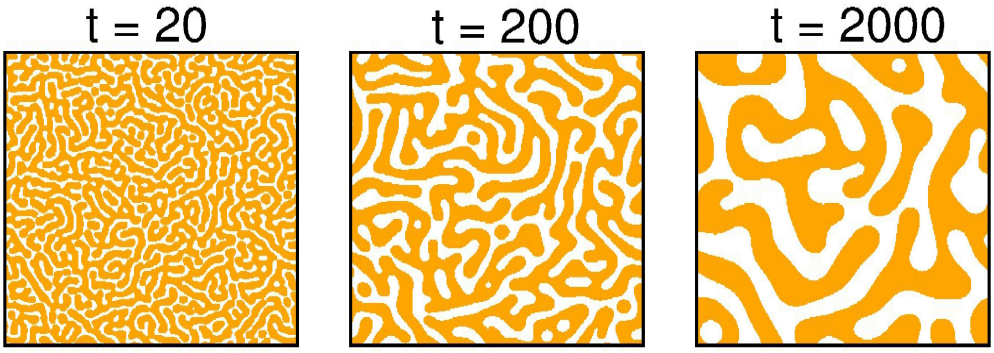

Figure 1.5: Snapshots during the evolution of a phase separating solid binary $(A + B)$ mixture, in space dimension $d = 2$. These are obtained for critical composition (50% A and 50% B particles) quench of the system inside the miscibility gap, from a high temperature homogeneous state. The orange and the white colors in the snapshots correspond to the A-rich and the B-rich phases, respectively. The results were obtained via numerical solutions of the Cahn-Hilliard equation.

1.3.2 Nucleation and growth

The regions very close to the coexistence curve offer metastability to a quenched system. There the phase-separation occurs via *nucleation and growth* [5, 6, 40, 41]. In this case, to make the system unstable, long wavelength fluctuations are needed. These fluctuations try to accumulate particles (spread over wide regions) to form stable nuclei which can grow with time. Since such fluctuations are rare, nucleation may get delayed.

There exists two broad types of nucleation, *heterogeneous nucleation* (occurs in the presence of external agent) and *homogeneous nucleation* (occurs in absence of external agents) [5]. Here we are interested in the latter one,

i.e., nucleation in pure substances.

The formation of a nucleus introduces a boundary between the two phases. For example, in case of gas-liquid transitions, when a system is quenched close to the vapor branch of the coexistence curve from a homogeneous state, a liquid droplet with radius R is formed, which is separated from the background gas phase by an interface, as shown in Fig. 1.6(a). The presence of interfaces introduces a barrier, ΔF, in free energy, which can be understood from the construction [5, 6]

$$\Delta F(R) = -\frac{4}{3}\pi R^3 F_v + 4\pi R^2 \gamma. \tag{1.4}$$

In Eq. (1.4), the first part is the volume term, while the second one is due to the presence of the interface. Here, F_v and γ are the volume free energy density and surface tension, respectively. The plot of $\Delta F(R)$ is shown in Fig. 1.6(b). The stability of a nucleus is decided by the competition between the volume and surface terms, as depicted in Fig. 1.6(b). If the droplet radius is larger than a critical value R_c, obtainable from the optimization in Eq. (1.4), it becomes a stable droplet which can grow with time.

In Fig. 1.7 we have presented a few snapshots from an evolving solid binary $(A + B)$ mixture which has been quenched with an off-critical composition (20% A particles and 80% B particles), again obtained using the Cahn-Hilliard model [6]. Thus, the phase separation occurs via nucleation and growth. In this case, as seen in this figure, the morphology consists of disconnected droplets. Like in spinodal decomposition, growth of such droplets also exhibit statistical self-similarity and power-laws [19].

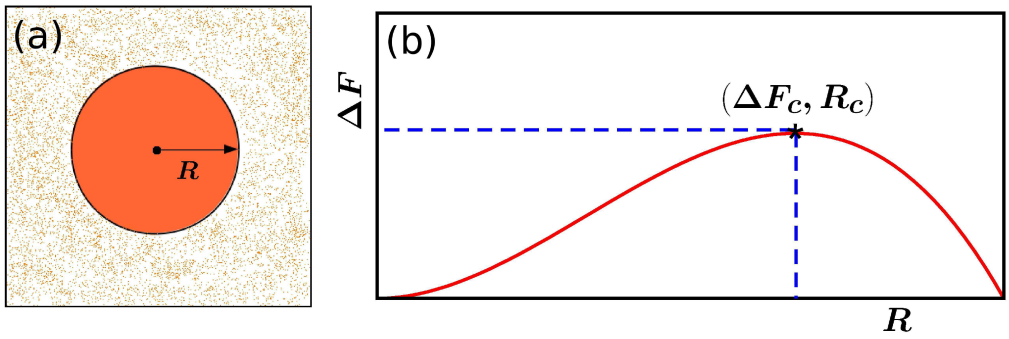

Figure 1.6: (a) Schematic picture of a liquid droplet (of radius R) in the background of a gas phase. (b) Plot of free energy, ΔF, vs radius of a droplet. The maximum of the free energy occurs at $R = R_c$, referred to as the critical size for a stable nucleus.

1.4 Typical models and growth laws related to coarsening dynamics

We will first consider the case of nonconserved order-parameter dynamics. We confine ourselves to scalar order parameter only.

1.4.1 Nonconserved order-parameter dynamics

In the nonconserved order-parameter case [4, 6, 18] the value of the global order-parameter (integration of the order-parameter over the whole space, $\int \psi(\vec{r}, t) dr^3$) is not constant during evolution. As stated earlier, an example of this is ordering in a ferromagnet, having been quenched from a disordered paramagnetic state. For $T > T_c$, as already stated, the average magnetization, ψ (order-parameter of the system), is zero. Finally, as it reaches the ferromagnetic equilibrium state, most of the spins are aligned in the same direction, giving rise to a nonzero value of ψ. Thus, the total value of the

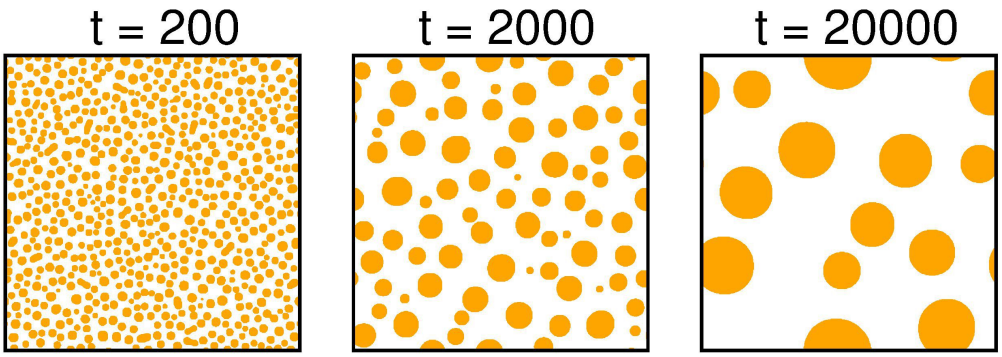

Figure 1.7: Evolution snapshots for an phase-separating off-critical binary $(A + B)$ alloy, in space dimension $d = 2$. The results are obtained from the numerical solutions of the Cahn-Hilliard equation with 20:80 ratio of numbers of A and B particles.

order-parameter is not respected.

To understand such ferromagnetic ordering, in the atomistic level one typically considers the Glauber spin flip Monte Carlo simulations [39, 42] of the Ising model that has the Hamiltonian [39]

$$H = -J \sum_{<ij>} S_i S_j; \;\; S_i = \pm 1; \;\; J > 0. \tag{1.5}$$

Here, $S_i = +1(-1)$ corresponds to an up (down) spin on a regular lattice, at a site i, $< ij >$ stands for a sum over the nearest neighbors. A positive value of the interaction strength J implies ferromagnetic state. In Glauber spin flip Monte Carlo [42], one chooses a spin randomly, flips it and calculates the energy difference, ΔE, between the original and tried states. The trial is accepted according to the standard Metropolis algorithm [39]. Details will be discussed later.

The ordering in a ferromagnet has also been well captured, at the macroscopic level, by the coarse-grained version of the Glauber Ising model, referred to as the time dependent Ginzburg-Landau (TDGL) [4, 6] equation. The TDGL equation is written as

$$\frac{\partial\psi(\vec{r},t)}{\partial t} = p_0\psi(\vec{r},t) - q_0\psi^3(\vec{r},t) + r_0\nabla^2\psi(\vec{r},t), \tag{1.6}$$

where, p_0, q_0 and r_0 are temperature dependent positive coefficients given respectively by $p_0 = \Gamma(T_c - T)$, $q_0 = \Gamma\frac{T}{3}\left(\frac{T_c}{T}\right)^3$ and $r_0 = \Gamma\frac{a^2T_c}{q}$, Γ being a damping coefficient. The TDGL equation can be phenomenologically obtained by considering the relaxation of a ferromagnetic system in an overdamped situation as [4]

$$\frac{\partial\psi(\vec{r},t)}{\partial t} \propto -\frac{\delta F[\psi(\vec{r},t)]}{\delta\psi(\vec{r},t)}, \tag{1.7}$$

where F is the standard Ginzburg-Landau (GL) free energy functional [4,6], given by

$$\frac{F}{k_BT} = \int d\vec{r}\,\Big[-\frac{1}{2}\left(\frac{T_c}{T}-1\right)\psi^2 + \frac{1}{12}\left(\frac{T_c}{T}\right)^3\psi^4 + \frac{T_c}{2qT}a^2(\vec{\nabla}\psi)^2\Big]. \tag{1.8}$$

For non-conserved order-parameter dynamics, the coarsening of domains occurs due to curvature driven motion of domain walls. For this, one writes

$$\frac{d\ell}{dt} \sim \frac{1}{\ell}. \tag{1.9}$$

This provides

$$\ell(t) \sim t^{1/2}, \tag{1.10}$$

which is known as the Chan-Allen growth law [4,6,43]. The derivation ignores system dimensionality.

1.4.2 Conserved order-parameter dynamics

In conserved order-parameter dynamics [4,6,44], the global order-parameter value remains constant during the entire process of evolution. An example is phase separation in a solid binary $(A + B)$ mixture. When a binary mixture is quenched from a high temperature $(T > T_c)$ homogeneous phase to a low temperature phase-separated state, it goes to a new equilibrium via the formation and growth of A-rich and B-rich domains. Here, the continuity equation [4, 6]

$$\frac{\partial \psi(\vec{r}, t)}{\partial t} = -\vec{\nabla} \cdot \vec{\mathcal{J}}, \tag{1.11}$$

is valid. In Eq. (1.11), $\vec{\mathcal{J}}$ is the concentration current, which is related to the chemical potential μ_c as

$$\vec{\mathcal{J}} = -D\vec{\nabla}\mu_c(\vec{r}, t), \tag{1.12}$$

where D is a diffusion constant. The chemical potential can be obtained from the functional derivative of free energy F (defined above), with respect to ψ, as

$$\mu_c = \frac{\delta F[\psi(\vec{r}, t)]}{\delta \psi(\vec{r}, t)}. \tag{1.13}$$

Combining the Eqs. (1.11), (1.12) and (1.13), one arrives at [4, 6]

$$\frac{\partial\psi(\vec{r},t)}{\partial t} = -\nabla^2\big[p_0\psi(\vec{r},t) - q_0\psi^3(\vec{r},t) + r_0\nabla^2\psi(\vec{r},t)\big], \tag{1.14}$$

which is referred to as the Cahn-Hilliard (CH) equation [4, 6, 44, 45], where p_0, q_0 and r_0 are temperature dependent positive coefficients. In Eq. (1.14), like the TDGL equation, the value of $\psi(\vec{r},t)$ can take values between $+\infty$ to $-\infty$. The positive values of ψ imply A-rich regions, while the negative values stand for B-rich regions. We solve Eq. (1.14) using the Euler discretization technique [6], to be described later.

The demixing transition in solid binary mixtures can also be studied via the Kawasaki spin exchange Monte Carlo simulations [39] of the Ising model, the Hamiltonian of which is given above. In this case, $S_i = +1$ and -1 correspond to A- and B-type of particles, respectively. In Kawasaki exchange Monte Carlo simulation, one picks up a pair of nearest neighbor particles randomly and interchanges their positions. This trial exchange is accepted or rejected via the Metropolis algorithm [39].

For conserved dynamics in solid binary mixtures the coarsening of domains occurs due to the diffusion of particles. The gradient in the chemical potential provides the drive for such transport. The interface velocity can thus be written as [23]

$$\frac{d\ell(t)}{dt} \sim |\vec{\nabla\mu_c}| \propto \frac{\gamma}{\ell^2(t)}, \tag{1.15}$$

where γ is the interfacial tension. The solution of Eq. (1.15) gives

$$\ell(t) \sim t^{1/3}, \tag{1.16}$$

referred to as the Lifshitz-Slyosov (LS) growth law [6,23,46]. This law is valid in different dimensions. Kinetics of phase separation in fluids, on the other hand, is a more complex phenomena, with strong influence from dimension and other facts. This we discuss separately in the next subsection.

1.4.3 Fluid systems

In fluids, due to hydrodynamics, the growth is typically much faster than the cases which have been discussed above. Here the growth exponent depends upon morphology as well as dimensionality [19, 40, 47–51]. To study the kinetics of separation in fluid phase transitions, typically one considers model H [12], lattice Boltzmann simulation [6], molecular dynamics simulation [52, 53], etc.

At the very early stage of phase separation in a fluid system the domain coarsening occurs via the particle diffusion mechanism (due to chemical potential or concentration gradient), providing $\alpha = 1/3$ as in solid binary mixtures [46]. At a later time, when the domains are large, hydrodynamic effects become important. First we focus on the percolating morphology. In this case, fast advective transport of materials occurs through the interconnected channels due to pressure gradient, obtainable from the interfacial tension [49]. This hydrodynamic regime is divided into two sub-regimes, viz., *viscous* and *inertial hydrodynamic* regimes [4, 6]. Before getting into further discussion

on that we introduce the model H below.

Model H is essentially a combination of the CH equation and Naiver-Stokes (NS) equation [3,6,12]. There one writes the dynamical equations for the order-parameter and velocity field as

$$\frac{\partial\psi}{\partial t} + \vec{v}\cdot\vec{\nabla}\psi = D\nabla^2\mu, \tag{1.17}$$

$$\rho\frac{D}{Dt}\vec{v} - \eta\rho\nabla^2\vec{v} = -\vec{\nabla}p - \psi\vec{\nabla}\mu. \tag{1.18}$$

In Eqs. (1.17) and (1.18), D is the diffusion constant, p is the pressure and the operator $\frac{D}{Dt}$ should be expanded as $\frac{d}{dt} + (\vec{v}\cdot\vec{\nabla})$. Starting from the Navier-Stokes equation for incompressible fluid, via dimensional analysis, Farukawa [47,48] arrived at (f is a friction coefficient)

$$\frac{d\ell}{dt} + f\ell\Big(\frac{d\ell}{dt}\Big)^2 = \frac{t_0\gamma}{\eta\xi\rho}, \tag{1.19}$$

t_0 being the relaxation time, related to the equilibrium distance ξ, given as

$$t_0 = \frac{\xi^2}{D}. \tag{1.20}$$

Using the expressions for t_0, η (via the generalized Stokes-Einstein-Sutherland relation [3,54]) and the critical singularity [3] of γ ($\sim \xi^{-2}$), it can be shown that the right hand side of Eq. (1.19) is a constant. Note here that on the other side of Eq. (1.19) the first term stands for dissipative friction and the second one corresponds to internal friction. At intermediate time scale, the dissipative (viscous) term dominates, whereas the inertial term becomes

more important at very late time. Under such considerations, following the LS value [46], there will be a crossover to $\alpha = 1$ which will give way to $\alpha = 2/3$ at very late time. According to San Miguel et al. [55], however, the stripes (analog of tubes) in $d = 2$ will be stable under weak perturbations. In this case, they propose an interface diffusion mechanism that provides $\alpha = 1/2$. There is, on the other hand, reasonable consensus on the very late time 2/3 value of α, even in this dimension.

For off-critical quench one observes disconnected, droplet-like domain morphology [19, 40] which invalidate the above descriptions of growth. This is because, there cannot be continuous flow of matter due to advection, a key hydrodynamic transport feature for tube-like interconnected domain morphology. In the disconnected case, phase separation occurs via droplet collision and coalescence mechanism [40, 49], i.e., two droplets collide and merge with each other to form a single larger droplet. This is also known as Binder-Stauffer (BS) mechanism [40]. Even though contribution from particle diffusion will be there, the latter will provide a much slower growth. For the BS mechanism, the droplet density (n) decays with time. For the time dependence of n, one writes

$$\frac{dn}{dt} = -D\ell n^2, \tag{1.21}$$

D being a length scale dependent diffusion constant. Since the droplets move diffusively, the Stoke-Einstein-Sutherland relation provides a constant value

for $D\ell$. Incorporating this fact and using $n \sim 1/\ell^d$ in Eq. (1.21) one obtains

$$\frac{d\ell}{dt} \sim \frac{1}{\ell^{d-1}}. \tag{1.22}$$

Solving Eq. (1.22) one gets $\ell(t) \sim t^{1/d}$. Thus, $\alpha = 1/3$ in $d = 3$, same as the LS value, though the mechanisms are completely different. Difference between the two cases will be seen in the growth amplitudes [41], BS providing a higher value. In table 1.3 we summarize all the growth laws for kinetics of fluid phase separation.

Another important aspect of coarsening phenomena is aging [6, 22, 24, 56, 57]. This we will discuss briefly later.

Table 1.3

Critical quench		
Growth Mechanism	d=3	d=2
Diffusive growth	$\alpha = \frac{1}{3}$	$\alpha = \frac{1}{3}$
Viscus Hydrodynamic growth ($d = 3$), Interface diffusion ($d = 2$)	1	$\frac{1}{2}$
Inertial Hydrodynamic growth	$\frac{2}{3}$	$\frac{2}{3}$
Off-critical quench		
Growth Mechanism	d=3	d=2
Particle diffusion mechanism	$\alpha = \frac{1}{3}$	$\alpha = \frac{1}{3}$
Droplet diffusion and collision mechanism	$\frac{1}{3}$	$\frac{1}{2}$

Table 1.3: Domain growth-laws in fluids, for critical and off-critical quenches, in various space dimensions.

1.5 Finite-size effects in computer simulations

In computer simulations, one faces serious problems with respect to the finite-size effects. For systems with growing length scales, these effects cannot be taken care of even via the application of periodic boundary conditions. As discussed, for a thermodynamically large system the correlation length diverges at the critical point [1]. Whereas, for a finite system the divergence of ξ will be restricted by the system size [13,39] L, i.e., $\xi = L$ at $T = T_c$. Fig. 1.8 schematically shows [1] how ξ increases as one approaches T_c. Because of the above mentioned finite-size restriction on ξ, close to the critical point the behavior of various static and dynamic quantities will be affected.

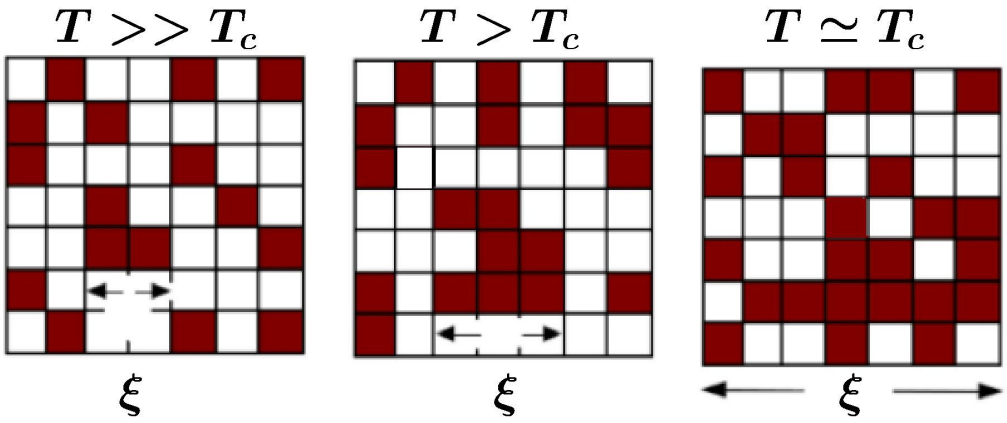

Figure 1.8: Schematic snapshots showing the increase of the static correlation length, ξ, as one approaches T_c. The brown blocks are regions over which correlation has developed. For a finite system, at $T = T_c$ the correlation length attains the system size L.

The finite-size effects are also problematic in the domain growth problems

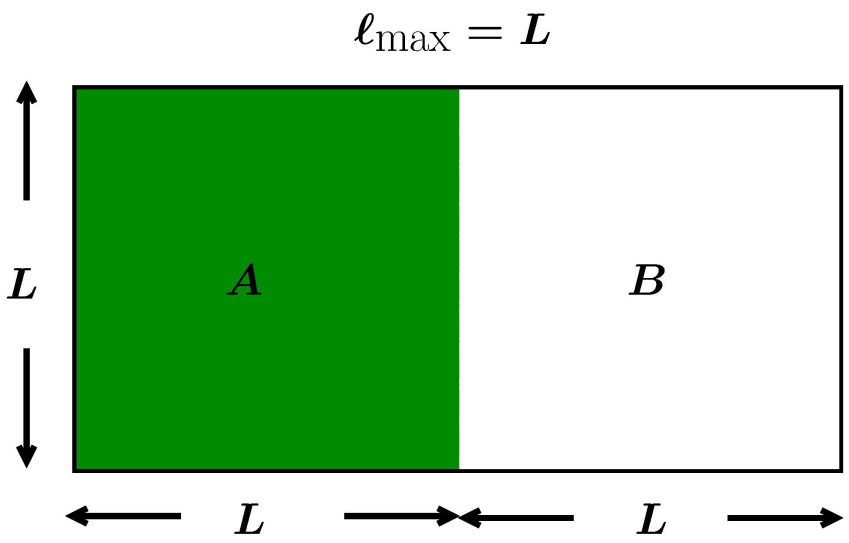

Figure 1.9: Schematic representation of the phase coexistence of a symmetric (50:50) binary ($A + B$) mixture in equilibrium. The domain length, ℓ, for both the phases, can attain the maximum value equal to L.

[17]. For example, let us consider the phase separation of a binary mixture with 50% A particles and 50% B particles. In equilibrium, the domain length of a particular phase (A- or B-phase) can attain the maximum value L (see the Fig. 1.9). Thus, for a finite system the behavior of $\ell(t)$ deviates from the expected power-law divergence as $\ell \to L$. As a result, often it does not become possible to come up with correct conclusions about the growth exponents.

In absence of adequate computational resources, the way to overcome such problems is the application of the finite-size scaling theory [13]. This sophisticated method was first introduced by M.E. Fisher, in the context of equilibrium critical phenomena. This we discuss in the next section.

1.6 Finite-size scaling analysis

This technique [13] has extensively been used in the equilibrium critical phenomena [39] as well as in the nonequilibrium domain coarsening problems [17, 51, 58]. Here we briefly discuss how this technique can be used in the context of equilibrium critical phenomena. Let us consider a quantity Z which shows singularity at the critical point as

$$Z = Z_0 \epsilon^z, \tag{1.23}$$

where z is the critical exponent and Z_0 is critical amplitude of Z. For a finite system, the critical enhancement of Z will be restricted by system size L. To account for that one should introduce a scaling function, $Y(y)$, such that

$$Z = Z_0 Y(y) \epsilon^z. \tag{1.24}$$

The scaling function $Y(y)$ should be independent of the system size. This is possible if the scaling parameter y is a dimensionless quantity. The appropriate choice $y = L/\xi$, the ratio of two length scales, provides information on the deficiency of the system size. A plot of Y vs y, using data from different system sizes, will show a master curve for the correct choice of z.

In the domain growth problem the same technique can be used to estimate the growth exponent. There ℓ and $1/t$ should be treated as quantities analogous to ξ and ϵ, respectively.

1.7 Quantities of interest

In phase transitions, depending upon interests, one focuses on various quantities. In this section, we will briefly discuss a few quantities, relevant primarily in our studies of kinetics. For dynamic critical phenomena, we will provide details in the next chapter.

1.7.1 Two-point equal time correlation function

In coarsening phenomena, one observes interesting patterns. As discussed, such patterns exhibit statistical self-similarity [4]. This means, if the pattern at a given time is enlarged by a certain factor it will overlap with another pattern at a different time, in statistical sense. This property as well as the type of pattern can be studied via the two-point equal time correlation function, $C(r,t)$, defined in an isotropic situation as [4, 6]

$$C(r,t) =< \psi(\vec{r}_0+\vec{r},t)\psi(\vec{r}_0,t) > - < \psi(\vec{r}_0,t) >< \psi(\vec{r}_0+\vec{r},t) > . \quad (1.25)$$

In Eq. (1.25), $r = |\vec{r}|$ and the angular brackets correspond to statistical averaging, means averaging over different initial configurations as well as averaging for different choices of the reference point $\vec{r}_0$. When the above mentioned self-similarity exists, $C(r,t)$ shows scaling behavior as [4]

$$C(r,t) \equiv \tilde{C}(r/\ell(t)), \quad (1.26)$$

where $\tilde{C}$ is a time independent master function. This is demonstrated in Fig. 1.10. The overlap of the data from different times, mentioned in the

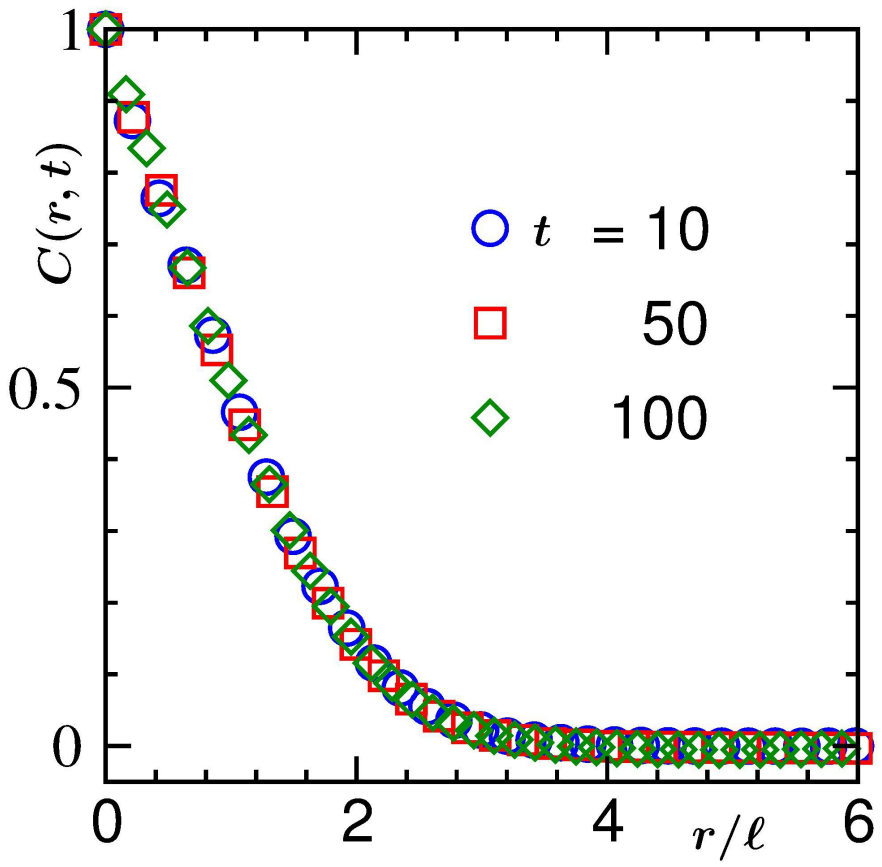

Figure 1.10: Plot of $C(r,t)$ vs $r/\ell(t)$, for the $d = 2$ TDGL equation. We have presented data from thee different times.

figure, lead to such a master curve. This multiplicative scaling property is consistent with the power-law growth of $\ell(t)$. One can measure the domain length from the decay of $C(r,t)$ as $C(r = \ell(t), t) = h_0$, where h_0 is constant.

This correlation function is useful in the studies of equilibrium critical phenomena as well. In the latter case, one can extract the correlation length ξ from its decay.

1.7.2 Structure factor

Instead of $C(r,t)$, experiments directly probe the structure factor [4], $S(k,t)$ ($k = |\vec{k}|$, being the scalar wave vector), the Fourier transform of $C(r,t)$:

$$S(\vec{k},t) = \int d\vec{r}\, e^{i\vec{k}\cdot\vec{r}}\, C(\vec{r},t). \tag{1.27}$$

Once again, for isotropic systems the quantity can be averaged over all directions for a fixed magnitude k of the wave vector. For self-similar patterns, the scaling property of $S(k,t)$ can be shown to be [4]

$$S(k,t) \equiv \ell^d(t)\tilde{S}[k\ell(t)], \tag{1.28}$$

where $\tilde{S}$ is another time independent master function and d is the dimensionality of the system. In the large k limit, $S(k,t)$ follows a power-law decay [4] as

$$S(k,t) \sim k^{-(d+n')}, \tag{1.29}$$

where n' is the number of components of the order-parameter. This is referred to as the Porod law [4], which is observed for sharp domain boundaries. For rough domain boundaries one observes slower decay of $S(k,t)$ than in Eq. (1.29), which has connection with the fractal dimensionality of the domain structure [21]. Similarly, in small k limit ($k \to 0$) also $S(k,t)$ follows power-law behavior, i.e., $S(k,t) \sim k^{\beta'}$, where again the exponent β' depends upon system dimensionality, in addition to its dependence on the conservation of order-parameter. It is understood that in the scaling regimes $\beta' = 0$ for nonconserved dynamics [22] and $\beta' = 4$ (for $d \geq 2$) for conserved dynamics

[22].

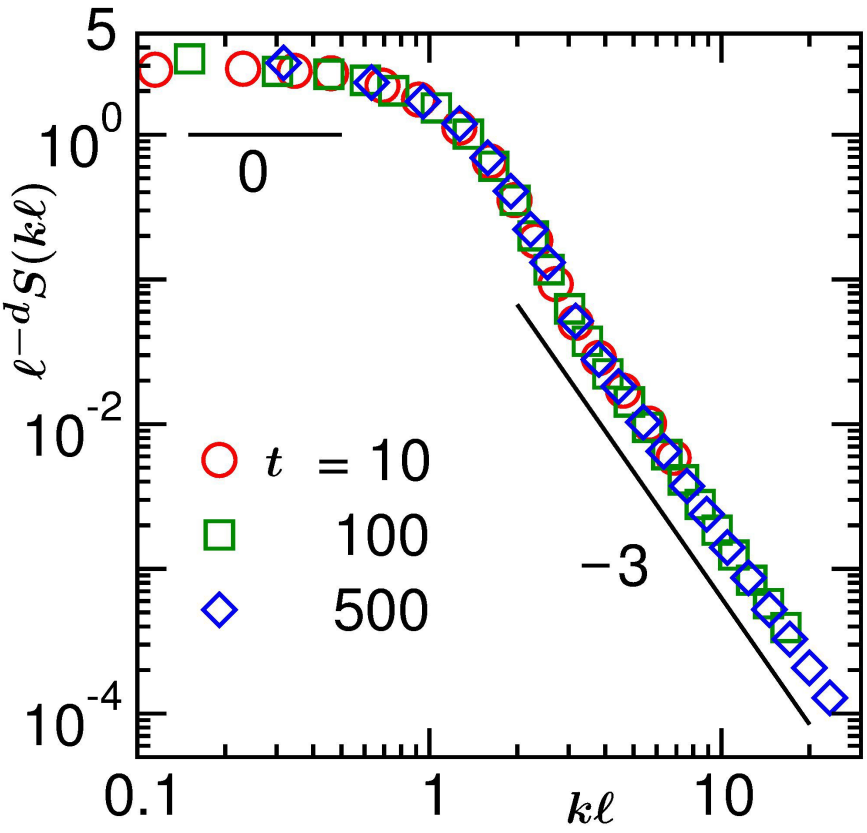

Figure 1.11: Scaling plot of the structure factor, $\ell^{-d}S(k\ell)$ vs $k\ell$, for the $d = 2$ TDGL equation. The solid lines correspond to power-laws with exponents 0 and -3.

In Fig. 1.11, we show the plot of $\tilde{S}[k\ell(t)]$, vs $k\ell$, for the $d = 2$ TDGL equation. There also we observe nice collapse of data from all the t values mentioned in the figure. In the large k limit, the data is consistent with the solid line with exponent -3, which is the expected Porod law. On the other hand, in the small k limit, the flat behavior of $S(k,t)$ implies $\beta' = 0$, as expected for nonconserved order-parameter dynamics. Inverse of the first moment of the structure factor also provides the domain length.

1.7.3 Two-time order-parameter autocorrelation function

In the out-of-equilibrium context, the two-time order-parameter autocorrelation function, $C(t, t_w)$, is used to study the aging dynamics [6, 24, 59]. This quantity is defined as [6]

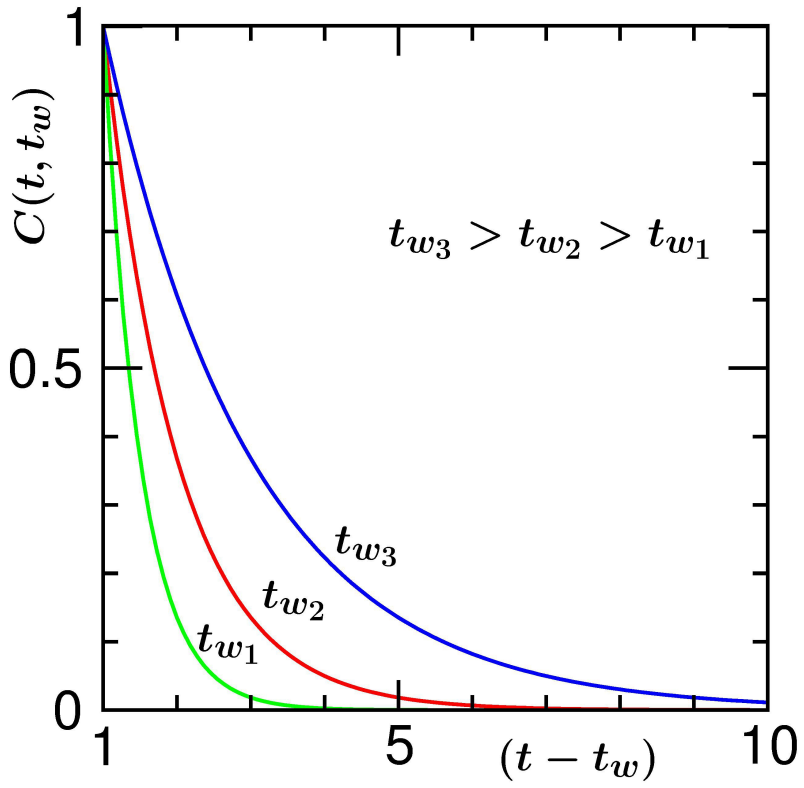

Figure 1.12: Plots of $C(t, t_w)$, vs the translated time, $(t - t_w)$, for different t_w values, are shown schematically, for coarsening dynamics.

$$C(t, t_w) = \langle \psi(\vec{r}, t)\psi(\vec{r}, t_w)\rangle - \langle \psi(\vec{r}, t)\rangle\langle \psi(\vec{r}, t_w)\rangle. \tag{1.30}$$

In Eq. (1.30), t is the observation time and t_w is the waiting time, often referred to as the age of a system. $C(t, t_w)$ goes to zero for $t >> t_w$. In equilibrium context autocorrelations of different types of current are often calculated to estimate various transport properties [54]. There such decay exhibits time translational invariance with respect to the translated time $(t - t_w)$, i.e., the decay of $C(t, t_w)$ is independent of the different choices of t_w. But, in nonequilibrium context, time-translation invariance property breaks down [6] due to slower decay of $C(t, t_w)$ with the increase of age, as schematically shown in Fig. 1.12. Such aging phenomena is of interest in kinetics of phase transitions, glassy systems and in other situations with slow relaxation. In kinetics of phase transitions, $C(t, t_w)$ exhibits scaling [22,24,57] as

$$C(t, t_w) \sim (\ell/\ell_w)^{-\lambda^{ag}}, \tag{1.31}$$

in the long time limit. In Eq. (1.31), ℓ and ℓ_w are the average domain lengths at times t and t_w, respectively. In this sub area, interest is in obtaining the full form of the autocorrelation function, as well as the exponent λ^{ag} for the late time decay. Understanding of this property is relatively poorer compared to that of domain growth.

1.7.4 Radius of gyration

If an object consists of N number of particles, (say, of equal mass) then the radius of gyration, R_g, is defined as [60, 61]

$$\begin{aligned} R_g &= \Big[\frac{1}{N}\sum_{i=1}^{N}(\vec{r}_i - \vec{r}_{\rm cm})^2\Big]^{1/2} \\ &= \Big[\frac{1}{N(N-1)}\sum_{i=1}^{N-1}\sum_{j=i+1}^{N}(\vec{r}_i - \vec{r}_j)^2\Big]^{1/2}, \end{aligned} \tag{1.32}$$

where $\vec{r}_{\rm cm}$ is the center of mass of the object and $\vec{r}_i$ is the position of the i'th particle. The total mass of the object, M, is connected to R_g as [62]

$$M \sim R_g^{d_f}. \tag{1.33}$$

In Eq. (1.33), the variation of M with R_g provides information about the compactness of the object [62]. For $d_f < d$ the object is a fractal one. To understand the growth of fractal structures, calculation of R_g becomes essential.

1.7.5 Center of mass of a composite object in periodic boundary conditions

The center of mass (CM) of a composite object is a unique point about which the entire mass is distributed in such a way that the application of an external force on that will generate only translational motion. For an

N-particle system the CM is calculated as [61]

$$\vec{r}_{\rm cm} = \frac{\sum_{i=1}^{N} m_i \vec{r}_i}{\sum_{i=1}^{N} m_i} = \frac{1}{N} \sum_{i=1}^{N} \vec{r}_i. \tag{1.34}$$

In the last step we assumed $m_i = m$ for all i.

Let us consider a situation where the mass is placed as shown in Fig. 1.13. In this case, if we calculate the CM in the typical way, using Eq. (1.34), it will be at C_1, which is indeed the correct position. But, in computer simulation, often we consider periodic boundary conditions to avoid surface effects. In that case, C_1 is not certainly the correct location of the CM. In such a situation, one way to calculate the CM of the object, using Eq. (1.34), is by shifting the particles in the right side of the box to the left, by appropriately translating x- coordinates of the particles. To achieve the objective this way, one may need to manually visualize the configurations, before instructing the computer program. On the other hand, this difficulty can easily be overcome in the following way, if one works in the polar coordinate system [63]. Let us define

$$\theta_i = 2\pi \frac{x_i}{L}, \tag{1.35}$$

where x_i is the x-component of the position vector $\vec{r}_i$ and L is the length of the box in the x-direction. This provides a new set of points

$$X_i = \cos\theta_i, \qquad\qquad Y_i = \sin\theta_i. \tag{1.36}$$

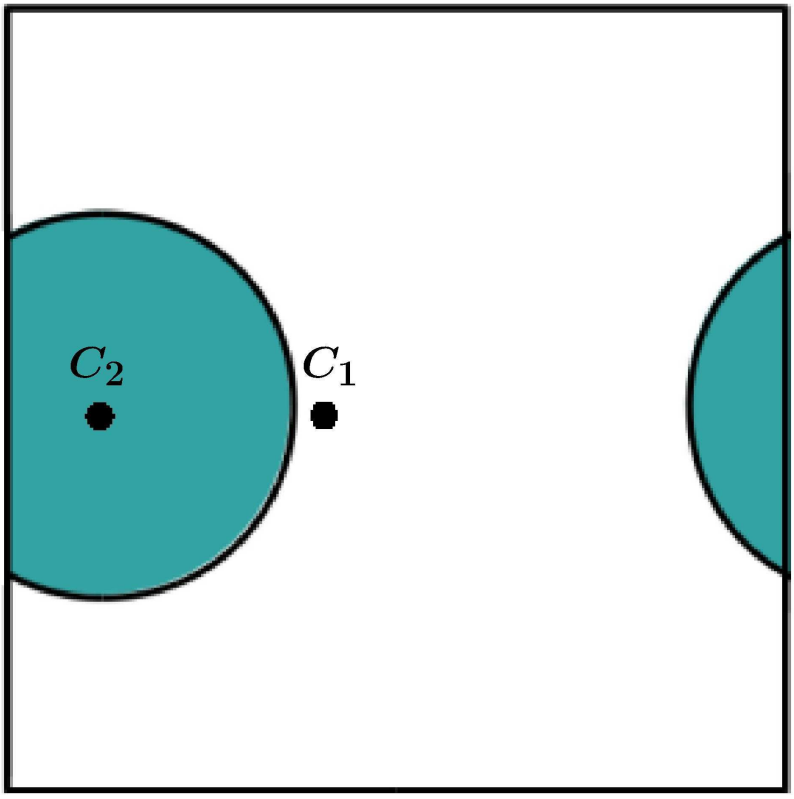

Figure 1.13: A liquid droplet is in a square box (of linear dimension L) under periodic boundary conditions. C_1 and C_2 are locations of the center of mass, obtained via different methods. See text for details.

Then we calculate the average of these two new quantities as

$$\bar{X} = \frac{1}{N}\sum_{i=1}^{N} X_i, \qquad \bar{Y} = \frac{1}{N}\sum_{i=1}^{N} Y_i, \tag{1.37}$$

and map these to a new coordinate $\bar{\theta}$ as

$$\bar{\theta} = \text{atan2}[-\bar{Y}, -\bar{X}] + \pi, \tag{1.38}$$

where the function atan2 computes angles between $-\pi$ to π, by taking care

of the signs of both $\bar{X}$ and $\bar{Y}$. Here, $\bar{\theta}$ is the correct value of CM in the polar coordinate system. Finally, the CM of the object in the Cartesian coordinate can be obtained as

$$x_{\rm cm} = L\frac{\bar{\theta}}{2\pi}. \tag{1.39}$$

In similar way one can calculate $y_{\rm cm}$ and $z_{\rm cm}$, for an object in $d = 3$. Now, using the above mentioned method, if we calculate the CM of the object in Fig. 1.13, it will be at C_2, which is the correct location of the CM in the presence of periodic boundary conditions.

1.8 Simulation methods

This thesis contains simulation studies of systems that exhibit phase transitions. Here we have looked at various types of phase transitions in the atomistic as well as coarse-grained levels, focusing on equilibrium and non-equilibrium aspects. Thus, different simulation methods became necessary. These we discuss below.

1.8.1 Euler discretization technique

The Euler discretization is a popular technique [64] for solving nonlinear ordinary or partial differential equations. It works in an iterative way via the discretization of total time into number of steps with small intervals δt. For illustration, let us consider a general differential equation

$$\frac{\partial\psi(\vec{r},t)}{\partial t} = f[\psi(\vec{r},t)], \tag{1.40}$$

where the value of ψ at $\vec{r}$ is known at a time t_0. Then we can obtain the value of ψ at a later time $t_0 + \delta t$ as

$$\psi(\vec{r}, t_0 + \delta t) = \psi(\vec{r}, t_0) + \delta t f[\psi(\vec{r}, t_0)]. \tag{1.41}$$

This way, one can obtain a reasonably accurate solution of Eq. (1.40) if δt is chosen to be very small. We have used this technique to solve the TDGL and the CH equations.

1.8.2 Monte Carlo simulation

In Statistical mechanics, the expectation value of a physical quantity $\mathcal{A}$ is defined as [39]

$$< \mathcal{A} >= \frac{\sum_i \mathcal{A}\ e^{-\beta E_i}}{\mathcal{Z}}, \tag{1.42}$$

where E_i is the energy in the ith state and $\mathcal{Z}$ is the partition function, defined as [39]

$$\mathcal{Z} = \sum_i e^{-\beta E_i}. \tag{1.43}$$

In both the above equations, the summations run over all states. Here, $\beta = 1/k_B T$, k_B being the Boltzmann constant. Even for very simple Hamiltonians, carrying out such calculations becomes nontrivial, analytically as well as computationally. As an example, let us consider the case of Ising model, on a square lattice in $d = 2$. The Hamiltonian for the model is given

in Eq. (1.5). On a computer, the calculation of $\mathcal{Z}$ even for a 10×10 lattice system requires dealing with $2^{100} \sim 10^{32}$ number of microstates. This difficulty can be overcome by using Monte Carlo (MC) simulations [39, 52]. There one draws N' microstates, from a given equilibrium distribution

$$p_i^{\rm eq} = \frac{1}{\mathcal{Z}} \exp[-\beta E_i], \tag{1.44}$$

following a Markovian chain process [39], which satisfy the detailed balance conditions (in equilibrium). Thus, the average of $\mathcal{A}$ can be obtained from MC simulations as [39]

$$\bar{\mathcal{A}} = \frac{1}{N'} \sum_{i=1}^{N'} \mathcal{A}_i, \tag{1.45}$$

$\mathcal{A}_i$ being the value for $i^{\rm th}$ state. Any statistical error that may occur will vanish when $N' \to \infty$.

The sampling of the phase space can be achieved by using Metropolis algorithm. The steps are the following [39].

1. Randomly select a state i with energy E_i.

2. Via a trial move go to a new state j with energy E_j.

3. Calculate the energy difference, $\Delta E = E_j - E_i$, between the two states.

4. Accept the trial move if $r_n < \exp(-\Delta E/k_B T)$, r_n being a random number between 0 and 1, taken from an uncorrelated set with uniform distribution.

This is the general procedure for MC simulation [39]. The specific trial moves for the Glauber and Kawasaki exchange cases have been mentioned

above. Below we discuss a more specialized case that has also been used in the thesis.

Gibbs ensemble Monte Carlo simulation

The Gibbs ensemble Monte Carlo (GEMC) [52, 65] simulation, devised by Panagiotopoulous, is an useful technique to calculate the phase coexistence of single or multicomponent fluids. Below we discuss the case for a single component system undergoing vapor-liquid transition. The GEMC simulation is performed in two separate boxes, viz., Box 1 and Box 2. The total number of particles, N ($= N_1 + N_2$, N_1 and N_2 being the number of particles in the Box 1 and Box 2, respectively), and total volume, V ($= V_1 + V_2$, V_1 and V_2 being the volumes of Box 1 and Box 2, respectively), remain fixed during entire period of a simulation. The thermodynamic requirements for phase coexistence are that the two boxes should maintain the internal equilibrium, i.e., the temperature, the pressure and the chemical potential of the two boxes should be equal. In this method, three types of perturbations or trial moves are considered, viz., particle displacements in each of the boxes, volume change of both the boxes and particle transfer between the boxes. These are schematically shown in Fig. 1.14. These moves will be accepted or rejected according to the Metropolis algorithm. Further discussion on the moves are given below.

Particle displacement: A particle is picked up randomly from Box 1 and provided a small displacement in a random direction. This trial move is

accepted with a probability

$$P_{\text{displacement}} = \min[1, \exp(-\beta \Delta E_1)], \tag{1.46}$$

where ΔE_1 ($= E_1^{\text{new}} - E_1^{\text{old}}$) is the energy difference between the states after and before the displacement of the particle in Box 1. Similarly, Eq. (1.46) is valid for moving a particle in Box 2.

Volume move: Suppose ΔV is the amount of volume increase in Box 1. As the total volume is fixed, then same amount of volume has to be decreased for Box 2. The acceptance criterion for this move is

$$P_{\text{volume}} = \min\Big[1, \exp\Big(-\beta \Delta E_1 - \beta \Delta E_2 + N_1 \ln \frac{V_1 + \Delta V}{V_1} + N_2 \ln \frac{V_2 - \Delta V}{V_2}\Big)\Big], \tag{1.47}$$

ΔE_1 and ΔE_2 being the energy changes in Box 1 and Box 2, due to the trial move.

Particle transfer: The acceptance criterion for particle transfer from Box 1 to Box 2 (or vice versa) is

$$P_{\text{transfer}} = \min\Big[1, \frac{N_1 V_2}{(N_2 + 1) V_1} \exp\Big(-\beta \Delta E_1 - \beta \Delta E_2\Big)\Big]. \tag{1.48}$$

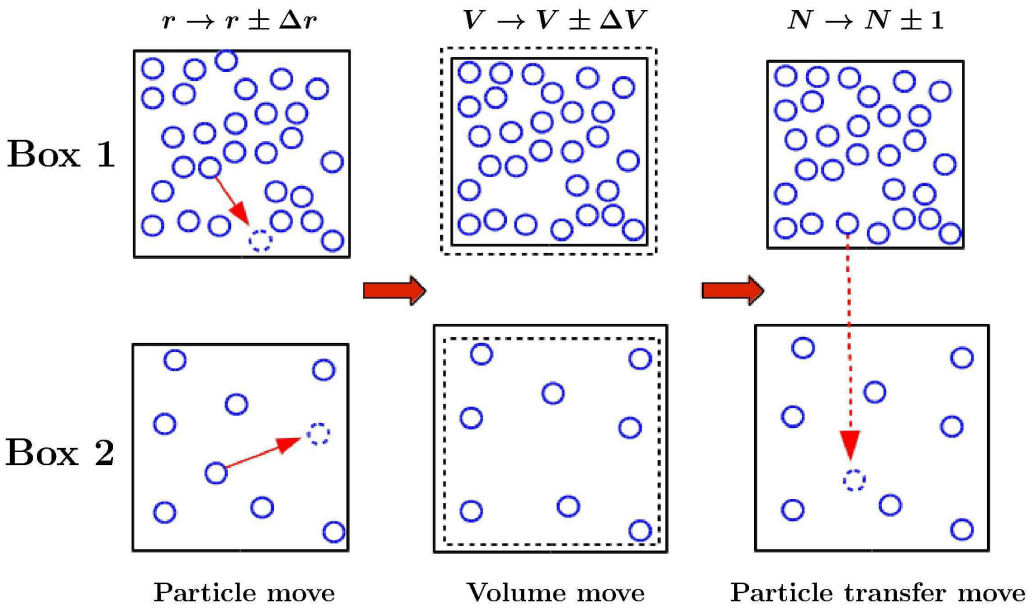

Figure 1.14: A schematic representation to show different trial moves in the Gibbs ensemble Monte Carlo simulation. The first column shows the particle displacement moves in each of the boxes, the middle one corresponds to the volume change of the boxes and the last column illustrates the particle transfer move between the boxes.

1.8.3 Molecular dynamics simulation

Molecular dynamics (MD) simulations [52, 53, 66] are commonly used to study dynamics in complex systems, at the atomistic level. In classical MD simulations, one essentially solves the Newton's equations of motion for a large number of particles interacting with each other via relevant potential. Although several techniques have been developed to solve these equations computationally, we will use the most popular Verlet-Velocity algorithm [52, 53]. In this method, to update the position and velocity of a particle i one

uses the equations (we set m_i, the mass of the ith particle, to unity)

$$x_i(t+\Delta t) = x_i(t) + \Delta t v_i^x(t) + \frac{\Delta t^2}{2} f_i^x(t), \tag{1.49}$$

and

$$v_i^x(t+\Delta t) = v_i^x(t) + \frac{\Delta t}{2}[f_i^x(t) + f_i^x(t+\Delta t)]. \tag{1.50}$$

Here, x_i and v_i^x are the x-component of the position and velocity of the ith particle, whereas $f_i^x(t)$ is the x-component of the force acting on the ith particle at time t, which can be calculated from the potential energy U_i, i.e., $\vec{f_i} = -\vec{\nabla} U_i$, assuming that there is no external force. Below a flow chart is given for MD simulation.

In this thesis we have performed MD simulations in NVE (microcanonical) ensemble as well as in NVT (canonical which keeps temperature constant) ensemble. In NVE simulations, the total energy of the system is constant although the potential and kinetic energies can fluctuate. In canonical ensemble, the temperature of a system is controlled by using a thermostat [52]. Essentially, the system is coupled with a heat reservoir. All the available thermostats control temperature to a good extent but only a few of them preserve hydrodynamics. Below we discuss different types of thermostats.

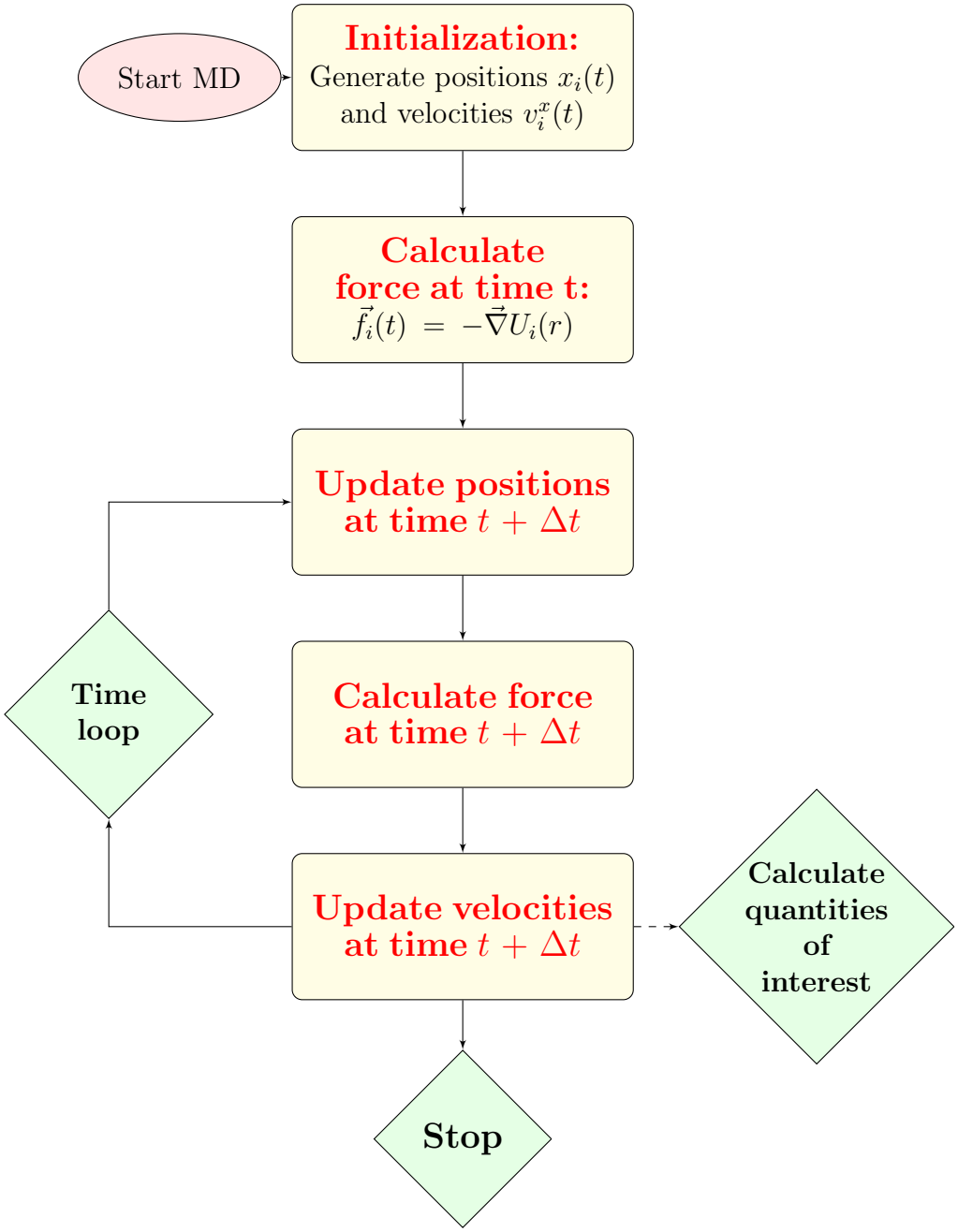

Flow diagram 1: This diagram explains the steps of a molecular dynamics simulation.

Andersen thermostat

Like Monte Carlo, the Andersen thermostat (AT) [52] is stochastic in nature and does not preserve hydrodynamics. The prescription for the AT is the following. At an MD step, one randomly selects some fraction of particles from the given system and draw their momentum from a Maxwellian distribution (m set to unity)

$$\mathcal{P}(v) = \Big(\frac{1}{2\pi k_B T}\Big)^{3/2} \exp\Big(-\frac{v^2}{2k_B T}\Big), \tag{1.51}$$

at the desired temperature [52]. This brings an imaginary coupling of the system with an external heat reservoir, maintained at a constant temperature T. The particles are thought to be hitting and exchanging their momentum with the heat reservoir. The strength of the coupling is controlled by a parameter Γ. In simulation, this can be implemented in two different ways:

1. At each MD step, a fixed percentage of particles, depending upon the value of Γ, is selected randomly and they are made to collide with the heat reservoir to exchange their momentum.

2. After a certain number of MD steps, again decided by the value of Γ, one allows all the particles to collide with the heat reservoir simultaneously. Both the ways are efficient to control the temperature and generate correct canonical ensemble properties of the system.

Lowe-Andersen thermostat

The Lowe-Andersen thermostat (LAT) [67, 68] is said to be a hydrodynamics preserving thermostat, the basic principle of which is similar to the AT. There, instead of selecting individual particles, pairs of particles (ij) with relative velocities $\vec{v}_{ij}$ $(= \vec{v}_i - \vec{v}_j$, $\vec{v}_i$ and $\vec{v}_j$ being the velocities of the ith and jth particle, respectively) are selected randomly. These particles are made to collide with heat reservoir, maintained at the assigned temperature T. The velocities of the particles are updated via the following equations:

$$\vec{v_i'}(t) = \begin{cases} \vec{v}_i(t) & \Gamma\Delta t < \xi_1 \\ \vec{v}_i(t) + \frac{\mu_{ij}}{m_i}\left[|\vec{v'}_{ij}| - \vec{v}_{ij}\cdot\hat{\sigma}_{ij}\right]\hat{\sigma}_{ij} & \Gamma\Delta t > \xi_1 \end{cases} \tag{1.52}$$

$$\vec{v_j'}(t) = \begin{cases} \vec{v}_j(t) & \Gamma\Delta t < \xi_1 \\ \vec{v}_j(t) - \frac{\mu_{ij}}{m_j}\left[|\vec{v'}_{ij}| - \vec{v}_{ij}\cdot\hat{\sigma}_{ij}\right]\hat{\sigma}_{ij} & \Gamma\Delta t > \xi_1. \end{cases} \tag{1.53}$$

Here, $\vec{v'}_i$ and $\vec{v'}_j$ are new velocities of the ith and jth particles, respectively, μ_{ij} $\left(= \frac{m_i m_j}{m_i + m_j}\right)$ is the reduced mass and $\hat{\sigma}_{ij}$ is the unit vector along the line joining the two particles. In the above equations, Γ is the coupling constant and ξ_1 is a random number between 0 to 1, drawn from a uniform distribution. The collision frequency $\Gamma\Delta t$ is compared with ξ_1. When $\Gamma\Delta t > \xi_1$, then one allows a selected pair of neighboring particles (i, j) to collide with the heat reservoir to maintain the temperature at a constant value. After collision, new set of velocities are assigned to the particles according to the relations noted down in second lines of these two equations. From these relations it is clear that local momentum remains conserved. Thus, this thermostat serves

the purpose of studies relating hydrodynamic effects.

Dissipative particle dynamics thermostat

The dissipative particle dynamics thermostat (DPDT) [52, 69] preserves hydrodynamics in the local scale like the LAT. In this method, there are three types of force acting on the particles, viz., dissipative force, $\vec{F}^D$, random force, $\vec{F}^R$, and conservative force, $\vec{F}^C$. Here $\vec{F}^D$ and $\vec{F}^R$ are not independent, they are connected via the fluctuation dissipation theorem with the assigned constant temperature of the system embedded in it. Thus, the net force on particle i is given by

$$\vec{f}_i = \sum_{j \neq i}^{N} (\vec{F}_{ij}^C + \vec{F}_{ij}^D + \vec{F}_{ij}^R), \tag{1.54}$$

where

$$\vec{F}_{ij}^C = -\vec{\nabla}\Big[u(r_{ij})\Big], \tag{1.55}$$

$$\vec{F}_{ij}^D = -w_0^D \omega^D(r_{ij})[\hat{\sigma}_{ij} \cdot \vec{v}_{ij}]\hat{\sigma}_{ij}, \tag{1.56}$$

and

$$\vec{F}_{ij}^R = w_0^R \omega^R(r_{ij})\theta_{ij}\hat{\sigma}_{ij}. \tag{1.57}$$

Here, $u(r_{ij})$ is the relevant interaction potential of the particles, $\vec{v}_{ij}$ is the relative velocity and $\hat{\sigma}_{ij}$ is the unit vector along the line joining the ith and jth particles. Further, w_0^R is the strength of the random force and w_0^D is the friction constant, and they satisfy the relation $[w_0^R]^2 = 2k_BTw_0^D$. In the

above equations, ω^D and ω^R are the space dependent weight functions, which satisfy

$$[\omega^R(r_{ij})]^2 = \omega^D(r_{ij}) = \begin{cases} 1 - r_{ij}/r_c & r < r_c \\ 0 & r \geq r_c. \end{cases} \tag{1.58}$$

The form in the last part of the equation is a popular choice, however, is not unique [70, 71]. In Eq. (1.57), θ_{ij} is a Gaussian white noise with zero mean and unit variance. It should be delta correlated in space and time as $< \theta_{ij}(t)\theta_{kl}(t') >= (\delta_{ik}\delta_{jl} + \delta_{il}\delta_{jk})\delta(t - t')$.

Nosé-Hoover thermostat

The idea of the Nosé-Hoover thermostat (NHT) [52, 72] comes from the extended Lagrangian formalism and was introduced by Nosé. Subsequently, improvement was made by Hoover. There, it is considered that the heat reservoir is an integral part of the original system. This provides an additional degree-of-freedom, "s", position of the imaginary heat reservoir, having the conjugate momentum, p_s. In addition to that, a parameter $Q = p_s/\dot{s}$ is introduced, which is the "effective mass" of the reservoir, often referred to as a coupling constant. The Hamiltonian of the combined system is written as

$$\mathcal{H}_{\text{Nose}} = \sum_{i=1}^{N} \frac{p_i^2}{2ms} + U + \frac{p_s^2}{2Q} + (3N + 1)k_B T \ln s. \tag{1.59}$$

Further, a new parameter, $\xi' = Q\dot{s}$, known as the friction parameter, is introduced. Following this, the equations of motion for NHT read as

$$\frac{d\vec{r}_i}{dt} = \vec{v}_i, \tag{1.60}$$

$$\frac{d\vec{v}_i}{dt} = -\frac{1}{m_i}\frac{\partial U(\vec{r}^N)}{\partial t} - \xi'\vec{v}_i, \tag{1.61}$$

$$\frac{d\xi'}{dt} = \Big(\sum_{i=1}^{N} m_i|\vec{v}_i|^2 - 3Nk_BT\Big)/Q, \tag{1.62}$$

$$\frac{d\ln s}{dt} = \xi'. \tag{1.63}$$

From the above set of equations it is clear that the friction parameter ξ' influences the velocity equation if the instantaneous temperature of the system deviates from the desired temperature. Whenever the instantaneous value tries to increase or decrease, the parameter ξ' always resists and brings it down to the assigned value. This way the temperature of the system fluctuates around the desired value. The strength of this fluctuation can be controlled by the coupling constant Q. It has been reported that NHT preserves the hydrodynamics and generates all the properties of canonical ensemble. Incorporating the above facts, the position and velocity update equations for NHT can be written as

$$x_i(t+\Delta t) = x_i(t) + v_i^x(t)\Delta t + \frac{\Delta t^2}{2}[f_i^x(t) - \xi'(t)v_i^x(t)], \tag{1.64}$$

and

$$\begin{aligned} v_i^x(t+\Delta t) &= v_i^x(t) + \frac{\Delta t}{2}\Big[f_i^x(t) + f_i^x(t+\Delta t) - 2\xi'(t)v_i^x(t)\Big] \\ &\quad - \frac{\Delta t^2}{2}\Big[\frac{\xi'(t)}{2}\Big(f_i^x(t) + f_i^x(t+\Delta t) - 2\xi'(t)v_i^x(t)\Big) \\ &\quad + v_i^x(t)\Big(\sum_{j=1}^{N} v_j^x(t)^2 - 3Nk_BT\Big)/Q\Big]. \end{aligned} \tag{1.65}$$

1.9 Overview of the thesis

Main objective of this thesis is to understand various equilibrium and nonequilibrium properties related to phase transitions of different types, viz., paramagnetic to ferromagnetic transition, solid-solid transition, vapor-solid transition and vapor-liquid transition. We have addressed questions related to dynamic critical phenomena as well as queries concerning domain growth and aging during phase transitions. For each of the problems, addressed in subsequent chapters, we have performed computer simulations. The simulation results are interpreted via finite-size scaling and/or other methods of analysis. These are compared with available theoretical predictions. In case of unavailability of such predictions, we made an effort to understand these by new analytical arguments or calculations. Since the synopsis contains brief descriptions of the problems, we do not repeat those here.

Bibliography

[1] H.E. Stanley, *Introduction to Phase Transitions and Critical Phenomena* (Oxford University Press, Oxford, 1971).

[2] K. Binder, in *Phase Transformation of Materials* ,edited by R.W. Cahn, P. Haasen, and E.J. Kramer (VCH, Weinheim, 1991), Vol. 5, p. 405.

[3] A. Onuki, *Phase Transition Dynamics* (Cambridge University Press, Cambridge, 2002).

[4] A.J. Bray, Adv. Phys. **51**, 481 (2002).

[5] R.A.L. Jones, *Soft Condensed Matter* (Oxford University Press, Oxford, 2008).

[6] S. Puri and V. Wadhawan (eds.), *Kinetics of Phase transitions* (CRC Press, Boca Raton, 2009).

[7] N. Goldenfeld, *Lectures On Phase Transition And The Renormalization Group*, (Perseus Books Publishing, Massachusetts, 1992).

[8] M. Plischke and B. Bergersen, *Equilibrium Statistical Mechanics* (World Scientific, Singapore, 2006).

[9] H. Haken, J.A.S. Kelso and H. Bunz, Biol. Cybern. **51**, 347 (1985).

[10] T. Vicsek, A. Czirók, E. Ben-Jacob, I. Cohen and O. Shochet, Phys. Rev. Lett. **75**, 1226 (1995).

[11] D. Layzer, *The Development of Order in the Universe* (Oxford Press, 1991).

[12] P.C. Hohenberg and B.I. Halperin, Rev. Mod. Phys. **49**, 435 (1977).

[13] M.E. Fisher, in *Critical Phenomena*, edited by M.S. Green (Academic, London, 1971) p1.

[14] K. Kawasaki, in *Phase Transition and Critical Phenomena*, edited by C. Domd and M.S. Green (Academic, New York, 1972), Vol. **2**, p.443.

[15] V. Privman, P.C. Hohenberg, and A. Aharony, in *Phase Transitions and Critical Phenomena*, edited by C. Domb and J.L. Lebowitz (Academic Press, New York, 1991), Vol. 14, Chap. I.

[16] M.A. Anisimov and J.V. Sengers, in *Equations of State for Fluids and Fluid Mixtures*, edited by J.V. Sengers, R.F. Kayser, C.J. Peters, and H.J. White, Jr., (Elsevier, Amsterdam, 2000) p. 381.

[17] S. Majumder and S.K. Das, Phys. Rev. E **81**, 050102 (R) 2010.

[18] J. Midya, S. Majumder and S.K. Das, J. Phys.: Condensed Matter **26**, 452202 (2014).

[19] S. Roy and S.K. Das, Soft Matter, **9**, 4178 (2013).

[20] S. Chakraborty and S.K. Das, Phys. Rev. E **93**, 032139 (2016).

[21] G.P. Shrivastav, V. Banerjee, S. Puri, Eur. Phys. J. E **37** 98 (2014).

[22] C. Yeung, M. Rao and R.C. Desai, Phys. Rev. E **53**, 3073 (1996).

[23] D.A. Huse, Phys. Rev. B, **40**, 304 (1989).

[24] D.S. Fisher and D.A. Huse, Phys. Rev. B, **38**, 373 (1989).

[25] N.V. Ter-Oganessian and V. P. Sakhnenko, J. Phys.: Condens. Matter, **22**, 226002 (2010).

[26] A. Albrecht and O.J. Steinhardt, Phys. Rev. Lett. **48**, 1220 (1982).

[27] H.C. Burstyn and J.V. Sengers, Phys. Rev. Lett. **45**, 259 (1980).

[28] R.A. Ferrell and J.K. Bhattacharjee, Phys. Lett. A **88**, 77 (1982).

[29] H.C. Burstyn and J.V. Sengers, Phys. Rev. A **25**, 448 (1982).

[30] R.A. Ferrell and J.K. Bhattacharjee, Phys. Rev. A **31**, 1788 (1985).

[31] G.A. Olchowy and J.V. Sengers, Phys. Rev. Lett. **61**, 15 (1988).

[32] R. Folk and G. Moser, Phys. Rev. Lett. **75**, 2706 (1995).

[33] J. Luettmer-Strathmann, J.V. Sengers, and G.A. Olchowy, J. Chem. Phys. **103**, 7482 (1995).

[34] S.K. Das, M.E. Fisher, J.V. Sengers, J. Horbach, and K. Binder, Phys. Rev. Lett. **97**, 025702 (2006).

[35] S.K. Das, J. Horbach, K. Binder, M.E. Fisher, and J.V. Sengers, J. Chem. Phys. **125**, 024506 (2006).

[36] S.Roy and S.K. Das, EPL **94**, 36001-p1 (2011).

[37] A. Onuki, Phys. Rev. E 55, 403 (1997).

[38] R. Folk and G. Moser, Phys. Rev. E **58**, 6246 (1998).

[39] D.P. Landau and K. Binder, *A Guide to Monte Carlo Simulations in Statistical Physics* (Cambridge University Press, Cambridge, 2009).

[40] K. Binder and D. Stauffer, Phys. Rev. Lett. **33**, 1006 (1974).

[41] S. Roy and S.K. Das, Phys. Rev. E **85**, 050602(R) (2012).

[42] R.J. Galuber, J. Math. Phys. **4**, 294 (1963).

[43] S.E. Allen and J.W. Cahn, Acta. Metall. **27**, 1085 (1979).

[44] J. Midya, S. Majumder and S.K. Das, Phys. Rev. E **92**, 022124 (2015).

[45] J.W. Cahn and J.I. Hilliard, J. Chem. Phys. **28**, 258 (1958).

[46] I.M. Lifshitz and V.V. Slyozov, J. Phys. Chem. Solids **19**, 35 (1961).

[47] H. Furukawa, Phys. Rev. A 31, 1103 (1985).

[48] H. Furukawa, Phys. Rev. A 36, 2228 (1987).

[49] E.D. Siggia, Phys. Rev. A **20**, 595 (1979).

[50] K. Binder and D. Stauffer, Adv. Phys. **25**, 343 (1976).

[51] S. Majumder and S.K. Das, EPL **95**, 46002 (2011).

[52] D. Frankel and B. Smit, *Understanding Molecular Simulations: From Algorithms to Applications* (Academic Press, San Diego, 2002).

[53] M.P. Allen and D.J. Tildesley, *Computer Simulations of Liquids* (Clarendon, Oxford, 1987).

[54] J.-P. Hansen and I.R. McDonald, *Theory of Simple Liquids* (Academic Press, London, 2008).

[55] M. San Miguel, M. Grant, and J.D. Gunton, Phys. Rev. A **31**, 1001 (1985).

[56] S. Ahmad, F. Corberi, S.K. Das, E. Lippiello, S. Puri and M. Zannetti, Phys. Rev. E **86**, 061129 (2012).

[57] F. Liu and G.F. Mazenko, Phys. Rev. B **44**, 9185 (1991).

[58] S.K. Das, S. Roy, S. Majumder and S. Ahmad, **97**, 66006 (2012).

[59] S. Majumder and S.K. Das, Phys. Rev. Lett. **111**, 055503 (2013).

[60] A.R. Khokhlov, A.Y. Grosberg, V.S. Pande, *Statistical Physics of Macromolecules* (AIP Press, New York, 1994, 350 p.)

[61] H. Goldstein, C. Poole, J. Safko, *Classical Mechanics (3rd ed.)*, (Addison-Wesley, New York, 2002).

[62] J. Midya and S.K. Das, arXiv:1604.06227.

[63] P. Schierz, J. Zierenberg, and W. Janke, J. Chem. Phys. **143**, 134114 (2015).

[64] J.C. Butcher, *Numerical Methods for Ordinary Differential Equations*, 2nd Edition (Willy, New York, 2003).

[65] A.Z. Panagiotopoulos, Molec. Phys. **61**, 813 (1987).

[66] D.C. Rapaport, *The Art of Molecular Dynamics Simulations* (Cambridge University Press, Cambridge, England, 2004).

[67] C.P. Lowe, Europhys. Lett, **47** 145 (1999).

[68] E.A. Koopman and C.P. Lowe, J. Chem. Phys. **124**, 204103 (2006).

[69] S.D. Stoyanov and R.D. Groot, J. Chem. Phys. **122**, 114112 (2005).

[70] T. Soddemann, B. Dünweg, and K. Kremer, Phys. Rev. E **68**, 046702 (2003).

[71] C. Pastorino, T. Kreer, M. Müller, and K. Binder, Phys. Rev. E **76**, 026706 (2007).

[72] S. Nosé, J. Chem. Phys. **81**, 511 (1984).

Chapter 2

Finite-size scaling study of dynamic critical phenomena in a vapor-liquid transition

2.1 Introduction

Understanding of the anomalous behavior of various static and dynamic quantities, in the vicinity of the critical points [1–24], is of fundamental importance. The critical behavior of the static quantities have been understood to a good extent via analytical theories, experiments and computer simulations [1–5, 7, 9]. On the other hand, the situation with respect to dynamics is relatively poor. Simulation studies, that helped achieving the objective for the static phenomena, gained momentum in the context of dynamic critical phenomena only recently [25–38]. Such a status is despite the fact that adequate information on the equilibrium transport phenomena is very much

essential for the understanding of even nonequilibrium phenomena like the kinetics of phase transitions [9,39]. For example, the crossovers and amplitudes in the growth-laws during phase transitions are often directly connected to the quantities like diffusivity and viscosity [39, 40].

The static correlation length, ξ, diverges at the critical point [2], i.e., $\xi \to \infty$ as the temperature $T \to T_c$, T_c being the critical point value for the latter. As a result, various other static as well as dynamics quantities show singularities in approach to the criticality. These singularities are of power-law type, in terms of the reduced temperature ($\epsilon = |T - T_c|/T_c$), such as [1–3, 5, 9]

$$\xi \sim \epsilon^{-\nu}, \quad \psi \sim \epsilon^{\beta}, \quad C \sim \epsilon^{-\alpha}, \quad \chi \sim \epsilon^{-\gamma}. \tag{2.1}$$

Here, ψ, C and χ are the order-parameter, specific heat and susceptibility, respectively. Typically, singularities for various dynamic quantities, viz., mutual or thermal diffusivity (D), shear viscosity (η), bulk viscosity (ζ), thermal conductivity (λ), etc., are expressed in terms of ξ as [4, 8, 11]

$$D \sim \xi^{-x_D}, \quad \eta \sim \xi^{x_\eta}, \quad \zeta \sim \xi^{x_\zeta}, \quad \lambda \sim \xi^{x_\lambda}. \tag{2.2}$$

The static critical exponents do not depend upon the choice of material and the type of transition. In a particular dimension (d), if the interaction among the particles or spins are of same type, i.e., either of short or long range, and the order parameters have the same number of components, the exponents will have the same values, giving rise to well defined universality classes. For short range interactions with one component order-parameters,

the exponents belong to the Ising universality class [1–3,5,6]. The universality of the critical exponents in statics, thus, is very robust, viz., paramagnetic to ferromagnetic, liquid-liquid, vapor-liquid transitions will all have the same set of exponent values depending upon the interaction range. Values of the above mentioned static exponents for the $d = 3$ Ising class are [6]

$$\nu \simeq 0.63, \quad \beta \simeq 0.325, \quad \alpha \simeq 0.11, \quad \gamma \simeq 1.239. \tag{2.3}$$

On the other hand, the universality of the dynamic exponents is considerably weaker. For example, the value of the exponent z, related to the longest relaxation time [7]

$$\tau \sim \xi^z, \tag{2.4}$$

can vary depending upon the choice of statistical ensemble [7–9]. Nevertheless, the exponents for liquid-liquid and vapor-liquid transitions should be same, given by the fluid or model H universality class [8–10]. The values of these exponents for this class are

$$x_{_D} \simeq 1.068, \quad x_{_\lambda} \simeq 0.902, \quad x_{_\eta} \simeq 0.068, \quad x_{_\zeta} \simeq 2.893. \tag{2.5}$$

These numbers are obtained via the dynamic renormalization group and mode-coupling theoretical calculations and found to be in agreement with experiments [8–24]. Like the static case, the dynamic exponents are also not all independent of each other, they follow certain scaling relations. E.g.

starting from the generalized Stokes-Einstein-Sutherland relation [2,9,19,41]

$$D = \frac{R_D k_B T}{6\pi\eta\xi}, \tag{2.6}$$

k_B being the Boltzmann constant and R_D another universal constant [19], one obtains [2]

$$x_{_D} = 1 + x_{_\eta}. \tag{2.7}$$

Unlike the static case, the computational estimation of the dynamic critical exponents started only recently, as mention above. In this work, we have presented simulation results for the critical dynamics of a three dimensional single component Lennard-Jones (LJ) fluid that exhibits vapor-liquid transition. We focus on the bulk viscosity and the thermal conductivity. There, of course, exist simulation studies on dynamics in vapor-liquid transitions [26, 28, 31, 42]. In fact, in some previous studies [26, 42] both these transport properties were calculated in the vicinity of critical points. However, presumably due to computational difficulty with respect to the calculation of collective transport properties, corresponding critical exponents were not quantified in those [26, 42] works. On the other hand, even though the critical behavior of the thermal diffusion constant was studied in Ref. [28], the associated conductivity was not separately looked at.

For this purpose, we have performed molecular dynamics (MD) simulations and analyzed the results via appropriate application of the finite-size scaling (FSS) theory [43]. Prior to that, we have studied the phase behavior of the model by using the Gibbs ensemble Monte Carlo (GEMC) simulation method [44] as well as successive umbrella sampling technique [45] in NPT

ensemble [46, 47] (N and P are the total number of particles and pressure, respectively). The critical temperature (T_c) and critical density (ρ_c) were estimated accurately via appropriate FSS analyses [48–50].

The rest of the chapter has been organized as follows. In section 2.2 we have discussed the model and methodologies. The results are presented in section 2.3. Finally, in section 2.4 we have summarized our results.

2.2 Model and Methods

As stated, we have considered a single component LJ fluid. In our model, a pair of particles, i and j, separated by a distance r ($= |\vec{r}_i - \vec{r}_j|$), interact via the potential [51]

$$\begin{aligned} U(r) &= u(r) - u(r_c) - (r - r_c)\frac{du}{dr}\Big|_{r=r_c}, \quad \text{for } r \leq r_c \\ &= 0, \quad \text{for } r > r_c, \end{aligned} \tag{2.8}$$

where r_c ($= 2.5\sigma, \sigma$ being the particle diameter) is a cut-off distance, introduced to accelerate the computation. In Eq. (2.8), $u(r)$ is the standard LJ potential [51, 52]

$$u(r) = 4\varepsilon\Big[\Big(\frac{\sigma}{r}\Big)^{12} - \Big(\frac{\sigma}{r}\Big)^{6}\Big], \tag{2.9}$$

with ε being the interaction strength. For the sake of convenience we set σ and ε to unity. The last term in the first part of Eq. (2.8) was introduced to correct for the discontinuity in the force at $r = r_c$ that occurs after the cutting and shifting of the potential.

The GEMC simulations [44, 52], for the study of the phase behavior

of the model, were performed in two separate boxes, as discussed below. The total number of particles in and the total volume (V) of the two boxes were kept fixed, though the numbers of particles (N_1 and N_2) in as well as the volumes (V_1 and V_2) of the individual boxes were varied during the simulations. We considered three types of perturbations or trial moves, viz., particle displacement in each of the boxes, volume change of the individual boxes and particle transfer between the boxes. Thus, this is a combination of simulations in constant NVT, NPT and $\mu_c VT$ ensembles, μ_c being the chemical potential. At a late time, one observes coexistence of the vapor phase (in one of the boxes) with the liquid phase (in the other box), if a simulation is performed at a temperature $T < T_c$. Thus, by running the simulations at different temperatures and obtaining the equilibrium densities ($\rho_\alpha = N_\alpha/V_\alpha$, α standing for liquid or vapor) of the individual phases, the whole phase diagram can be drawn, which, of course, will provide information about the critical temperature and critical density.

The phase diagram was also obtained via successive umbrella sampling [45] MC simulations in NPT ensemble [46,47]. Like the grandcanonical case, the overall density fluctuates in this ensemble as well. While in the former the fluctuation is a result of particle addition and deletion moves, in the case of NPT simulations the volume moves give rise to the fluctuation. The NPT ensemble has advantage over the former when overall density is rather high. In the implementation of successive umbrella sampling technique, for overall density $\in [0, 1]$, the corresponding volume range is divided into small windows. In each of these windows simulations were performed over long

periods of time. For $T < T_c$, these simulations provide double-peak distribution for specific volume $v_{\rm sp}$ $(= V/N)$. The peak at the smaller value of $v_{\rm sp}$, at a particular temperature, corresponds to a point on the liquid branch of the coexistence curve. The coexisting vapor density is given by the position of the peak at the higher value of $v_{\rm sp}$. While the coexistence curve data will be presented from the GEMC simulations, for the estimation of critical parameters, particularly ρ_c, we will rely on the simulations in NPT ensemble. Here note that our results on the phase behavior are consistent with the data from the simulations in grandcanonical ensemble which are made available online [53].

To study the transport properties we have performed MD simulations [51, 52, 54]. There we first thermalize the systems, using the stochastic Andersen thermostat [52], to generate the initial configurations. Finally, for the production runs we performed MD simulations in the microcanonical (constant NVE, E being the total energy) ensemble that preserves hydrodynamics, essential for the calculations of transports in fluids [52].

The transport quantities have been calculated by using the Green-Kubo (GK) formulae [41, 51]. The GK relations for the viscosities and the thermal conductivity are connected to the expressions [41, 51]

$$\mathcal{Y} = \frac{1}{k_B T V} \int_0^t dt' < \sigma'_{\mu s}(t') \sigma'_{\mu s}(0) >; \ \mu, s \in [x, y, z], \tag{2.10}$$

and

$$\lambda = \frac{1}{k_B T^2 V} \int_0^t dt' < j_T^s(t) j_T^s(0) >; \ s \in [x, y, z]. \tag{2.11}$$

In Eq. (2.10), $\sigma'_{\mu s}$ is related to the pressure tensor $\sigma_{\mu s}$, defined as

$$\sigma_{\mu s} = \sum_{i=1}^{N} \Big[m_i v_{i\mu} v_{is} + \sum_{j=i+1}^{N} (\mu_i - \mu_j) F_{sj} \Big], \tag{2.12}$$

where F_{sj} is the s^{th} component of the force on the j^{th} particle, m_i is the mass of the i^{th} particle (chosen to be equal to m for all), $v_{i\mu(s)}$ is the $\mu(s)^{\text{th}}$ component of velocity for particle i and $\mu_{i(j)}$ is the Cartesian coordinate for particle $i(j)$ along the μ-axis. For the diagonal elements $\sigma'_{\mu\mu} = \sigma_{\mu\mu} - < \sigma_{\mu\mu} >$ and $\mathcal{Y} = \zeta + 4/3\eta$, whereas for the off-diagonal elements ($\sigma'_{\mu s} = \sigma_{\mu s}$) $\mathcal{Y} = \eta$. In Eq. (2.11), j_T^s is the thermal flux along any particular axis, defined as

$$j_T^s = \frac{1}{2} \sum_{i=1}^{N} v_{is} \Big[m|v_i|^2 + \sum_{j \neq i}^{N} U(r) \Big] - \frac{1}{2} \sum_{i=1}^{N} \sum_{j \neq i}^{N} \vec{v}_i \cdot \vec{r} \frac{\partial U(r)}{\partial s}, \tag{2.13}$$

where v_{is} is the velocity component of the i^{th} particle along s-axis. In $U(r)$ it is understood that the energy comes from the interaction between particles i and j, vector distance between them being represented by $\vec{r}$. This justifies the summation over j in the last equation.

All our simulations were performed in cubic systems of linear dimension L and in the presence of periodic boundary conditions in all possible directions. In our MD simulations, time was measured in an LJ unit t_0 ($= \sqrt{m\sigma^2/\epsilon}$) and the integration time step was set to $dt = 0.005 t_0$. All the results related to transport properties are presented after averaging over 64 initial realizations. From here on, for the sake of convenience, we set m, k_B and t_0 to unity. Note that the time in MC simulations is expressed in units of number of Monte Carlo steps (MCS). In the case of GEMC method, each

step consists of 75% displacement moves, 10% volume moves, and 15% particle transfer moves, of a total of N trials. There was no particular order for the execution of these moves. Results for the coexistence curve are presented after averaging over 15 initial configurations.

2.3 Results

A. Phase Behavior

In Fig. 2.1 we show the density profiles inside the two boxes, vs time, obtained from a typical run in the GEMC simulations [44] at $T = 0.86$. For each of the studied temperatures, we started with density $\rho = 0.3$, in each of the boxes. Gradually, the density in one of the boxes increases with time, while it decreases in the other box, if $T < T_c$. Finally, the densities inside both the boxes saturate and fluctuate around the mean values, as shown in this figure. The distribution of the densities, obtained from the profiles in Fig. 2.1, has been presented in Fig. 2.2. The appearance of the two peaks is expected (given that the profiles are well separated) and implies the coexistence of vapor and liquid phases. There the locations of the peaks correspond to the equilibrium density values of the vapor and liquid phases, for the studied temperature.

In Fig. 2.3 we have presented the phase diagram for the model, in the temperature vs density plane. We obtained this by plotting the equilibrium coexistence densities of the two phases at different temperatures. Accuracy of these results are checked by comparing with the ones obtained from umbrella

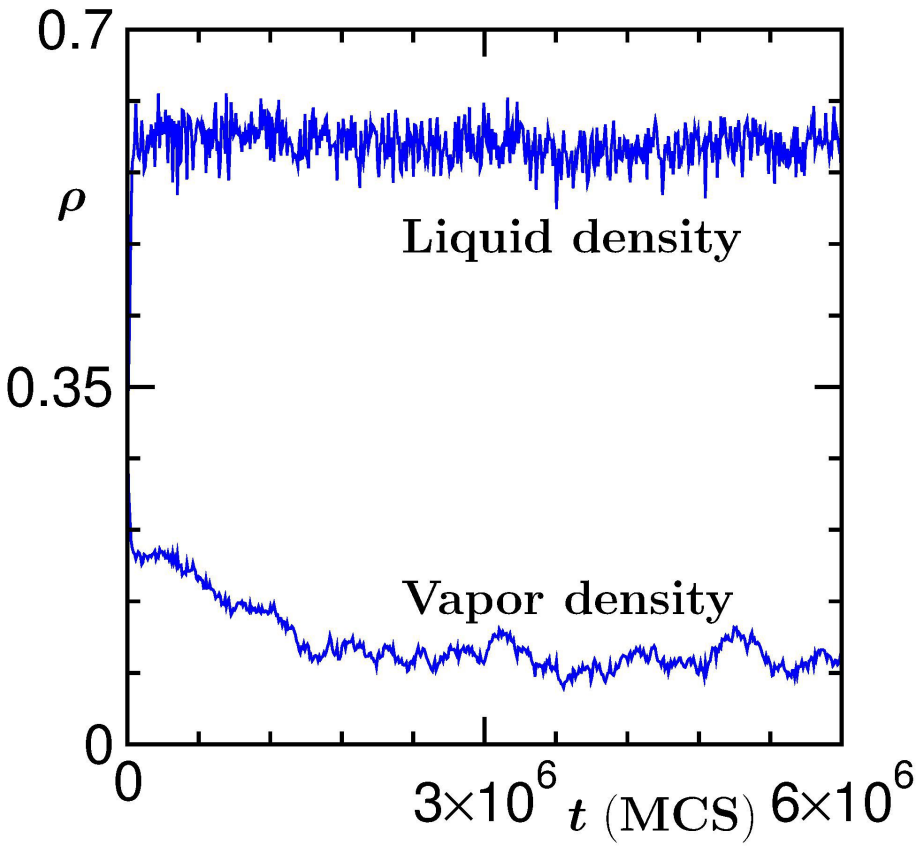

Figure 2.1: Density profiles inside the two boxes, during a Gibbs ensemble Monte Carlo run with $V = 2 \times 12^3$, are plotted vs time. The results correspond to $T = 0.86$.

sampling simulations in the NPT ensemble. From this figure, it is clear that the value of the order-parameter ψ ($= \rho_\ell - \rho_v$, ρ_ℓ and ρ_v being respectively the liquid and vapor densities) is approaching zero with the increase of temperature. In Fig. 2.3, we do not present data from temperatures very close to critical point, since they suffer from the finite-size effects. The finite-size effects were appropriately identified by comparing the results from different system sizes.

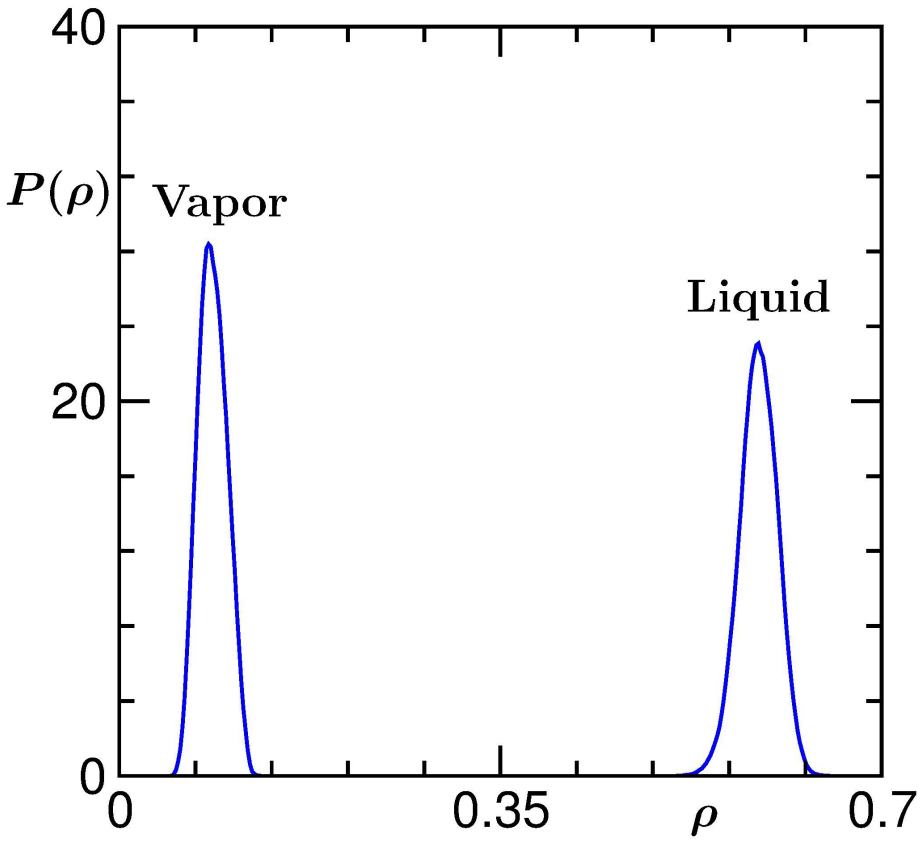

Figure 2.2: Plot of the density distribution function, $P(\rho)$, vs ρ, for the density profiles in Fig. 2.1.

The values of T_c and ρ_c can be calculated by using the equations [52]

$$\psi = \rho_\ell - \rho_v = A(T_c - T)^\beta, \tag{2.14}$$

and

$$\rho_d = \frac{\rho_\ell + \rho_v}{2} = \rho_c + B(T_c - T), \tag{2.15}$$

where A and B are constants. For fitting the simulation data to Eq. (2.14), to obtain T_c, we choose $\beta = 0.325$, which, as already mentioned, is its value for the $d = 3$ Ising universality class. Since LJ potential is a short-range

one, this value is expected. For the same reason, we will adopt the Ising value for ν, while analyzing the transport properties. This exercise provides $T_c = 0.939 \pm 0.004$. This is in good agreement with a previous estimate via grandcanonical simulations, for the same model [55].

Estimation of ρ_c, on the other hand, will suffer from error, if made via fitting to Eq. (2.15). This is because, Eq. (2.15) should contain additional terms in powers of $(T_c - T)$, due to field mixing [48–50]. Accurate finite-size scaling analyses [48, 49] have been performed to extract ρ_c, that take care of these singularities. In some of these previous studies [48, 55] only the term proportional to $\epsilon^{1-\alpha}$ have been considered. More recently, it has been stressed that the leading singularity [49, 50] is $\epsilon^{2\beta}$ and should be considered for more accurate estimation of ρ_c. Here we perform finite-size scaling analysis using this dominant contribution. For this exercise we have used data from NPT simulations at T_c. Recall that, like L in the grandcanonical ensemble, here N is kept fixed and we treat it as L^3.

In Fig. 2.4 we show ρ_d (upper curve) as a function of $L^{-2\beta/\nu(=1.032)}$. This scaling form comes from the fact that $\xi \sim L$ at T_c. Linear extrapolation of the data set to $L = \infty$ provides $\rho_c \simeq 0.317$. In this figure we have also included the mean value of ρ ($\bar{\rho}$) (see lower plot), estimated from the inverse of the average specific volume. This also exhibits a linear behavior, extrapolation of which leads to $\rho_c \simeq 0.315$. From these exercises we take $\rho_c = 0.316$. Given that the behavior of data for $\bar{\rho}$ is better we put more weight to the value obtained from its convergence and we will present transport quantities at $\rho = 0.315$. In Fig. 2.3, the cross mark is the location of the critical point. The simulation data in this figure show nice consistency with the continuous line,

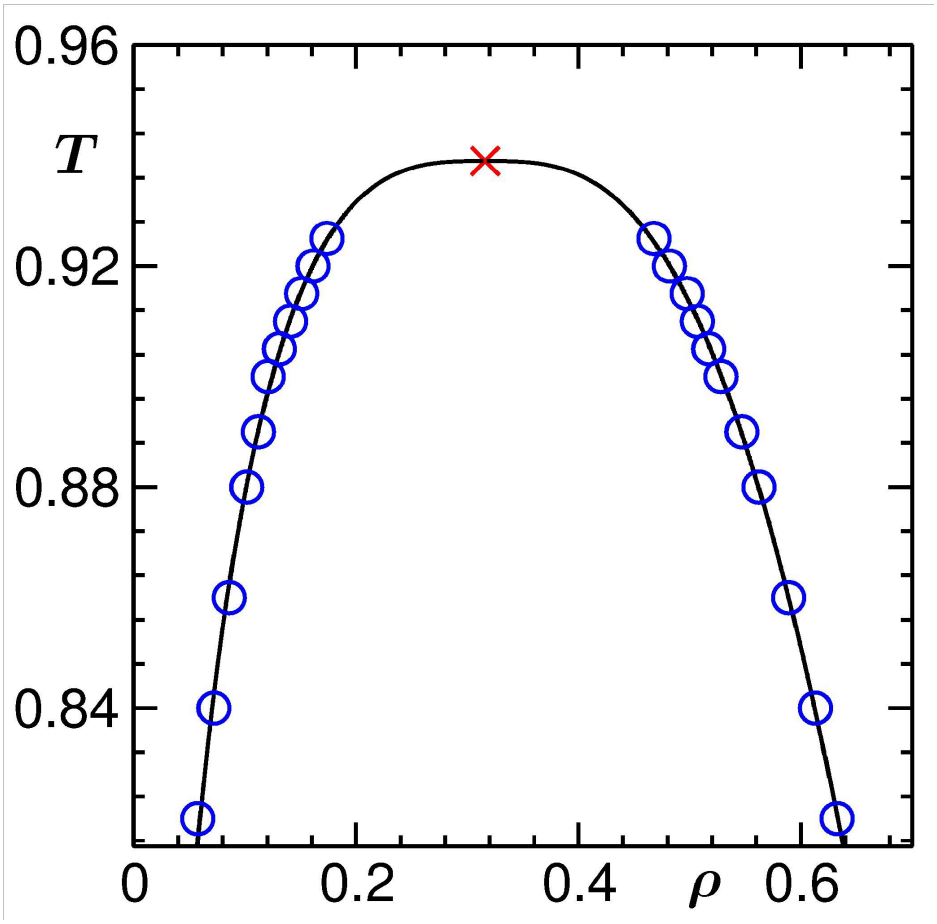

Figure 2.3: Phase diagram of the 3D LJ fluid in the $T - \rho$ plane, obtained via the Gibbs ensemble Monte Carlo simulations. The cross mark in the figure is the location of the critical point. The continuous line represents the Ising critical behavior of the order parameter. The results correspond to $V = 2 \times 12^3$.

which has the Ising behavior. Our estimation of ρ_c is reasonably consistent with the previous [55] grandcanonical estimate (0.320). Little more than 1% difference that exists may well be due to the fact that in this earlier work data were not analyzed by considering the leading singularity. Nevertheless, in view of this difference, we have calculated transport properties over a wide range of density, viz. $[0.31, 0.32]$. While we will present results at our

estimated value of ρ_c, outcomes from other densities will be mentioned in appropriate place.

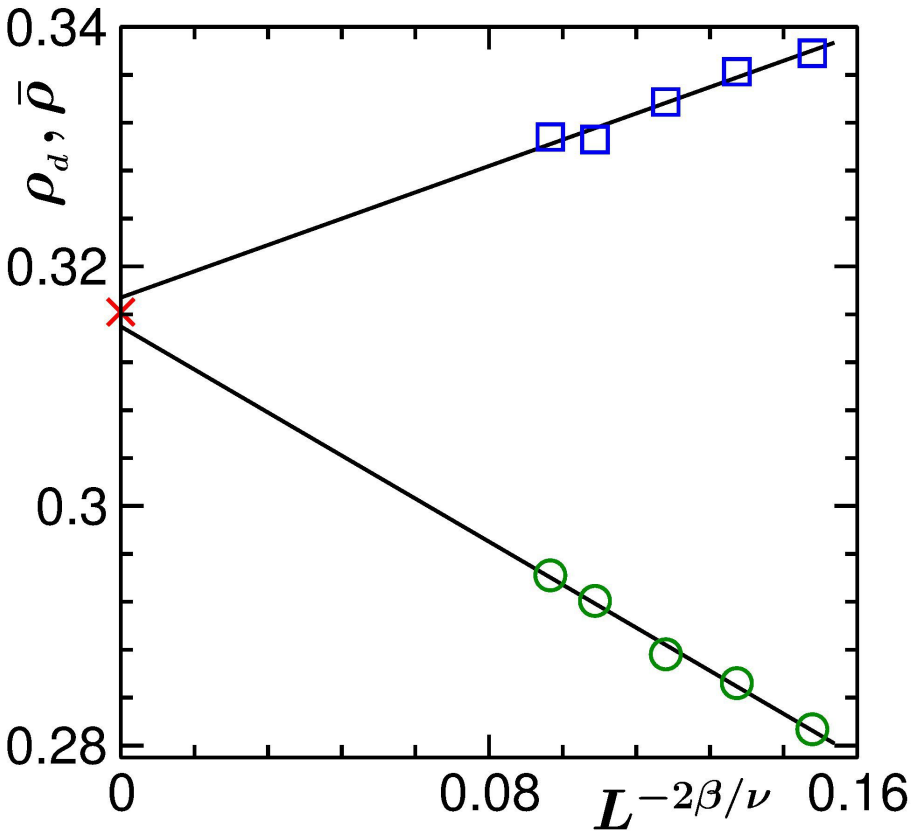

Figure 2.4: Demonstration of the estimation of ρ_c via finite-size scaling analysis. Here we have plotted ρ_d (upper curve) and $\bar{\rho}$ (lower curve), obtained from NPT simulations at T_c, vs $L^{-2\beta/\nu}$.

Note that the values of T_c and ρ_c were estimated previously [48, 52] for the vapor-liquid transitions in similar LJ models. However, those studies either used different values of r_c or did not consider the term related to force correction. The difference in the numbers between our study and these previous ones are related to these facts. In fact, the cut-off dependence of the critical temperature is nicely demonstrated by Trokhymchuk and Alejandre

[56]. However, we cannot use the information from this work because of the force correction that we use.

Before proceeding to show the results for dynamics, in Fig. 2.5 we show the two-dimensional cross-sections of two typical equilibrium configurations at $T = 0.95$ and 1.4. Structural difference between the two snapshots is clearly visible. The one at $T = 0.95$ shows density fluctuations at much larger length scale, implying critical enhancement in ξ. The values of ξ, as well as χ, can be calculated from the density-density structure factors by fitting the small wave-vector data to the Ornstein-Zernike form [2].

B. Dynamics

All the results for dynamics are presented from temperatures above the critical value, by fixing ρ to ρ_c. In Fig. 2.6, we show the plots of $\zeta + \frac{4}{3}\eta$ and λ, vs time, as obtained from the GK formulas, at $T = 0.96$, on a semi-log scale. We extract the final values for these quantities from the flat regions. From this figure it is clear that a transport quantity having higher critical exponent settles down to a flat plateau at a later time. This states about the difficulty of calculating a transport coefficient with strong critical divergence, like the bulk viscosity (ζ), particularly close to T_c. The difficulty gets pronounced with the increase of system size, consideration of which is essential to avoid the finite-size effects in the critical vicinity. However, in our simulations we have used relatively small system sizes and relied on the FSS theory [43] for the estimation of the critical exponents.

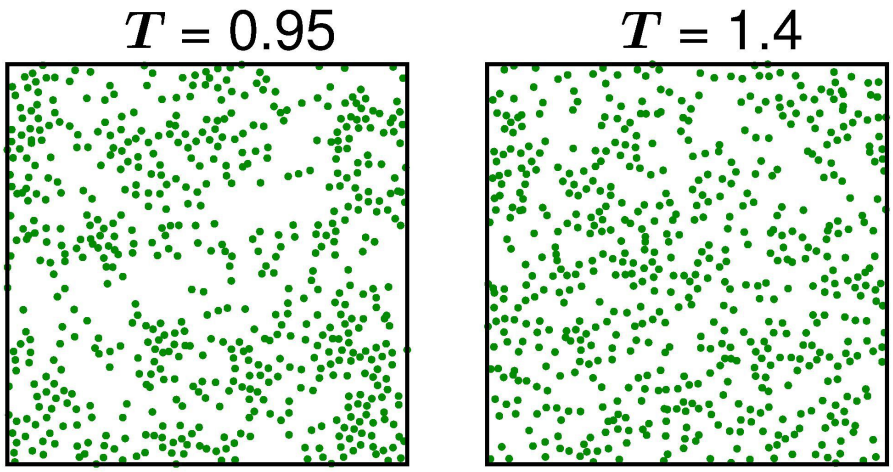

Figure 2.5: Two-dimensional slices of typical equilibrium configurations at $T = 0.95$ and 1.4. The dots mark the locations of the particles.

The temperature dependence of the bulk viscosity and the thermal conductivity, obtained from the plateaus of GK integrations, have been presented in Fig. 2.7 and Fig. 2.8, respectively. The enhancement in these quantities can be observed for both the presented system sizes, mentioned in the figure, close to T_c, represented by the dashed lines. Weaker enhancement for the smaller system, for both ζ and λ, signify finite-size effects.

In Fig. 2.9 we show the plot of ζ vs ϵ, using data from the larger system size that has been used in Fig. 2.7, on a log-log scale. We observe that the simulation data are in disagreement with the theoretically predicted solid line (having exponent $x_\zeta \nu = 1.82$). The reasons for the disagreement could be the finite-size effects as well as the presence of a background contribution [57], the latter arising from small wavelength fluctuations. We observe similar disagreement for λ, presented in the inset of Fig. 2.9, for the same system size. These two serious issues, viz., finite-size effects and background contributions,

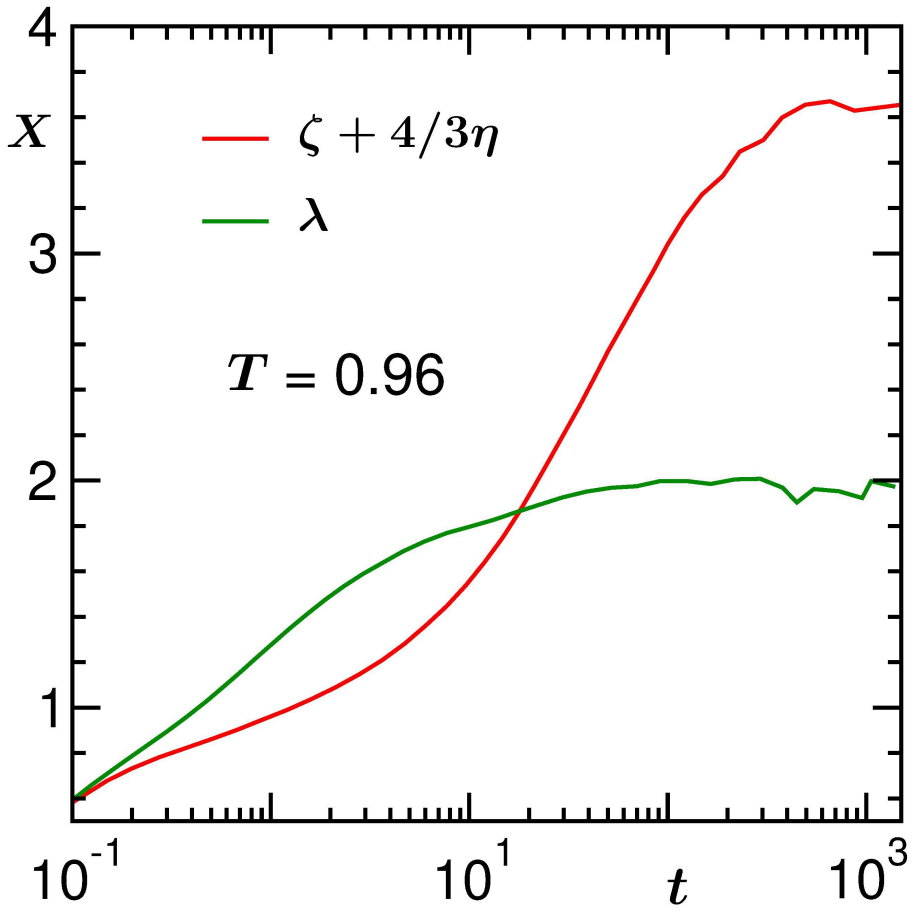

Figure 2.6: Plots $\zeta + \frac{4}{3}\eta$ and λ, vs t, in a semi-log scale, at $T = 0.96$, with $L = 30$.

have to be appropriately taken care of during the estimation of the critical exponents, along the line discussed below.

A quantity, say X, that exhibits singularity at the critical point, can be decomposed into two parts [19, 29, 30, 57] as

$$X = \Delta X(T) + X_{_b}, \tag{2.16}$$

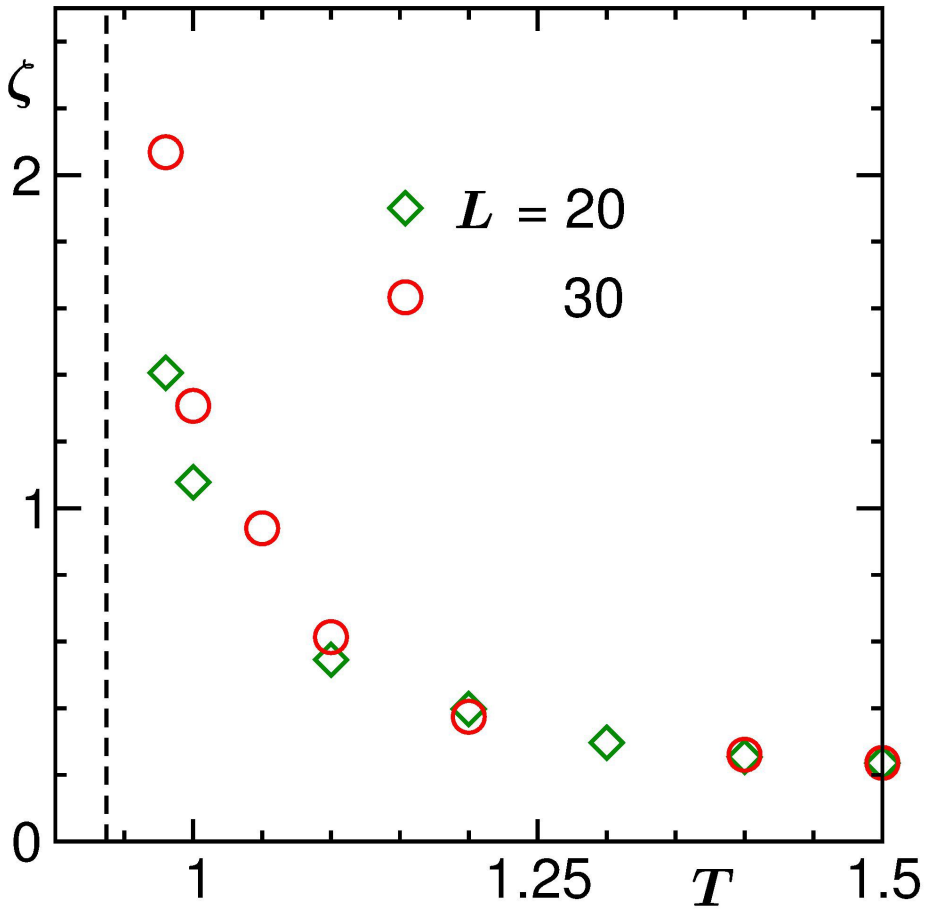

Figure 2.7: Plots of ζ vs T for two different system sizes. Close to the critical point the error bars are of the order of the symbol sizes. The dashed line in the figure is the location of the critical temperature.

where $\Delta X(T)$ comes from the critical fluctuations and is strongly temperature dependent. On the other hand, X_b, the background, is only weakly temperature dependent and is often treated as a constant [29, 30]. This latter contribution should also be independent of the system size. The presence of such a term, particularly in computer simulations, where one works with finite systems, can lead to a misleading conclusion. To extract the correct critical divergence one needs to subtract it appropriately from the total value,

such that

$$\Delta X(T) = X - X_b \sim \xi^x, \tag{2.17}$$

where x is the critical exponent for X. We have estimated X_b by treating it as an adjustable parameter in the FSS analysis that we describe below. One might as well have aimed to obtain the background contributions from Fig. 2.9 by looking at the behavior of the data sets far away from T_c. Even though these plots certainly provide hint on the presence of nonzero X_b, even a weak temperature dependence of the latter may cause significant error while analyzing data close to T_c, if estimated from high T convergence.

As stated above, at the critical point the correlation length is restricted by the system size, i.e., $\xi \sim L$ at $T = T_c$, so that [7]

$$\Delta X(T_c) \sim L^x. \tag{2.18}$$

Far from T_c, the finite-size effects will be absent, i.e., the data will be independent of L. To describe the thermodynamic limit ($L \gg \xi$) and finite-size limit data by a single equation, one should introduce a bridging or FSS function $Y(y)$, to write

$$\Delta X(T) \sim Y(y) L^x. \tag{2.19}$$

In Eq. (2.19), $Y(y)$ is independent of the system size and depends upon the scaling variable y ($= (L/\xi)^{1/\nu} \sim \epsilon L^{1/\nu}$), the latter being a dimensionless quantity. In the limit $y \to 0$, i.e., $T \to T_c$, Y must be a constant so that Eq. (2.18) is recovered. On the other hand, in the limit $y \to \infty$ ($\xi << L,\ \epsilon \gg 0$),

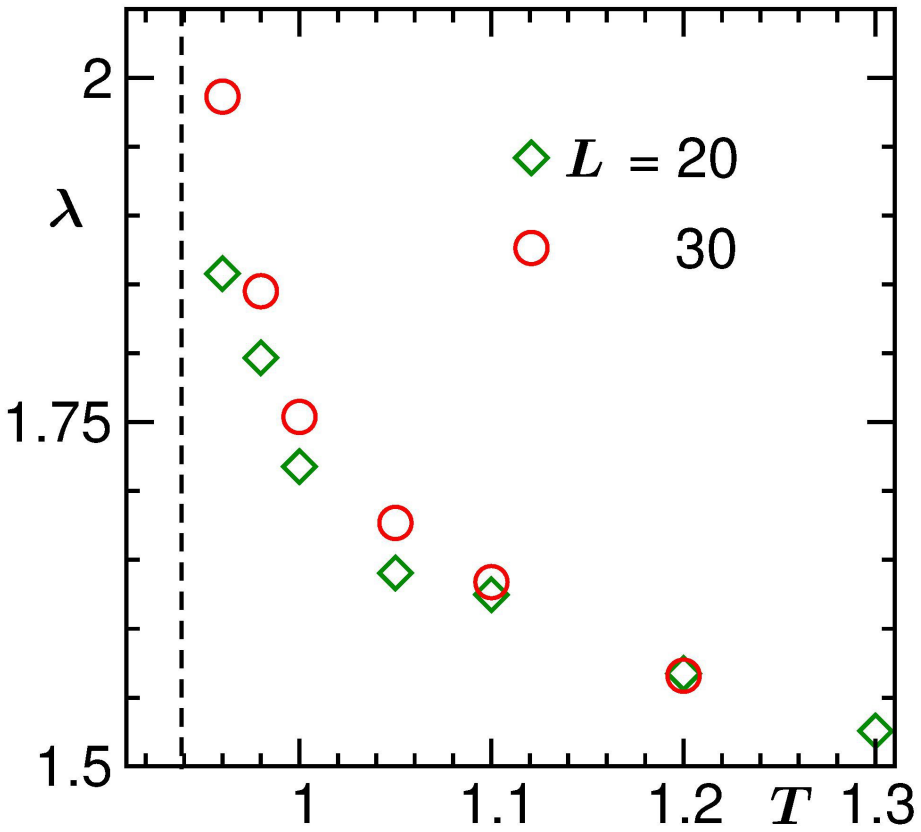

Figure 2.8: Plots of λ vs T. Data from two different system sizes are shown. Close to the critical point the error bars are of the order of the symbol sizes. The dashed line marks the location of the critical temperature.

Y should exhibit a power-law decay

$$Y(y) \sim y^{-x\nu}, \tag{2.20}$$

so that the data are described by Eq. (2.17). A plot of Y vs y, obtained by taking data from different system sizes, will exhibit data collapse, for appropriate choices of X_b, x and ν. Also, for the best data collapse, the large y behavior of Y will be consistent with Eq. (2.20).

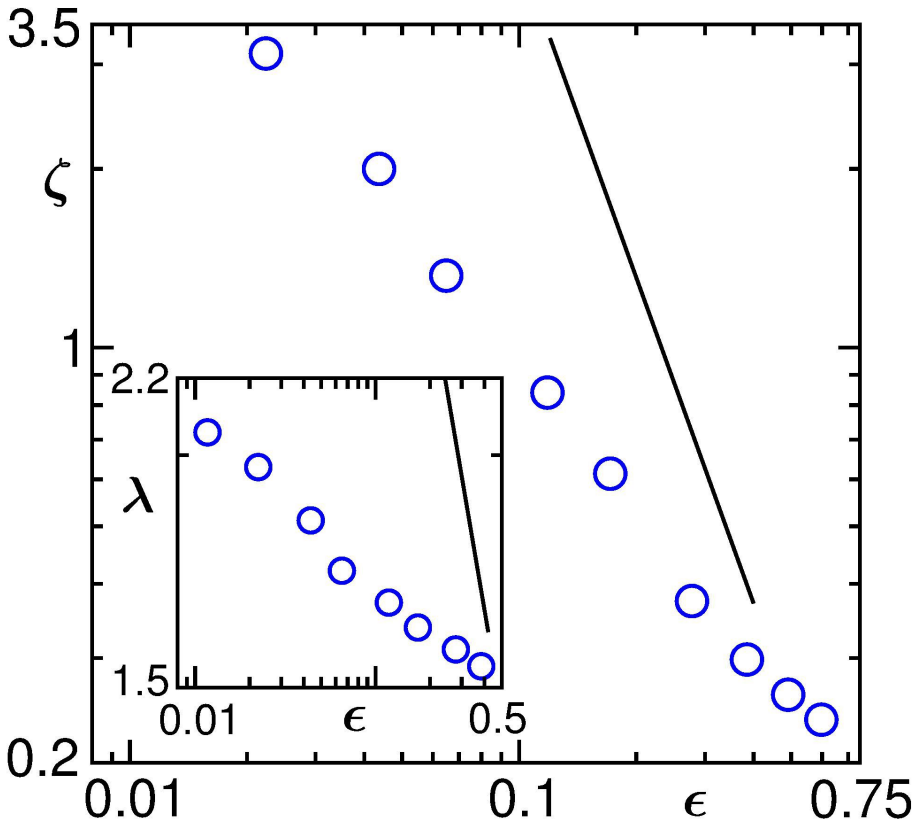

Figure 2.9: Plot of ζ vs ϵ, on a log-log scale, for $L = 30$. The solid line corresponds to the theoretical expectation. Inset shows the same exercise for λ.

In Fig. 2.10, we have presented the FSS analysis result for ζ, by plotting $Y(y)$ vs y, using data from different system sizes, mentioned on the figure. To show consistency with the theoretical predictions, in this analysis we have used ζ_b (background contribution for ζ) as adjustable parameter and fixed ν and x_ζ to their theoretical values. The presented result corresponds to best collapse which is obtained for $\zeta_b = 0.40$. Given the difficulty one encounters in calculating bulk viscosity, even a reasonably better collapse would require significant additional effort. In the limit $y \to 0$, the master curve approaches

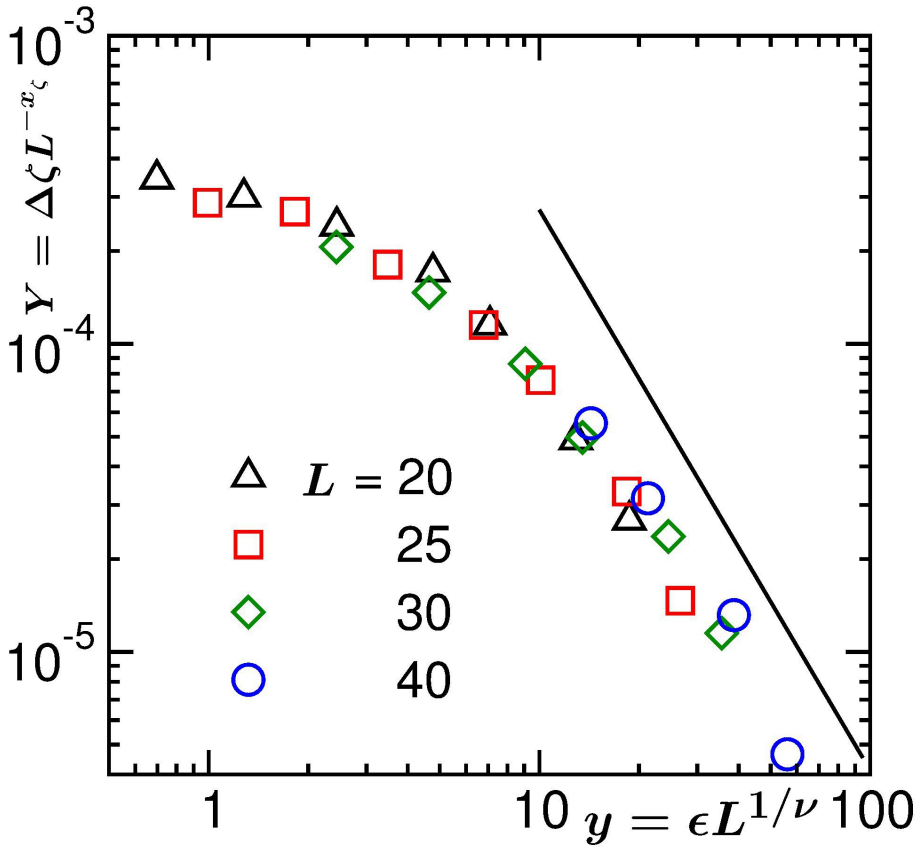

Figure 2.10: Finite-size scaling plot for the bulk viscosity. The scaling function Y $(= \Delta\zeta L^{-x_\zeta})$ is plotted vs the scaling parameter y $(= \epsilon L^{1/\nu})$, on a log-log scale, using data from different system sizes. The solid line in the figure corresponds to the theoretical expectation.

a constant value, as expected from the construction of Y. On the other hand, for $y \to \infty$, the master curve is showing a power-law decay with the exponent $x_\zeta \nu = 1.82$. Similar exercise we have performed for λ, the results for which are presented in Fig. 2.11. Here note that, since $\Delta\lambda \sim T\epsilon^{-0.57}$, the ordinate contains the factor T^{-1}. In this case we have obtained best collapse for $\lambda_b = 1.34$.

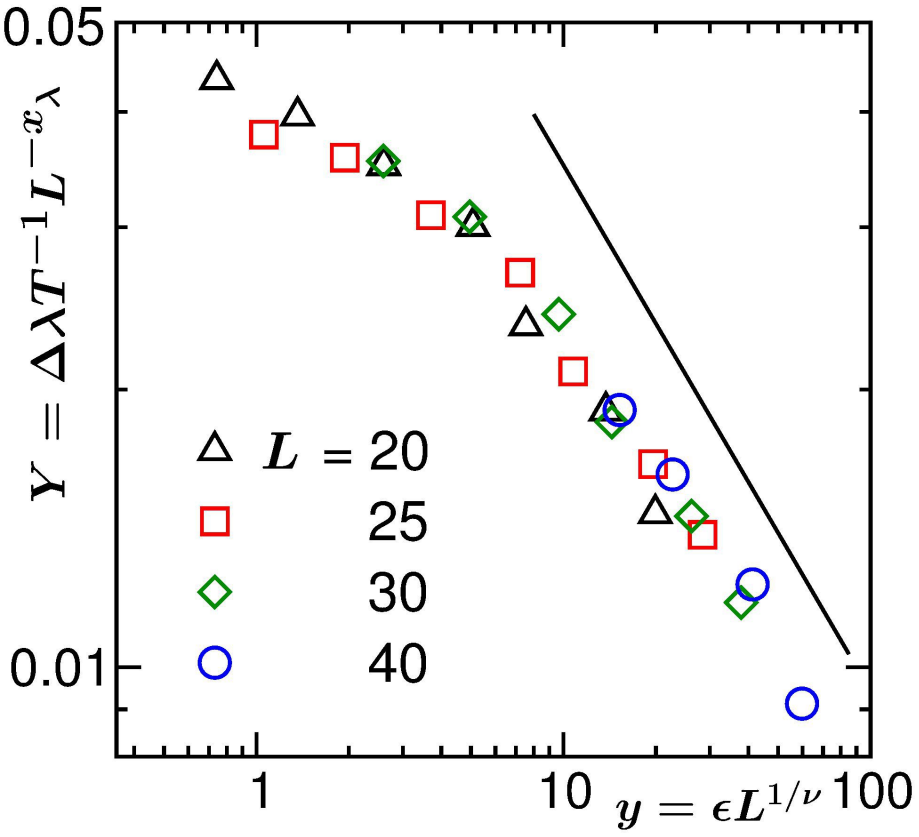

Figure 2.11: Finite-size scaling exercise for the thermal conductivity. Here we show Y $(= \Delta\lambda T^{-1} L^{-x_\lambda})$ vs y $(= \epsilon L^{1/\nu})$ on a log-log scale. The solid line in the figure corresponds to the theoretical expectation.

2.4 Summary

We have studied the phase behavior and the dynamic critical phenomena for vapor-liquid transition in a single component Lennard-Jones fluid in space dimension $d = 3$. The phase behavior was obtained via Monte Carlo simulations [44]. To study the dynamic critical phenomena, we performed molecular dynamics simulations [51, 52, 54] in microcanonical ensemble. The Green-Kubo relations [41] were used to calculate the transport quantities, viz., the bulk viscosity and the thermal conductivity. We observe strong

finite-size effects, similar to the case of liquid-liquid transitions [29, 32]. Our finite-size scaling analyses, however, show that that the simulation data are consistent with the theoretically predicted critical divergences. In fact, to the best of our knowledge, this is the first time the critical exponents for bulk viscosity and thermal conductivity have been quantified for a vapor-liquid transition.

Our results, along with the ones for the binary fluid [29, 32], are compatible with the expectation that the dynamic critical phenomena of the vapor-liquid and liquid-liquid transitions belong to the same universality class, defined by model H [8]. Here note that the theoretical numbers for x_ζ for vapor-liquid and liquid-liquid transitions are slightly different [23, 24]. This difference is within the error bars of computation via molecular dynamics.

Despite the similar critical exponents in vapor-liquid and liquid-liquid transitions, we have observed some differences between the two cases. Our observation of the critical range in this work is less wide compared to that of the liquid-liquid transition [29, 32]. We also have observed that the background contribution for the bulk viscosity is nonzero (though small), whereas in the liquid-liquid transition it was not needed in the analysis [32]. Similarly, for thermal conductivity the background term plays very important role. These differences may have some connection with the symmetry of the model in the liquid-liquid case, but further investigations will be needed to confirm it.

Bibliography

[1] M.E. Fisher, Rep. Prog. Phys. **30**, 615 (1967).

[2] H.E. Stanley, *Introduction to Phase Transitions and Critical Phenomena* (Oxford University Press, Oxford, 1971).

[3] M.E. Fisher, Rev. Mod. Phys. **46**, 597 (1974).

[4] V. Privman, P.C. Hohenberg, and A. Aharony, in *Phase Transitions and Critical Phenomena*, edited by C. Domb and J.L. Lebowitz (Academic Press, New York, 1991), Vol. 14, Chap. I.

[5] M.E. Fisher, Rev. Mod. Phys. **70**, 653 (1998).

[6] J. Zinn-Justin, Phys. Rep. 344, 159 (2001).

[7] D.P. Landau and K. Binder, *A Guide to Monte Carlo Simulations in Statistical Physics* (Cambridge University Press, Cambridge, 2009).

[8] P.C. Hohenberg and B.I. Halperin, Rev. Mod. Phys. **49**, 435 (1977).

[9] A. Onuki, *Phase Transition Dynamics (Cambridge University Press*, Cambridge, England, 2002).

[10] J.V. Sengers and R.A. Perkins, "Fluids near critical points", in *Transport Properties of Fluids: Advances in Transport Properties*, edited by M.J. Assael, A.R.H. Goodwin, V. Vesovic, and W.A. Wakeham (IUPAC, RSC Publishing, Cambridge, 2014), pp. 337-361.

[11] M.A. Anisimov and J.V. Sengers, in *Equations of State for Fluids and Fluid Mixtures*, edited by J.V. Sengers, R.F. Kayser, C.J. Peters, and H.J. White, Jr., (Elsevier, Amsterdam, 2000), p. 381.

[12] L. Mistura, J. Chem. Phys. **62**, 4571 (1975).

[13] H.C. Burstyn and J.V. Sengers, Phys. Rev. Lett. **45**, 259 (1980).

[14] R.A. Ferrell and J.K. Bhattacharjee, Phys. Lett. A **88**, 77 (1982).

[15] H.C. Burstyn and J.V. Sengers, Phys. Rev. A **25**, 448 (1982).

[16] R.A. Ferrell and J.K. Bhattacharjee, Phys. Rev. A **31**, 1788 (1985).

[17] G.A. Olchowy and J.V. Sengers, Phys. Rev. Lett. **61**, 15 (1988).

[18] R. Folk and G. Moser, Phys. Rev. Lett. **75**, 2706 (1995).

[19] J. Luettmer-Strathmann, J.V. Sengers, and G.A. Olchowy, J. Chem. Phys. **103**, 7482 (1995).

[20] A. Onuki, Phys. Rev. E 55, 403 (1997).

[21] R. Folk and G. Moser, Phys. Rev. E **58**, 6246 (1998).

[22] H. Hao, R.A. Ferrell, and J.K. Bhattacharjee, Phys. Rev. E. **71**, 021201 (2005).

[23] J.K. Bhattacharjee, I. Iwanowski, and U. Kaatze, J. Chem. Phys. **131**, 174502 (2009).

[24] J.K. Bhattacharjee, U. Kaatze, and S.Z. Mirzaev, Rep. Prog. Phys. **73**, 066601 (2010).

[25] K. Jagannathan and A. Yethiraj, Phys. Rev. Lett. **93**, 015701 (2004).

[26] K. Meier, A. Laesecke, and S. Kabelac, J. Chem. Phys. **122**, 014513 (2005).

[27] K. Jagannathan and A. Yethiraj, J. Chem. Phys. **122**, 244506 (2005).

[28] A. Chen, E.H. Chimowitz, S. De, and Y. Shapir, Phys. Rev. Lett. **95**, 255701 (2005).

[29] S.K. Das, M.E. Fisher, J.V. Sengers, J. Horbach, and K. Binder, Phys. Rev. Lett. **97**, 025702 (2006).

[30] S.K. Das, J. Horbach, K. Binder, M.E. Fisher, and J.V. Sengers, J. Chem. Phys. **125**, 024506 (2006).

[31] K. Dyer, B.M. Pettitt, and G. Stell, J. Chem. Phys. **126**, 034501 (2007).

[32] S. Roy and S.K. Das, Europhys. Lett. **94**, 36001 (2011).

[33] M. Gross and F. Varnick, Phys. Rev. E **85**, 056707 (2012).

[34] S. Roy and S.K. Das, J. Chem. Phys. **139**, 064505 (2013).

[35] S. Roy and S.K. Das, J. Chem. Phys. **141**, 234502 (2014).

[36] S. Roy and S.K. Das, Eur. Phys. J. E **38**, 132 (2015).

[37] S. Roy, S. Dietrich, and F. Höfling, J. Chem. Phys. **145**, 134505 (2016).

[38] J.W. Mutoru, W. Smith, C.S. O'Hern, and A. Firozabadi, J.Chem. Phys. **138**, 024317 (2013).

[39] A.J. Bray, Adv. Phys. **51**, 481 (2002).

[40] H. Furukawa, Phys. Rev. E **36**, 2288 (1987).

[41] J.-P. Hansen and I.R. McDonald, *Theory of Simple Liquid*s (Academic Press, London, 2008).

[42] D.J. Searles, D.J. Evans, H.J.M. Hanley and S. Murad, Molecular Simulation **20**, 385 (1998).

[43] M.E. Fisher, in *Critical Phenomena*, edited by M.S. Green (Academic Press, London) 1971, p. 1.

[44] A.Z. Panagiotopoulos, Molec. Phys. 61, 813 (1987).

[45] P. Virnau and M. Mller, J. Chem. Phys. **120**, 10925 (2004).

[46] N.B. Wilding and K. Binder, Physica A **231**, 439 (1996).

[47] A.Z. Panagiotopoulos, J. Phys.: Condens. Matter **12**, R25 (2000).

[48] N.B. Wilding, J. Phys.: Condens. Matter **9**, 585 (1997).

[49] Y.C. Kim, E. Luijten and M.E. Fisher, Phys. Rev. Lett. **91**, 065701 (2003).

[50] C.A. Cerdeiria, G. Orkoulas and M.E. Fisher, Phys. Rev. Lett. **116**, 040601 (2016).

[51] M.P. Allen and D.J. Tildsely, *Computer Simulations of Liquids* (Clarendon, Oxford, 1987).

[52] D. Frankel and B. Smit, *Understanding Molecular Simulations: From Algorithms to Applications* (Academic Press, San Diego, 2002).

[53] https://www.nist.gov/mml/csd/ chemical-informatics-research-group/ sat-tmmc-liquid-vaor-coexistence-properties-linear-2.

[54] D.C. Rapaport, *The Art of Molecular Dynamics Simulations* (Cambridge University Press, Cambridge, England, 2004).

[55] J.R. Errington and P.G. Debenedetti, J. Chem. Phys. **118**, 2256 (2003).

[56] A. Trokhymchuk and J. Alejandre, J. Chem. Phys. **111**, 8510 (1999).

[57] H.C. Burstyn, J.V. Sengers, J.K. Bhattacharjee, and R.A. Ferrell, Phys. Rev. A **28**, 1567 (1983).

Chapter 3

Droplet growth during vapor-liquid transition in a 2D Lennard-Jones fluid

3.1 Introduction

When a homogeneous system is quenched inside the miscibility gap, it falls unstable to fluctuations and moves towards the new equilibrium via the formation and growth of particle-rich and particle-poor domains [1–5]. In addition to being of interest from the fundamental scientific point of view, understanding of associated phenomena has many important technological consequences [4]. The nature of a domain pattern is quantitatively studied via, among other quantities, the two-point equal time correlation function,

which, in an isotropic situation, has the definition [4, 5] ($r = |\vec{r}|$)

$$C(r,t) =< \psi(\vec{0},t)\psi(\vec{r},t) > - < \psi(\vec{r},t) >^2, \tag{3.1}$$

where ψ is a space ($\vec{r}$) and time (t) dependent order-parameter. The angular brackets in Eq. (3.1) are related to the statistical averaging, involving space and initial configurations. Typically, during the growth, the structures at different times are self-similar [4, 5] (in statistical sense). As a consequence, $C(r,t)$ exhibits the scaling property [4, 5]

$$C(r,t) \equiv \tilde{C}(r/\ell). \tag{3.2}$$

In Eq. (3.2), ℓ is the average size of the domains or clusters, which usually exhibits power-law growth with time as [1, 2, 4, 5]

$$\ell \sim t^{\alpha}. \tag{3.3}$$

The exponent α depends upon the system and order-parameter dimensionality [4, 5], transport mechanism [4–13], order-parameter conservation [4, 5], as well as the type of pattern [9–11, 14].

For a vapor-liquid transition, relevant nonequilibrium order-parameter can be constructed from the local density field $\rho_{\vec{r}}(t)$. We define $\psi(\vec{r},t) = \rho_{\vec{r}}(t) - \rho_c$, the latter being the (equilibrium) critical density. Integration of this scalar quantity over the whole system remains constant with time. For quenches close to ρ_c, say via the variation of temperature (T), one expects an interconnected domain structure [4, 5, 14, 15]. On the other hand, close

to the coexistence curve, one of the phases (liquid or vapor) fails to percolate [9,10,14,16,17]. There has been significant recent interest in the kinetics with such morphology [14, 16–26]. For overall density close to the vapor branch, circular or spherical liquid droplets, depending upon the system dimension (d), nucleate [27–29]. Associated problems have direct relevance in the context of cloud physics [30, 31].

The above mentioned droplets should retain their shape while growing [14, 18, 19]. During phase separation in solid binary mixtures [4, 8], such droplets, formed by the minority particles in an asymmetric composition, are typically static [21] and growth in the system occurs via an evaporation-condensation mechanism, proposed by Lifshitz and Slyozov (LS) [8]. In this mechanism, particles from a smaller droplet get detached, to be diffusively deposited on a larger droplet. The value of α in that case is 1/3, irrespective of the value of d. In fluids, on the other hand, these droplets are expected to move [9, 10, 14]. For the diffusive motion of the droplets and coalescence following collisions, the growth law is predicted by Binder and Stauffer (BS) [9–11]. For this mechanism, solution of the equation [11]

$$\frac{dn}{dt} = -Bn^2, \tag{3.4}$$

n being the droplet density ($\propto 1/\ell^d$) and B a constant, provides

$$\alpha = \frac{1}{d}. \tag{3.5}$$

The right side of Eq. (3.4) is related to the collision frequency. Assuming

that the collisions are sticky, this is equated with dn/dt. For the mechanism under discussion, B is a product of ℓ and the droplet diffusivity D, the latter being a function of ℓ. This product can be treated as a constant, accepting the validity of the generalized Stokes-Einstein-Sutherland relation [32, 33]. The value of B, however, may have dependence upon temperature [32, 33]. This will modify the growth amplitude, depending upon the depth of quench.

Though the growth exponent in Eq. (3.5) was predicted for the liquid-liquid transitions, it was recently shown [14, 18, 19], from studies in $d = 3$, that even for the vapor-liquid transitions this theory works, if the background vapor density is reasonably high with long range fluctuations. But in $d = 3$, the value of the exponent is same as the LS one. Thus, $d = 2$ provides a better ground for the confirmation of the mechanism, since the BS value is different in this dimension from the LS one.

In this chapter we study the kinetics of phase separation in a single component Lennard-Jones (LJ) system, via the molecular dynamics (MD) simulations [34,35] in $d = 2$. For a very low overall density, at temperatures reasonably close to the critical value, we observe nucleation and growth of circular liquid droplets in the vapor background. Via the calculation of the mean-squared-displacements (MSD) of the centers of mass (CM) of the droplets we confirmed their diffusive motion. It has been shown that between collisions, the change in the number of particles in a droplet is negligible, implying growth via the inter-droplet collisions. Finally, the exponent $\alpha = 1/2$, as predicted by BS [9, 10], is observed. For choosing a region of interest inside the miscibility gap, appropriate knowledge of the coexistence curve becomes essential. This we have obtained via the Monte Carlo simulations [36].

3.2 Model and Methods

In our model, particles i and j, at a distance r from each other, interact via [35]

$$U(r) = u(r) - u(r_c) - (r - r_c)\frac{du}{dr}\Big|_{r=r_c}, \tag{3.6}$$

where $u(r)$ is the standard LJ potential [35]

$$u(r) = 4\varepsilon\Big[\Big(\frac{\sigma}{r}\Big)^{12} - \Big(\frac{\sigma}{r}\Big)^{6}\Big], \tag{3.7}$$

σ being the particle diameter and ε the interaction strength. The cut-off distance r_c ($= 2.5\sigma$), in Eq. (3.6), was introduced to facilitate faster computation. The discontinuity in the force, thus appears, was taken care of by the introduction of the last term in Eq. (3.6).

The phase behavior, along with the critical values for temperature (T_c) and density, were obtained via the Gibbs ensemble Monte Carlo (GEMC) simulation method [34, 36, 37]. For the kinetics, we have performed MD simulations in the canonical ensemble, using various hydrodynamics preserving thermostats [34, 38–41], the results from all of which match with each other. For the sake of convenience, we present results only from the Nosé-Hoover thermostat (NHT) [34] which controls the temperature better.

The GEMC simulations [34] were performed in two boxes, for each combination of T and ρ, the latter being the overall density. There we have allowed three different types of trial moves, viz., particle displacements in and volume change of each of the boxes, as well as particle transfer from one

box to the other, by keeping the total number (N) of the particles and total area (V) of the boxes fixed. We have fixed the overall density ($\rho = N/V$) to a value 0.3. This procedure, in the long time limit, leads to different constant density profiles (with fluctuations around the mean values) for the two boxes, one corresponding to the vapor phase and the other to the liquid phase, if the chosen temperature is below the critical value. The phase diagram was obtained by plotting these mean values as a function of temperature.

All the simulations for kinetics were performed in periodic square boxes with area $V = L^2$, L (= 2048 in units of σ) being the linear system dimension. Other than the snapshots, the results are presented after averaging over at least 15 independent initial configurations. Unless otherwise mentioned, for all the simulations, we fixed ρ to 0.03 and T to $0.35\varepsilon/k_B$. Time in our MD simulations was measured in units of $\sqrt{m\sigma^2/\varepsilon}$, where m is the mass of the particles. From here on, for the sake of convenience, we set m, σ, ε and k_B to unity.

For the calculation of the $C(r,t)$, used for the verification of the self-similarity property [5] and obtaining the values of ℓ, we have mapped the continuum systems onto the (square) lattice ones. If the density (calculated by considering the nearest neighbors) at a lattice point is higher than the critical value, ψ is assigned the value $+1$, otherwise -1. We have obtained the values of ℓ from

$$C(\ell, t) = 0.25, \tag{3.8}$$

as well as from the first moment of the domain size distribution function,

$P(\ell_d, t)$ [15], as

$$\ell = \int \ell_d \; P(\ell_d, t) \; d\ell_d, \tag{3.9}$$

where ℓ_d is the distance between two successive interfaces along any direction. Results from the two methods are proportional to each other. Except for Fig. 3.4, we have used ℓ from Eq. (3.9).

3.3 Results

In Fig. 3.1 we show the coexistence curve, in T vs ρ plane, for the model system. The circles are from the GEMC simulations [34, 37]. The values of T_c and ρ_c were estimated via appropriate analyses of the simulation data, by using the facts (A and A' are constants)

$$\rho_\ell - \rho_v = A(T_c - T)^\beta, \tag{3.10}$$

and

$$\frac{\rho_\ell + \rho_v}{2} = \rho_c + A'(T_c - T), \tag{3.11}$$

where ρ_ℓ and ρ_v are the densities along the (higher density) liquid and the (lower density) vapor branches of the coexistence curve, respectively. In the fitting exercises (using the above equations) we have set β to 1/8, the $d = 2$ Ising critical exponent for the order parameter. Given the short range of the LJ interaction, it is expected that our model will belong to the Ising critical universality. This exercise provides $T_c = 0.415 \pm 0.005$ and $\rho_c = 0.350 \pm 0.005$,

represented by the cross. The continuous line in Fig. 3.1 represents the Ising critical behavior, with which the simulation data are in nice agreement.

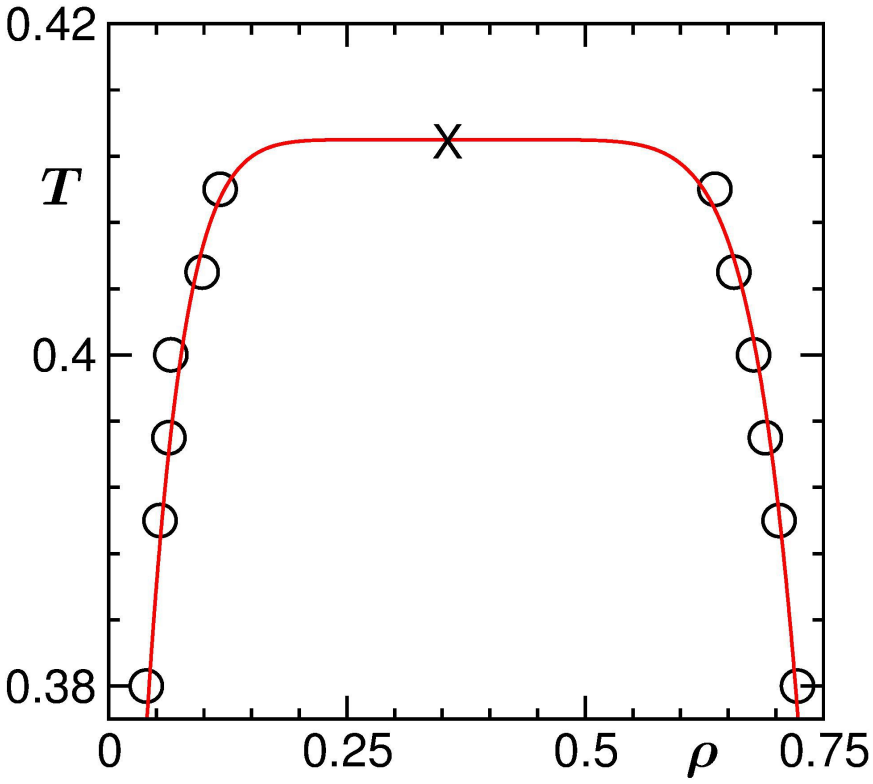

Figure 3.1: Vapor-liquid coexistence curve for the considered two-dimensional ($2D$) Lennard-Jones fluid, in temperature vs density plane. The circles are from the Gibbs ensemble Monte Carlo simulations and the continuous curve is obtained by fitting the simulation data to the theoretical form corresponding to the criticality in the $2D$ Ising model. The cross mark is the location of the critical point. For the simulation results we have used $V = 1250$.

Fig. 3.2 shows the evolution snapshots following the quench of a high temperature homogeneous system, with $\rho = 0.03$, to $T = 0.35$. Here note that, because of the very low overall density, nucleation of stable droplets [27, 28] requires fluctuations over long distances. Such fluctuations are, however, rare. Thus, the onset of phase separation gets delayed. This fact can be

appreciated from the first snapshot that contains clusters of very small sizes, despite the value of t being quite large. Following nucleation, rather fast growth of the disconnected clusters is clearly visible.

The presence of the circular symmetry, as seen in Fig. 3.2, in the structure of the clusters is related to the minimization of the interfacial free energy. The minor fluctuations that are noticeable in the boundary regions of these droplets are due to the proximity to the critical point that provides low surface tension and large equilibrium correlation length [2, 42].

In Fig. 3.3 we present a few evolution snapshots for a high overall density, viz., $\rho = 0.35$, the value of T remaining the same as in Fig. 3.2. The pattern in this case is contrastingly different from that in Fig. 3.2; the high density quench provides an elongated, interconnected morphology [4, 5, 14, 15]. The mechanisms of growth in the two cases are also expected to be different [9–13]. However, in the rest of the chapter we will focus only on the off-critical quench.

First, to check for the self-similar property [5] of the structures at different times, in Fig. 3.4 we show the scaling plot of the two-point equal time correlation function. Nice collapse of data from different times, when plotted vs the scaled distance r/ℓ, confirms that the patterns at different times differ from each other only by a change in length scale. Here we mention, for the bicontinuous structure (that we observed for $\rho = 0.35$), the correlation function exhibits prominent oscillation, albeit damped, around zero. This has connection with the fact that the integration of the $C(r, t)$ over space is related to the total system order-parameter [4,5], the latter being zero (in the language of ψ) for ρ close to ρ_c. Observation of only a very shallow minimum

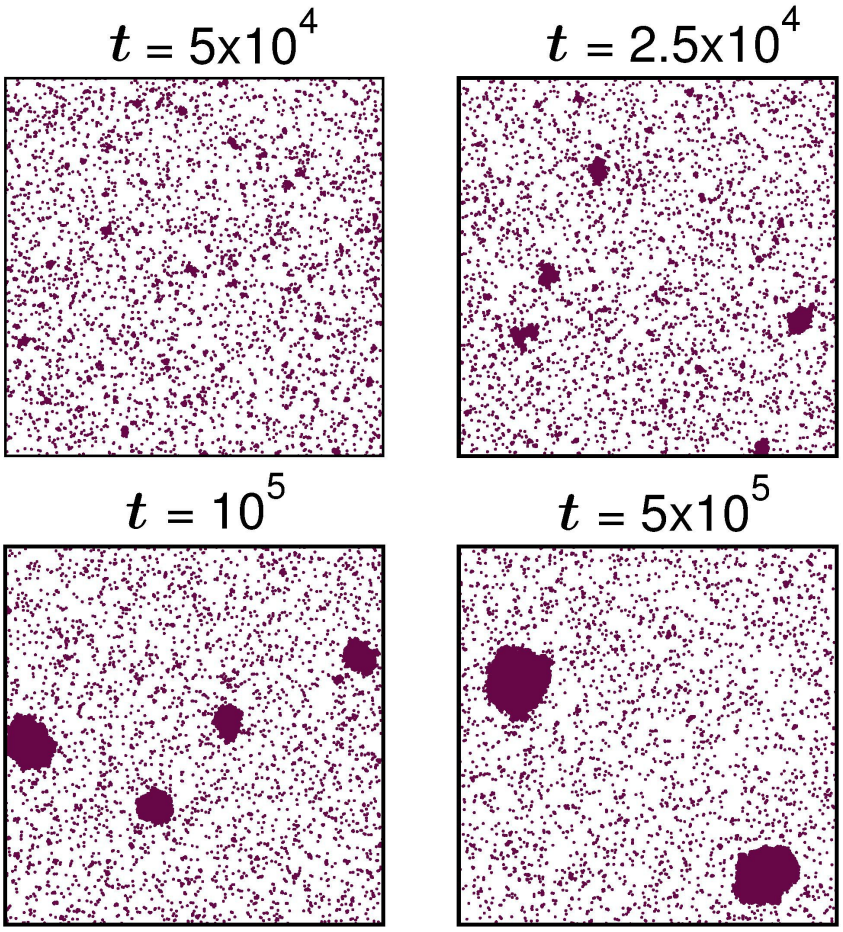

Figure 3.2: Snapshots during the evolution of the LJ fluid, having been quenched from a high temperature homogeneous state, with overall density $\rho = 0.03$, to a temperature $T = 0.35$, inside the coexistence curve. The dots mark the location of the particles. Though the results are obtained for $L = 2048$, we have shown only small parts (400×400) of the original system.

in the present case is due to the fact that, for $\rho << \rho_c$, the composition with respect to negative and positive values of ψ is highly asymmetric.

To understand the mechanism of growth, next we calculate the MSD [32] of the CMs of the droplets as

$$\text{MSD} = \left\langle \left(\vec{R}_{\text{CM}}(t') - \vec{R}_{\text{CM}}(0) \right)^2 \right\rangle, \tag{3.12}$$

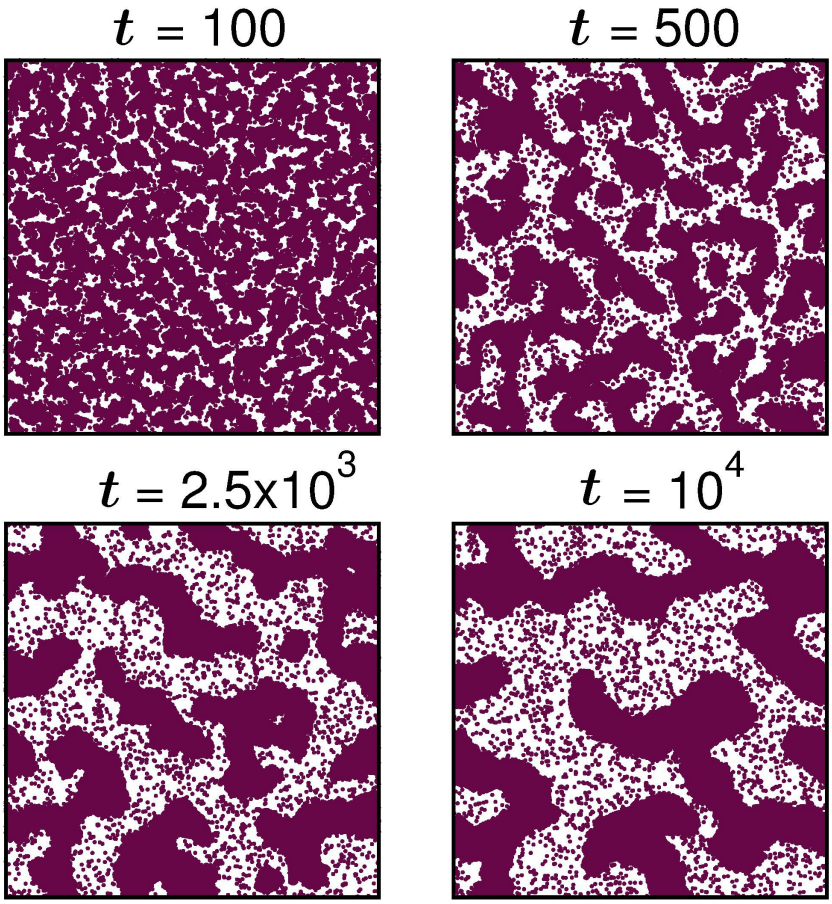

Figure 3.3: Same as Fig. 3.2 but for overall density $\rho = 0.35$. These results correspond to $L = 512$, unlike all the other results related to kinetics with NHT. Little higher density of the vapor phase that appears here, compared to that in Fig. 3.2, is because of the fact that in Fig. 3.2 we presented 400×400 cuts (from a larger system).

where $\vec{R}_{\rm CM}(t')$ is the location of a cluster CM at time t'. For this purpose, the droplets were appropriately identified by using the connectivity of regions with the positive values of ψ. The MSD for a typical CM is presented in the main frame of Fig. 3.5, as a function of time, on a log-log scale. Here t' is not the simulation time, it is measured from the moment a probe starts.

As mentioned above, the growth of the droplets during kinetics of phase

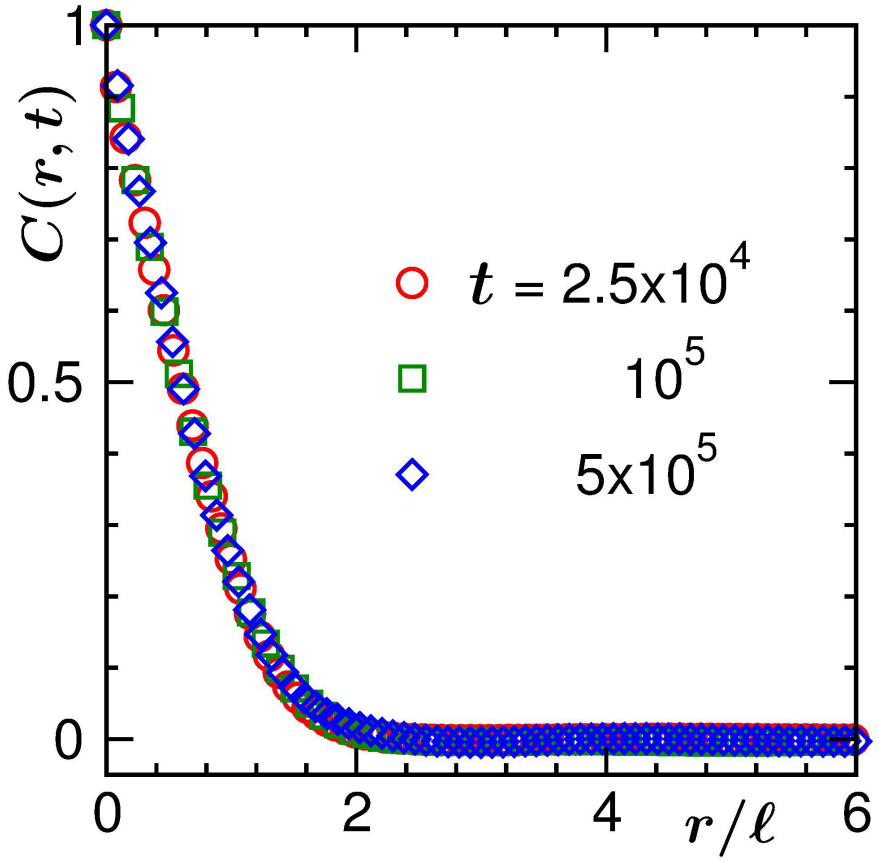

Figure 3.4: Scaling plot of the two-point equal time correlation function. Here we have plotted $C(r,t)$ as a function of the scaled distance r/ℓ, using data from three different times.

separation in solid binary mixtures occurs via the diffusion of particles from smaller droplets to larger ones, the CMs of the droplets remaining essentially fixed. However, as expected [9, 10, 14], Fig. 3.5 shows that the droplets can move in fluids. At early time, say upto $t' = 100$, the data are reasonably proportional to t'^2, implying ballistic motion [32]. After this time, the data gradually turn over to a linear behavior, that corresponds to diffusive motion [32]. Such a diffusive motion can be appreciated from the inset of this figure where we show a trajectory of the droplet under consideration.

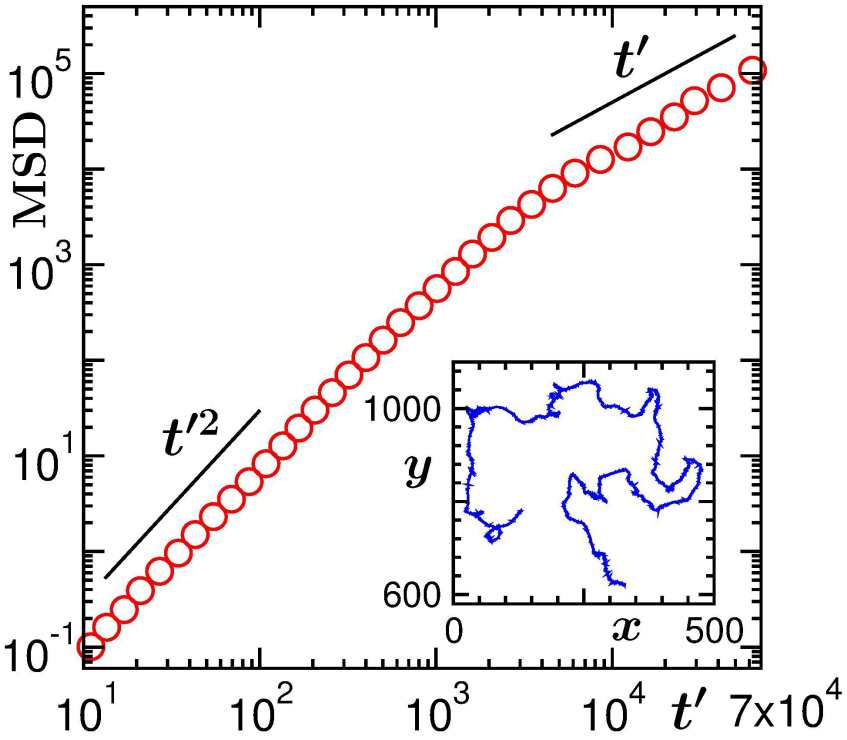

Figure 3.5: Mean-squared-displacement (MSD) for the center of mass of a typical liquid droplet is plotted vs time, on a log-log scale. The power-law regimes, parallel to t'^2 and t', correspond, respectively, to ballistic and diffusive motions. The inset shows the trajectory of the center of mass of the droplet over a period of time.

The mobility of the droplets will allow them to collide with each other. We have checked that such collisions are sticky in nature. Given that the droplets are in the liquid phase, mobility of the constituent particles, with respect to the CMs, is rather high. This fact allows a noncircular cluster, that has formed after a collision between two droplets, to gain circular shape, that is required to minimize the interfacial free energy, before it undergoes a collision. This explains the structural self-similarity, thus the scaling property of $C(r, t)$.

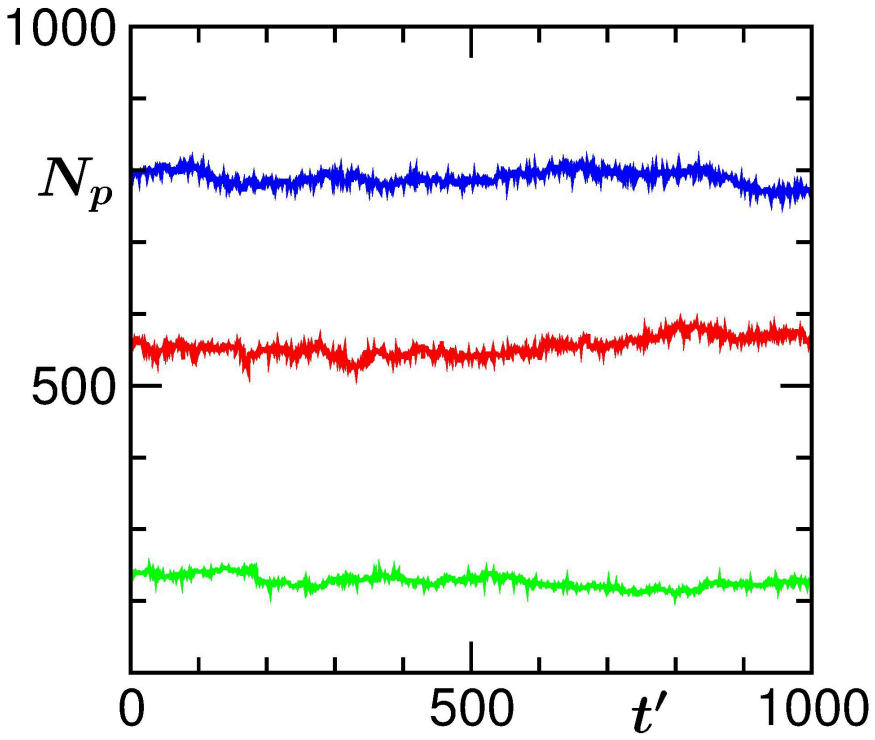

Figure 3.6: Plots of the numbers of particles in a few droplets, with the variation of time, the later being calculated from the beginning of the probes. During this period the droplets do not undergo collisions with any other droplet.

Despite growth via the diffusive motion of the droplets and sticky collisions among them, contribution to the growth due to the LS mechanism [8], i.e., via evaporation of particles from a smaller droplet and their condensation on a bigger one, is still possible. To check for that, in Fig. 3.6 we show the numbers of particles in a few droplets, over the time scale of typical collision interval. These plots convey the massage that the sizes of the droplets do not change between collisions. Thus, the growth essentially occurs via the diffusive droplet coalescence mechanism [9–11]. In that case, we expect a power-law growth with $\alpha = 0.5$.

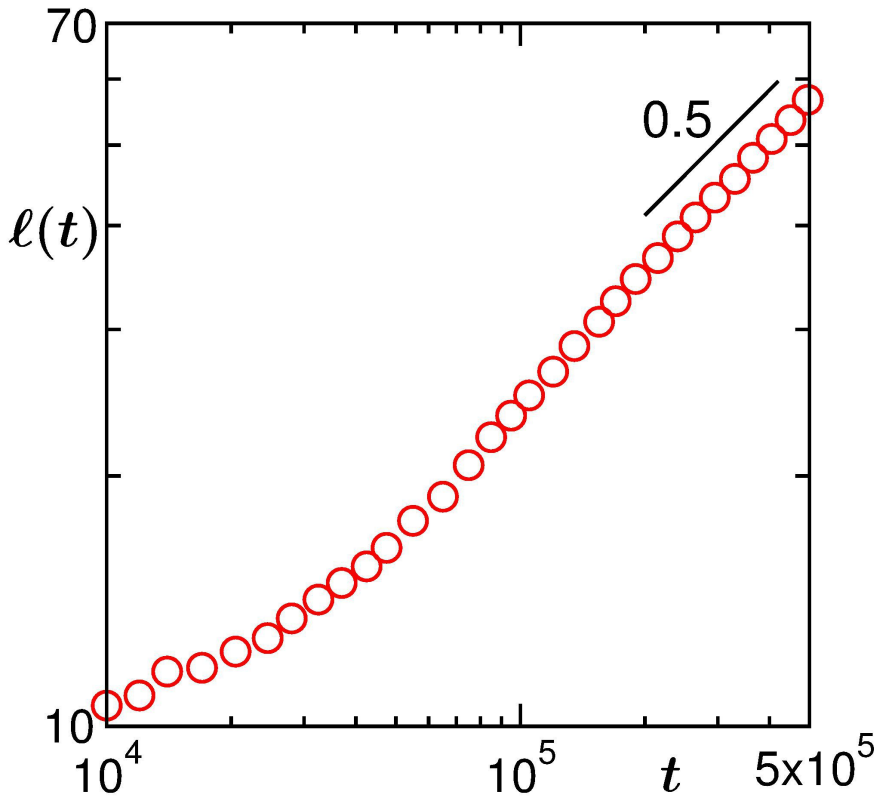

Figure 3.7: The average radius of the liquid droplets is plotted as a function of time, on a log-log scale. The solid line represents a power-law growth with exponent 0.5.

In Fig. 3.7 we show ℓ as a function of t, on a log-log scale. The late time data appear quite straight, implying power-law. The solid line there represents the BS growth-law with which the simulation data are very much consistent. Slightly faster trend in the simulation data, during an intermediate time regime, can be explained in the following way. Given that a perfect linear behavior in the MSD of cluster CMs appears at a rather late time, many collisions, particularly during the above mentioned regime, occur while the participating droplets are moving ballistically. This brings a shorter time scale in the problem during which the collision partners might not have

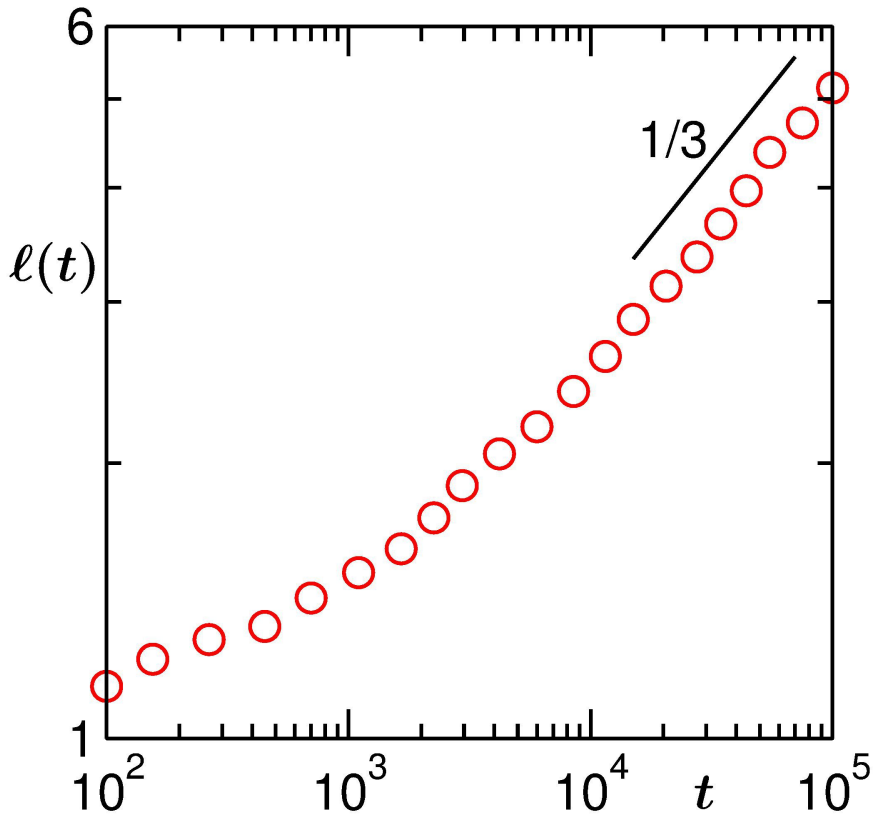

Figure 3.8: Same as Fig. 3.7, but the data set was obtained via the application of Andersen thermostat in our MD simulations. Unlike the previous results for kinetics (all of which were obtained using NHT), these results are presented after averaging over five independent initial configurations with $L = 512$.

gained a proper circular shape, from which they departed during the previous collisions. Presence of such non-circular shape or fractality (see the snapshot at $t = 2.5\times10^4$) during ballistic aggregation can enhance the growth rate [43]. On the other hand, the slower growth at very early time can be attributed to the LS mechanism [8]. During this period, the (unequilibrated) vapor phase density is rather high, leading to slow movement of the droplets. In that case growth can be dominated by evaporation-condensation mechanism, which is

also favored by rather low average distance between neighboring droplets. Nevertheless, we caution, the data from this early period should not be interpreted too seriously, for the reason stated above, i.e., the density inside the clusters is still changing, altering the value of ℓ even if the number of particles inside the droplets remain same. Such a time scale will be longer as one quenches the systems to temperatures closer to the critical value. This is due to the divergences of the correlation length and the relaxation time over that equilibrium length scale [2, 36, 42]. On the other hand, choice of temperature far below T_c does not allow us to study the kinetics of vapor-liquid transition, due to crystallization [43]. In the latter situation, the above mentioned fractality of the clusters become very prominent and growth may occur via the ballistic aggregation mechanism for the entire period due to very low density of the vapor phase [43]. In this case the self-similarity is also violated.

Finally, in Fig. 3.8 we show a plot of ℓ vs t from MD simulations using the Andersen thermostat (AT) [34]. The AT being a stochastic thermostat, it does not preserve hydrodynamics [32]. We have checked that for this method the droplets remain static. Thus, the only possibility of growth is via the LS mechanism. The consistency of the data set with the $t^{1/3}$ behavior, at late time, confirms this fact, alongside making sure that the BS mechanism is an hydrodynamic effect.

3.4 Summary

We have presented results related to the phase behavior and kinetics for the vapor-liquid transition in a two-dimensional Lennard-Jones model. While the phase diagram was obtained via the Monte Carlo simulations [36,37], for the kinetics we have performed molecular dynamics (MD) simulations [34] with hydrodynamics preserving thermostats. Even though MD simulations in the microcanonical ensemble preserves hydrodynamics perfectly, simulations in the canonical ensemble become essential to study the kinetics of phase separation, particularly for the transitions driven by temperature. This is due to the fact that with the increase of domain size, as the potential energy of the system decreases, simulations in the microcanonical set up will provide continuous increase in the kinetic energy, since the total energy is conserved in this ensemble [34, 36]. Thus, eventually the system temperature will go above the critical value, discarding the objective.

We have pointed out the structural difference between the high and the low density quenches. For the low density quench we have demonstrated the structural self-similarity, identified the growth mechanism and quantified the power-law growth exponent. We have shown that the growth essentially occurs due to the diffusive motion of the droplets and sticky collisions among them. The identified growth exponent matches well with the value predicted by Binder and Stauffer [9–11], for such a mechanism.

For the low temperature quenches with similar density we observe interesting disconnected fractal clusters, growth of which violate the "standard" self-similarity property discussed above [43]. Growth in this case occurs via

the ballistic aggregation mechanism, that provides an exponent much higher than the BS value [43].

Bibliography

[1] K. Binder, in *Phase Transformation of Materials*, ed. R.W. Cahn, P. Haasen and E.J. Kramer, VCH, Weinheim, 1991, Vol.5, p.405.

[2] A. Onuki, *Phase Transition Dynamics*, Cambridge University Press, UK, 2002.

[3] R.A.L Jones, *Soft Condensed Matter*, Oxford University Press, Oxford, 2008.

[4] S. Puri and V. Wadhawan (eds.), *Kinetics of Phase Transitions*, CRC Press, Boca Raton, 2009.

[5] A.J. Bray, Adv. Phys. **51**, 481 (2002).

[6] H. Tanaka, Phys. Rev. Lett. **72**, 1702 (1994).

[7] H. Tanaka, J. Chem. Phys. **105**, 10099 (1996).

[8] I.M. Lifshitz and V.V. Slyozov, J. Phys. Chem. Chem. Solids **19**, 35 (1961).

[9] K. Binder and D. Stauffer, Phys. Rev. Lett. **33**, 1006 (1974).

[10] K. Binder, Phys. Rev. B **15**, 4425 (1977).

[11] E.D. Siggia, Phys. Rev. A **20**, 595 (1979).

[12] H. Furukawa, Phys. Rev. A **31**, 1103 (1985).

[13] H. Furukawa, Phys. Rev. A **36**, 2288 (1987).

[14] S. Roy and S.K. Das, J. Chem. Phys. **139**, 044911 (2013).

[15] S. Majumder and S.K. Das, EPL **95**, 46002 (2011).

[16] R. Shimizu and H. Tanaka, Nature Communications **6**, 7407 (2015).

[17] C. Datt, S.P. Thampi and R. Govindarajan, Phys. Rev. E **16**, 303 (2015).

[18] S. Roy and S.K. Das, Phys. Rev. E **85**, 050602 (2012).

[19] S. Roy and S.K. Das, Soft Matter **9**, 4178 (2013).

[20] S.K. Das, S. Roy and J. Midya, C. R. Phys. **16**, 303 (2015).

[21] S. Majumder and S.K. Das, Phys. Chem. Chem. Phys. **15**, 13209 (2013).

[22] J. Jung, J. Lee, and J.S. Kim, Chem. Phys. **449**, 1 (2015).

[23] J. Jung, E. Jang, M.A. Shoib, K. Jo, and J.S. Kim, J. Chem. Phys. **144**, 134502 (2016).

[24] S. Razavi, J. Koplik, and I. Kretzschmar, Langmuir, **30**, 11272 (2014).

[25] P.B. Warren, Phys. Rev. Lett. **87**, 225702 (2001).

[26] F. Perrot, P. Guenoun, T. Baumberger, D. Beysens, Y. Garrabos, and B. Le Neindre, Phys. Rev. Lett. **73**, 688 (1994).

[27] A.C. Zettlemoyer (ed.), *Nucleation*, Dekker, New York, 1969.

[28] F.F. Abraham, *Homogeneous Nucleation Theory*, Academic, New York, 1974.

[29] K. Binder, Rep. Prog. Phys. **50**, 783 (1987).

[30] S. Twomey, J. Phys. Chem. **84**, 1459 (1980).

[31] E. Ilotoviz and A. Khaln, Atmos. Chem. Phys., doi:10.5194/acp-2016-499.

[32] J.-P. Hansen and I.R. McDonald, *Theory of Simple Liquids*, Academic Press, London, 2008.

[33] T.M. Squires and J.F. Brady, Phys. Fluids **17**, 073101 (2005).

[34] D. Frenkel and B. Smit, *Understanding Molecular Simulations: From Algorithm to Applications*, Academic Press, San Diego, 2002.

[35] M.P. Allen and D.J. Tildesley, *Computer Simulations of Liquids*, Clarendon, Oxford, 1987.

[36] D.P. Landau and K. Binder, *A Guide to Monte Carlo Simulations in Statistical Physics* (Cambridge University Press, Cambridge, 2009).

[37] A.Z. Panagiotopoulos, Molec. Phys. **61**, 813 (1987).

[38] E.A. Koopman and C.P. Lowe, J. Chem. Phys. **124**, 204103 (2006).

[39] S.D. Stoyanov and R.D. Groot, J. Chem. Phys. **122**, 114112 (2005).

[40] T. Soddemann, B. Dünweg, and K. Kremer, Phys. Rev. E **68**, 046702 (2003).

[41] S. Nosé, Progr. Theor. Phys. **103**, 1 (1991).

[42] V. Privman, P.C. Hohenberg, and A. Aharony, in *Phase Transitions and Critical Phenomena*, edited by C. Domb and J.L. Lebowitz (Academic Press, New York, 1991), Vol. 14, Chap. I.

[43] J. Midya and S.K. Das, arXiv:1604.06227.

Chapter 4

Cluster growth during vapor-solid transition in a 2D Lennard-Jones system

4.1 Introduction

Universality in dynamics of phase transitions is not as robust as statics [1]. E.g. each of solid-solid [2–8], fluid-fluid [3, 5, 9–25] and solid-fluid [23, 26, 27] transitions may have different relaxation mechanism. In kinetics, the average size (ℓ) of domains, rich in one or the other type of particles, grows with time (t) as [3] $\sim t^{\alpha}$. Growth in solid mixtures [6] occurs via particle diffusion, providing $\alpha = 1/3$. In fluids [1, 3], hydrodynamics is important and the related mechanism depends upon the region of quench inside the miscibility gap [3,9–15,17–21]. For disconnected spherical clusters, close to a coexistence curve, the fluid-fluid phase separations proceed via the cluster diffusion and

coalescence mechanism [9–11], for which $\alpha = 1/d$ in space dimension d. In the fluid-solid case, interplay between hydrodynamic and particle-diffusion mechanisms can provide new picture. Despite diverse relevance [26–31], other than condensed matter physics, understanding in this variety remains poor, due to difficulties with the identification of phases and slow nucleation.

Despite weak universality, self-similarity [3, 9] is a robust phenomenon exhibited by structures during phase transitions. E.g. the above mentioned spherical clusters retain their shape at all times. As a consequence, in usual scenario, the two-point equal-time correlation function [3] $C(r = |\vec{r}|, t)$ $(=< \psi(\vec{0}, t)\psi(\vec{r}, t) > - < \psi(\vec{r}, t) >^2$, ψ being a time and space ($\vec{r}$) dependent order-parameter), obeys the scaling property [3, 9] $C(r, t) \equiv C(r/\ell(t))$, meaning, structures at two times differ only by size. Though found to hold [7–9, 18, 19, 21, 32] in diverse situations, validity of this scaling remains unknown for the fluid-solid case. A crucial general question in this context is related to the consequence on growth if this "simple" scaling is absent.

Here we study vapor-solid transitions in a Lennard-Jones (LJ) model via hydrodynamics preserving molecular dynamics (MD) simulations. While the results are expected to have general validity, here we focus on $d = 2$, relevant in contexts like active matter [33, 34] and bio-membranes [26]. Strikingly, for quenches with low overall density, the above scaling property in $C(r, t)$ is absent due to the formation of disconnected fractal solid domains, which, in turn, have significant influence on the kinetics. The fractal structure forms due to the existence of two well-separated time scales in the problem that do not allow the interfacial energy to minimize. One time scale comes from the slow particle mobility inside the rigid solid clusters and the other

from the fast ballistic-like transport of the clusters through the low density vapor phase. Sticky collisions among such ballistically moving fractal objects, having strong experimental relevance in the contexts of clustering in a cosmic soup [28–31, 35] and various aerosols (including growth of ice crystals in clouds [36]), lead to a new growth picture that has been understood via a nonequilibrium kinetic theory [28, 31, 37].

4.2 Model and Methods

For the kinetics, we perform MD simulations using a model [8, 18, 38] where particles, at r distance apart, interact via $U(r) = u(r) - u(r_c) - (r - r_c)(du/dr)_{r=r_c}$, $u(r)$ being the standard LJ form [38] $u(r) = 4\varepsilon[(\sigma/r)^{12} - (\sigma/r)^6)]$. Here, ε has the dimension of energy, σ is the interatomic diameter, and r_c ($= 2.5\sigma$) is a cut-off distance. In $d = 2$, the vapor-liquid phase diagram for this model was estimated by us via the Monte Carlo [39] simulations in a Gibbs ensemble, the critical values of T and number density (ρ) being respectively $T_c = (0.415 \pm 0.005)\epsilon/k_B$ and $\rho_c = 0.350 \pm 0.005$, k_B being the Boltzmann constant. Fixing ρ to 0.03, we explore very low T, to access the vapor-solid coexistence with disconnected morphology. Unless otherwise mentioned, our results are for $T = 0.25\epsilon/k_B$. The MD simulations were performed in canonical ensemble, with the Lowe-Andersen [40], dissipative particle dynamics [41] and the Nosé-Hoover thermostats [42, 43] (NHT), which preserve hydrodynamics. We, however, have presented results only from the NHT that appears to us a better temperature controller. We note that, even though the thermodynamic properties are independent of

the choice of a thermostat, the kinetics is very sensitive to it. To study kinetics in connection with fluids, conservation of local momentum and other hydrodynamic properties is necessary, which is not possible with stochastic thermostats. All our simulations were performed in periodic square boxes of linear dimension $L = 2048\sigma$. The quantitative results are presented after averaging over a minimum of 10 initial configurations. The time in our MD simulations was measured in units of $(m\sigma^2/\varepsilon)^{1/2}$, m being the the mass of a particle. For all presentation purposes we set m, σ and ε to unity. For the calculation of $C(r)$ we have mapped our system [18, 19, 21] onto a binary one by assigning the values ± 1 to ψ depending upon whether the local density is higher or lower than the critical value.

4.3 Results

Figure 4.1 shows three evolution snapshots. Following nucleation, at initial stage the circular clusters are in liquid phase. These liquid drops grow due to the deposition of individual particles on them as well as via the mechanism consisting of droplet diffusion and coalescence [9]. Gradually, crystallization inside the droplets occurs and density in the vapor regions saturates to a very low value. The solid clusters move rapidly through the low density background phase, to provide fast ballistic-like aggregation that leads to the fractal structure, as seen in the later time snapshots. We will provide details in support of this latter mechanism. With a stochastic (Andersen) thermostat [43] we obtain circular pattern at all times. This already states that the fractality is a result of hydrodynamics.

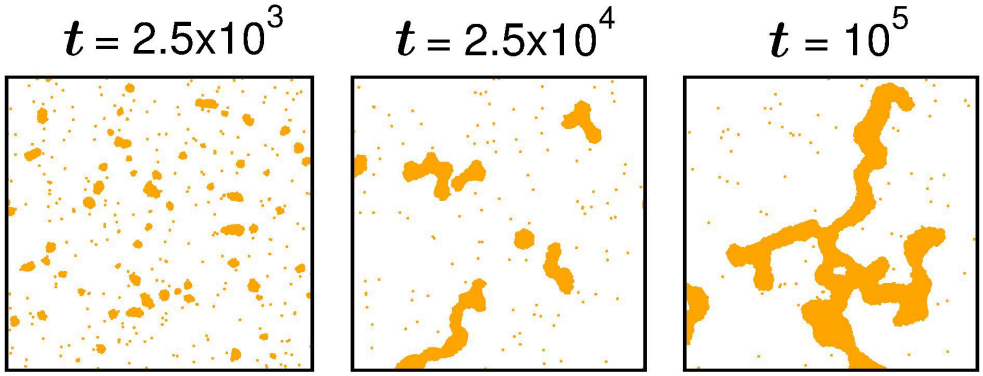

Figure 4.1: Snapshots during the evolution of the Lennard-Jones system, having been quenched from a high temperature homogeneous state to the state point ($\rho = 0.03, T = 0.25$) inside (and close to the vapor branch of) the coexistence curve. Only 400×400 parts of the original systems ($L = 2048$) are shown from three different times. Because of this reason, the last snapshot appears like an interconnected structure in spinodal decomposition.

In Fig. 4.2 we show the ℓ vs t plot. This quantity was calculated via a standard method [8, 18, 19, 21] followed in phase ordering dynamics (see caption). In fluid-fluid phase separation, for disconnected droplet morphology and growth via droplet-diffusion and coalescence mechanism, one writes [9–11]

$$\frac{dn}{dt} = -Bn^2, \tag{4.1}$$

where B ($= D\ell$, D being a diffusivity) is a positive constant, decided by the Stokes-Einstein-Sutherland relation [44], and n is the droplet density. Solution of equation (4.1), taking $n \propto 1/\ell^d$, provides $\alpha = 1/d$. But the late time data appear consistent with $\alpha = 1/3$ which points towards the particle-diffusion mechanism in solid mixtures [1–6]. However, as seen in Fig. 4.3, the number of particles in a droplet, before it undergoes a collision, remains

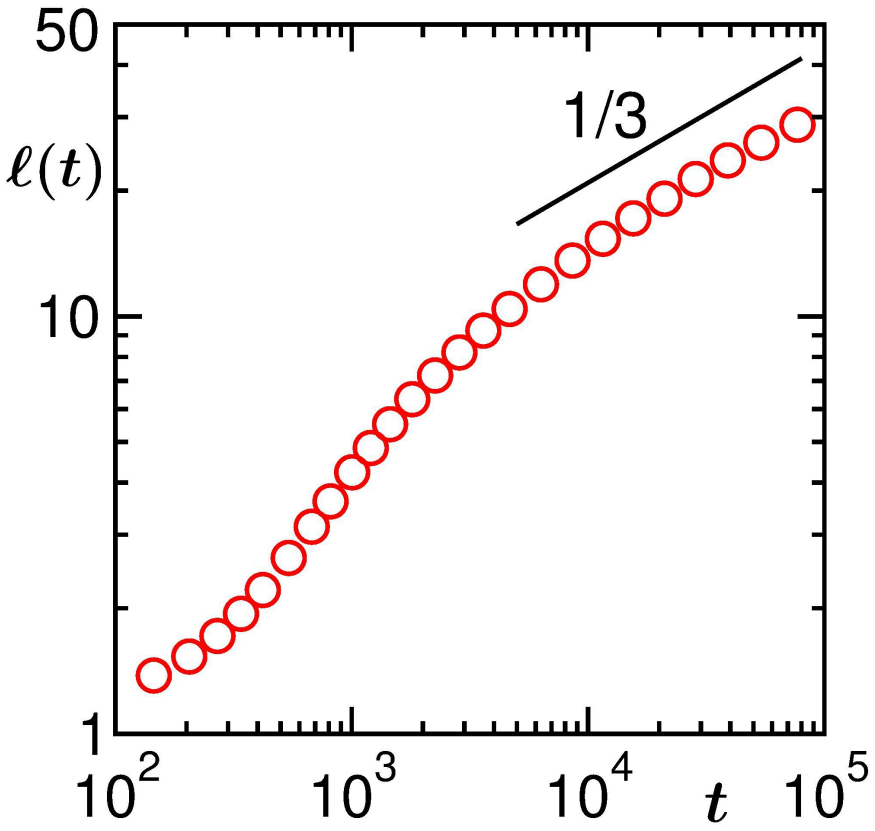

Figure 4.2: Average domain size, $\ell(t)$, obtained from the the length distribution $P(\ell_d, t)$ as $\ell(t) = \int P(\ell_d, t)\ \ell_d\ d\ell_d$, a standard method [8, 18, 19, 21] followed in phase ordering dynamics, ℓ_d being the distance between two successive interfaces along any direction, is plotted vs t, on log-log scale. The solid line corresponds to $t^{1/3}$ behavior.

constant. Thus, the growth occurs via collisions. The consistency of the data with $\alpha = 1/3$ is thus accidental. In fact a closer look suggests continuous bending in the data set.

As seen in Fig. 4.4, there exists severe lack of scaling [45] in the $C(r, t)$ which may in general be due to a disproportionate growth in the structure. E.g. in a fractal morphology the branches may have a different widening rate compared to the rate of increase in the overall length [46]. In the present

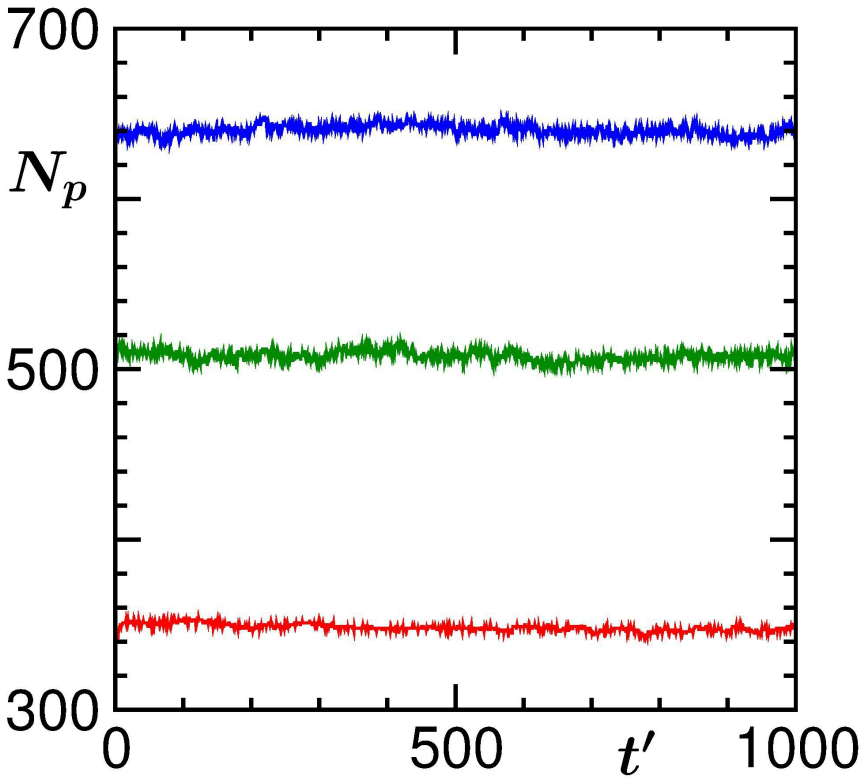

Figure 4.3: Plots of number of particles, N_p, vs translated time, for three different droplets.

case this can be due to two time scales, coming from different transport mechanisms. While the overall growth occurs due to motion of the clusters and collisions among them, the structural change of the clusters, following the collisions, is related to the dynamics of the constituent particles. The mobility of these particles, in their cluster reference frame, can be low, depending upon the phase of the clusters which will be addressed later. In such cases, scaling property of $C(r,t)$ involves the fractal dimensionality and extraction of a characteristic length via the standard procedure (mentioned above - see caption of Fig. 4.2) is not meaningful. An alternative is to look for the growth of the average mass (M), appropriate [47] for non-percolating

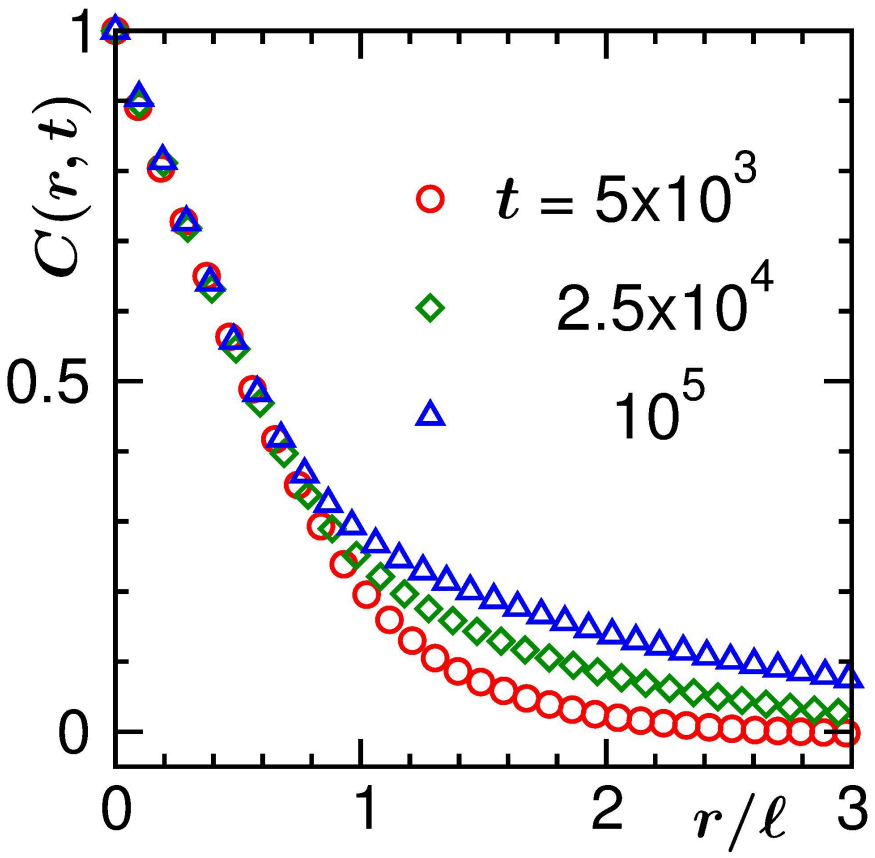

Figure 4.4: Two point equal time correlation functions from three different times are plotted vs r/ℓ.

structures as in the present case, and connect it to the average radius of gyration [34, 48] (R_g). The latter is the true characteristic length scale, and is different from ℓ for the present problem.

In Fig. 4.5 we present a plot of M vs R_g. This shows a power-law behavior

$$M \sim R_g^{d_f}. \tag{4.2}$$

The data appear consistent with $d_f = 1.6$, the fractal or mass dimensionality [48] of the structure. The dimensionality is low, even compared to the

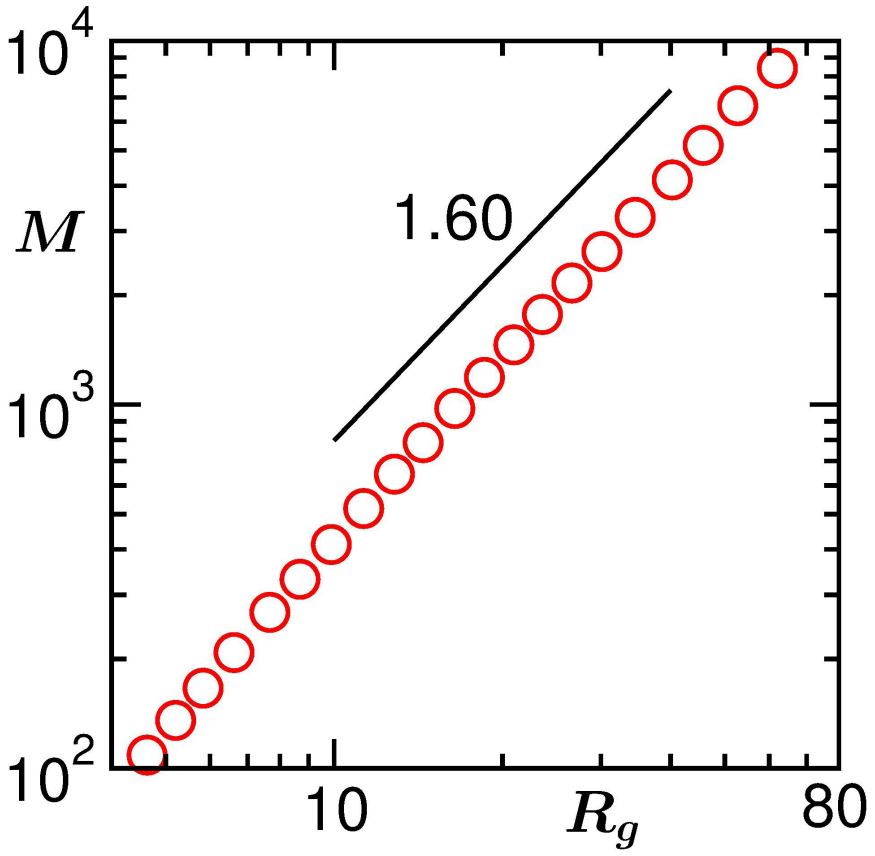

Figure 4.5: Log-log plot of average (time dependent) cluster mass (M) vs the average radius of gyration (R_g). The solid line is a power-law with exponent $d_f = 1.6$.

structures formed in diffusion limited aggregation [49]. This we will explain later. To apply equation (4.1), we need to know about the nature of motion of these fractal objects. Note that despite the dominant mechanism being collision, if the droplet motion is not diffusive and the structure is not circular, B need not be a constant. In Fig. 4.6, we show the mean-squared-displacement (MSD) [44] ($= \langle |\vec{R}_{\rm CM}(t) - \vec{R}_{\rm CM}(0)|^2 \rangle$) for the center of mass (CM) of a cluster ($\vec{R}_{\rm CM}$ being the position vector for the CM), vs time. The robust t^2 behavior over long time confirms that the motion is practically

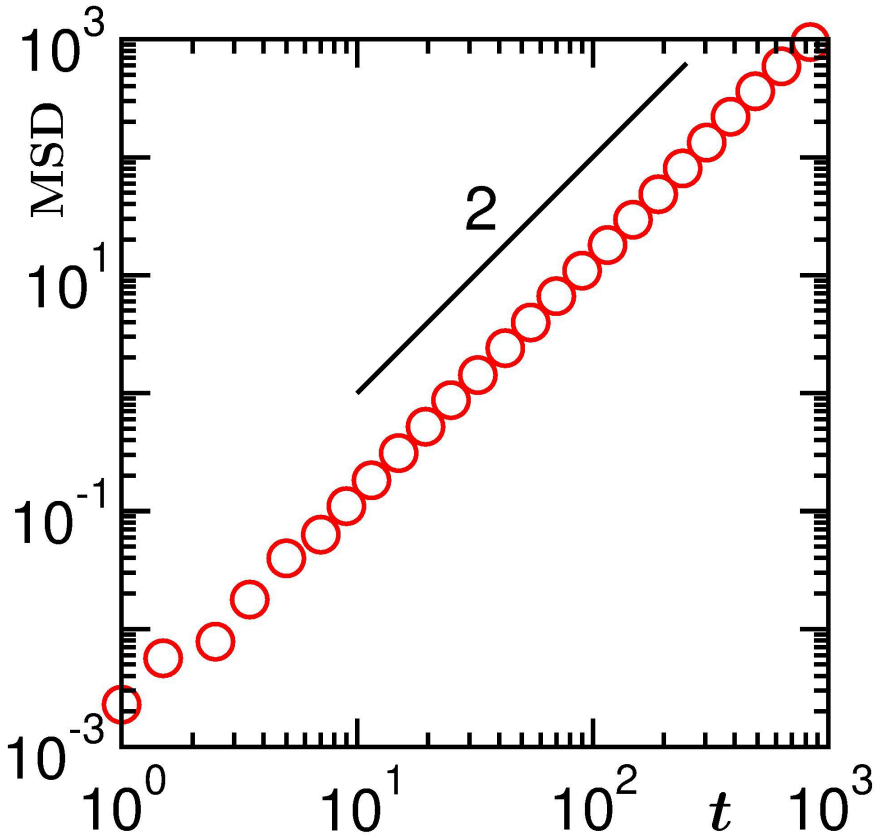

Figure 4.6: Mean-squared-displacement of a typical cluster is plotted, on a log-log scale, vs t. The t^2 line corresponds to ballistic motion.

ballistic. Such a transport is due to the low viscosity of the vapor phase and can be understood from the perspective of hydrodynamic theory [44] with the following input. Given that the density is uniform in the vapor phase and Reynolds number is very high, the terms related to pressure gradient, diffusion and advection will be absent in the Navier-Stokes equation. These ballistically moving clusters grow due to sticky collisions among them, because of strong attraction among particles in the peripheral regions of the colliding clusters. In a stochastic thermostat, in every step, the particles are

provided with random velocities. This will prevent coherency in particle motion, necessary in getting such ballistic cluster motion. In that case cluster growth will occur via evaporation-condensation mechanism of Lifshitz and Slyozov [2, 3], applicable for kinetics of phase separation in solid mixtures. The findings from Figs. 4.5 and 4.6 necessitate the call for the theory of

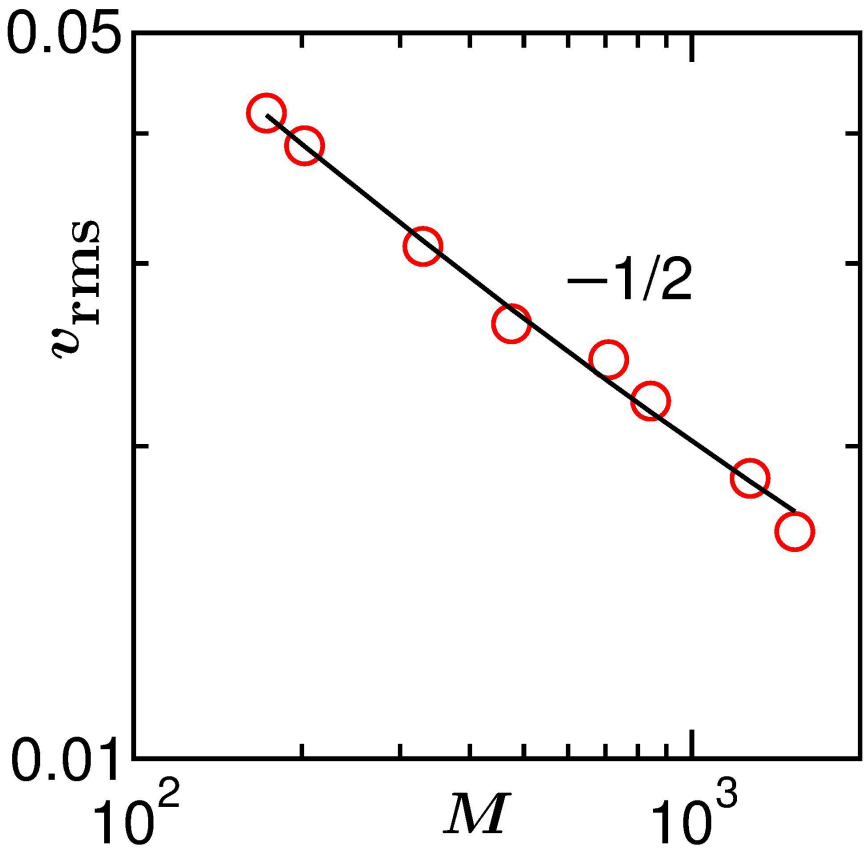

Figure 4.7: Root-mean-squared velocity, $v_{\rm rms}$, of the clusters is plotted, on log-log scale, vs M. The solid line has a power-law decay with exponent 1/2.

ballistic aggregation, having the equation [28, 37]

$$\frac{dn}{dt} = -\text{“collision-cross-section”} \times < v_{\rm rel} > \times n^2. \qquad (4.3)$$

A continuum hydrodynamic theory is not needed for the understanding, since the events of interest are collisions among clusters with large average distance of separation. This is different from the case of high T quenches close to the critical density, for which one obtains percolating liquid-domain morphology, requiring a continuum hydrodynamic description with the above mentioned terms in the Navier-Stokes equation.

The current problem has some similarity [28, 35] with the clustering in a system of sticky hard spheres (SHS). The difference between the SHS case [28, 35] and the problem addressed in this chapter is that the former is not a phase transition, particles there are non-interacting, surface tension is absent and fractality is naturally expected due to sticky collisions. Nevertheless, in the case of SHS, fractality of the structure was not considered, neither in theory nor in simulation, which we explicitly include here. Thus, the current study, even though designed for phase transitions, provides better description of experimentally observed clustering phenomena in diverse fields quite naturally.

In $d = 2$, the "collision-cross-section" is a "length", equaling R_g. For uncorrelated motion of the droplets [28], the mean relative velocity, $< v_{\rm rel} >$, of the clusters should be the root-mean-squared velocity, $v_{\rm rms}$, which, as seen in Fig. 4.7, varies with M as

$$v_{\rm rms} \sim M^{-1/2}, \tag{4.4}$$

expected for Maxwellian distribution of kinetic energy, validity of which is separately checked. Incorporating these facts in equation (4.3), along with

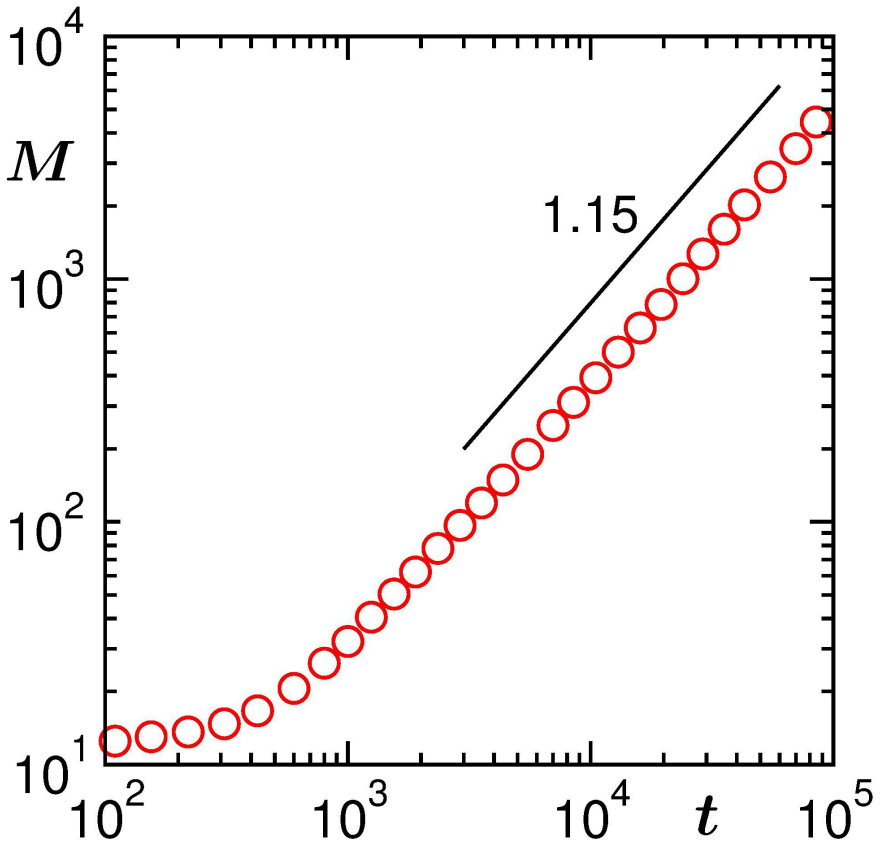

Figure 4.8: Log-log plot of M vs t. The solid line corresponds to a power-law growth with the exponent 1.15. This number is stable against system sizes.

$n \propto 1/M$, we obtain

$$\frac{dM}{dt} \sim M^{\frac{2-d_f}{2d_f}}, \tag{4.5}$$

providing

$$M \sim t^{\beta_0}; \quad \beta_0 = \frac{2d_f}{3d_f - 2}. \tag{4.6}$$

The value of the exponent β_0 for $d_f = 1.6$ is approximately 1.143. In Fig. 4.8 we show a plot of M, vs t. In the long time regime, the data exhibit a power-law behavior. The exponent is very much consistent with the predicted value.

This implies

$$R_g \sim t^{0.72}, \tag{4.7}$$

the exponent being rather high for a $2D$ phase separation. Given the clean nature of the data we do not aim for a finite-size scaling analysis [20,39,50]. In Fig. 4.9 we show the growth exponent β_0 vs temperature. These are in nice agreement with the values obtained from Eq. (4.6). Note that with the change of T, the rigidity of the cluster changes, providing different values of d_f.

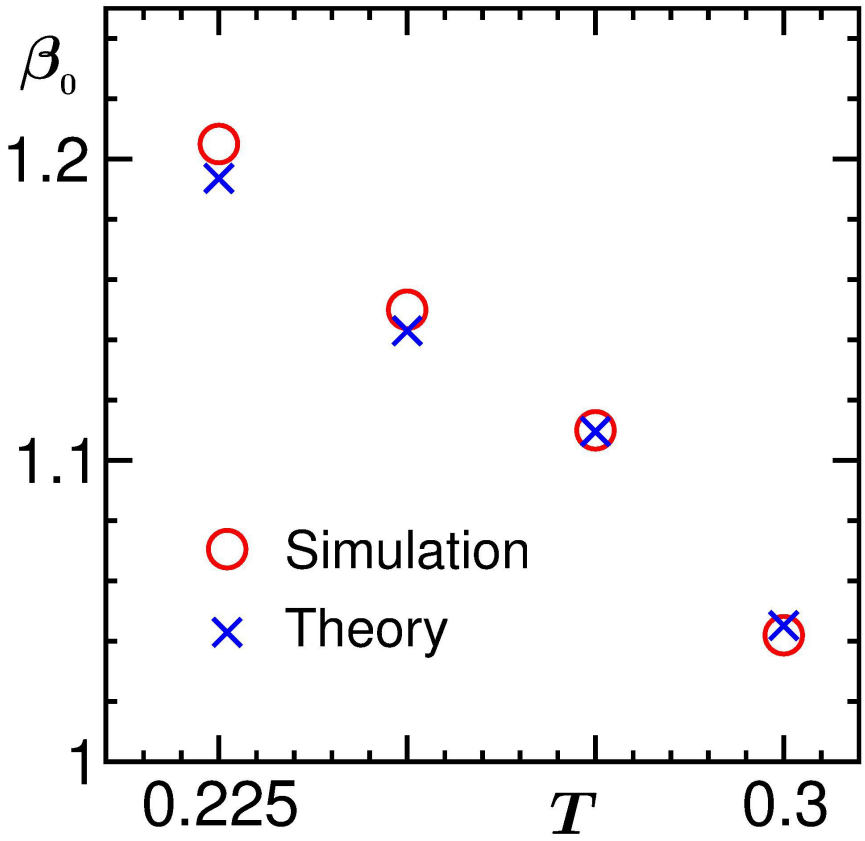

Figure 4.9: Plot of the exponent β_0 as a function of temperature.

On the question of another (slower) time scale being the origin of fractality, we intend to show the existence of a rigid crystalline order. In Fig. 4.10(a) we show the snapshot of a part of a cluster and in Fig. 4.10(b) the corresponding structure factor [44], $S(k)$, vs the wave number k. These clearly confirm the presence of a crystalline order. Nevertheless, because of only quasi-long-range order [51] (in $d = 2$) in a soft background and the possibility that frequent particle exchanges between the solid and the vapor phases can take place in the interfacial regions, one should examine the rigidity to validate the solid state transport properties. In Fig. 4.10(c), we show trajectories of three particles, belonging to the same cluster, with respect to the cluster CM. All the scalar distances remain constant. The circular shape of the trajectories confirm rotation of the cluster. Such rotations make the collisions more probable in the peripheral regions, perpendicular to the major cluster-axes. This explains the very low value for the fractal dimension. In Fig. 4.10(d), we show the x-component of the intermediate trajectory, vs time. It appears, the typical time period of rotations is comparable to the time scale of the collisions. This also confirms the rigidity of the clusters over a long time. Thus, the origin of the fractal domain structure lies in the rigid crystalline order. The constituent particles of a non-circular cluster cannot rearrange themselves to provide the latter a circular shape before it undergoes a collision.

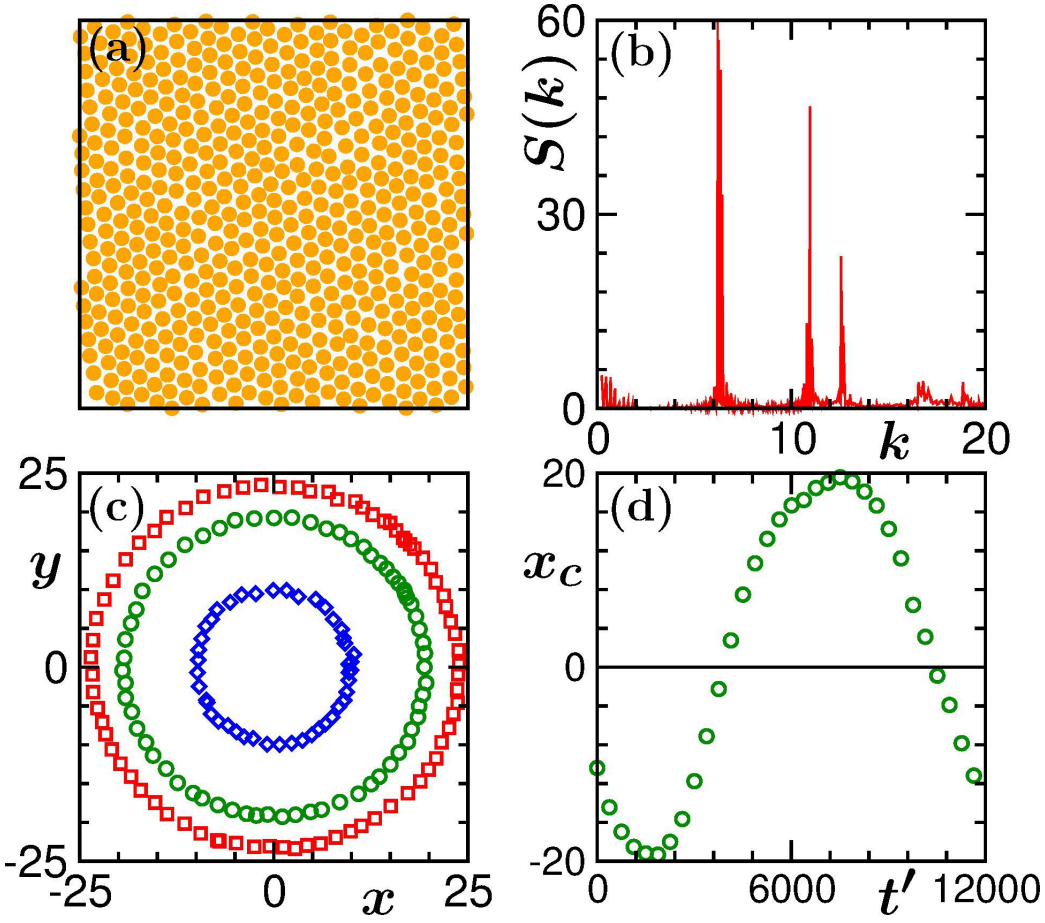

Figure 4.10: (a) Snapshot of a part of a cluster at $t = 10^5$. (b) The structure factor $S(k)$ $(=< \sum_{i=1,j=1}^{N} \exp(i\vec{k} \cdot \vec{r}) > /N$; $\vec{r} = \vec{r}_i - \vec{r}_j$, N being the number of particles in the considered cluster), for the snapshot in (a), is plotted vs the wave number k. (c) Relative positions of three particles with respect to the center of mass of a cluster to which these particles belong. (d) Plot of x-component for the intermediate circle in (c), vs translated time.

4.4 Summary

In conclusion, for overall density close to the vapor branch, the vapor-solid transition proceeds unusually fast, via the ballistic aggregation mechanism [28]. In kinetics of phase transition, two mechanisms are known for

disconnected cluster growth, viz., Lifshitz-Slyozov particle diffusion mechanism and Binder-Stauffer droplet diffusion and coalescence mechanism. In this work we have demonstrated that ballistic aggregation is another mechanism if the background density is very low. The standard self-similarity, usually observed in phase transitions, is violated during the growth process, due to the formation of filament-like fractal pattern. Invoking the fractality, along with the mass dependence of the mean relative velocity of the clusters, in a general formalism [28], we have obtained the growth law, exponent of which depends strongly upon fractality, thus the temperature, as observed in simulations. The identified mechanism has similarity with that for the formation of clusters in cosmic dust [28] and in coarsening in active matters [34] where the particles in a domain move coherently, in addition to other condensed matter systems. The fractality observed by us is common in many physical situations, where solid clusters are of varying shapes, e.g. needles, dendrite, etc. [36], with dimensionality much smaller than that of the system. Thus our results are relevant for true physical phenomena, e.g. growth of ice crystals in cloud via collisions [36].

Bibliography

[1] A. Onuki, *Phase Transition Dynamics*, Cambridge University Press, UK, 2002.

[2] K. Binder, in *Phase Transformation of Materials*, ed. R.W. Cahn, P. Hansen and E.J. Kramer, VCH, Weinheim, 1991, Vol.5, p.405.

[3] A.J. Bray, Adv. Phys. **51**, 481 (2002).

[4] R.A.L Jones, *Soft Condensed Matter*, Oxford University Press, Oxford, 2008.

[5] S. Puri and V. Wadhawan (eds.), *Kinetics of Phase Transitions*, CRC Press, Boca Raton, 2009.

[6] I.M. Lifshitz and V.V. Slyozov, J. Phys. Chem. Chem. Solids **19**, 35 (1961).

[7] S. Puri and K. Binder, Phys. Rev. Lett. **86** 1797 (2001).

[8] S. Majumder and S.K. Das, Phys. Rev. E **81**, 050102 (2010).

[9] K. Binder and D. Stauffer, Phys. Rev. Lett. **33**, 1006 (1974).

[10] K. Binder, Phys. Rev. B **15**, 4425 (1977).

[11] E.D. Siggia, Phys. Rev. A **20**, 595 (1979).

[12] H. Furukawa, Phys. Rev. A **31**, 1103 (1985).

[13] H. Furukawa, Phys. Rev. A **36**, 2288 (1987).

[14] H. Tanaka, Phys. Rev. Lett. **72**, 1702 (1994).

[15] H. Tanaka, J. Chem. Phys. **105**, 10099 (1996).

[16] H. Kabrede and R. Hentschke, Physica A **361**, 485 (2006).

[17] S. Majumder and S.K. Das, EPL **95**, 46002 (2011).

[18] S. Roy and S.K. Das, Phys. Rev. E **85**, 050602 (2012).

[19] S. Roy and S.K. Das, Soft Matter **9**, 4178 (2013).

[20] S. Majumder and S.K. Das, Phys. Rev. Lett. **111**, 055503 (2013).

[21] S. Roy and S.K. Das, J. Chem. Phys. **139**, 044911 (2013).

[22] K. Binder and M.H. Kalos, J. Stat. Phys. **22**, 363 (1980).

[23] G. Leptoukh, B. Strickland and C. Ronald, Phys. Rev. Lett. **74**, 3636 (1995).

[24] R. Shimizu and H. Tanaka, Nature Communications **6**, 7407 (2015).

[25] F. Perrot, P. Guenoun, T. Baumberger and D. Beysens, Phys. Rev. Lett. **73**, 688 (1994).

[26] M. Sleutel, J. Lutsko, A.E.S. Van Driessche, M.A. Duŕan-Olivencia and D. Maes, Nature Communications **5**, 5598 (2014).

[27] Y. Suzuki, M. Endo and H. Sugiyama, Nature Communications **6**, 8052 (2015).

[28] G.F. Carnevale, Y. Pomeau and W.R. Young, Phys. Rev. Lett. **64**, 2913 (1990).

[29] G. Wetherill, *The Formation and Evolution of Planetary Systems*, Cambridge University Press,Cambridge, 1988.

[30] S. Chandrasekhar, Rev. Mod. Phys. **15**, 1 (1943).

[31] M.H. Ernst, in *Fundamental Problems in Statistical Mechanics VI*, E.G.D. Cohen (ed.), Elsevier, New York, 1985.

[32] S.K. Das, S. Puri, J. Horbach and K. Binder, Phys. Rev. Lett. **96**, 016107 (2006).

[33] R. Wittkowski, A. Tiribocchi, J. Stenhammer, R.J. Allen, D. Marenduzzo and M.E. Cates, Nature Communications **5**, 4351 (2014).

[34] P. Cremer and H. Löwen, Phys. Rev. E **89** 022307 (2014).

[35] E. Trizac and J.-P. Hansen, J. Stat. Phys. **82** 1345 (1996).

[36] R.R. Rogers and M.K. Yao, *A Short Course in Cloud Physics*, Butterworth Heinemann, 3rd Edition (1989).

[37] S.N. Pathak, D. Das and R. Rajesh, EPL **107**, 44001 (2014).

[38] M.P. Allen and D.J. Tildesley, *Computer Simulations of Liquids*, Clarendon, Oxford, 1987.

[39] D.P. Landau and K. Binder, *A Guide to Monte Carlo Simulations in Statistical Physics*, Cambridge University Press,Cambridge, 2009.

[40] E.A. Koopman and C.P. Lowe, J. Chem. Phys. **124**, 204103 (2006).

[41] S.D. Stoyanov and R.D. Groot, J. Chem. Phys. **122**, 114112 (2005).

[42] S. Nosé, J. Chem. Phys. **81**, 511 (1984).

[43] D. Frenkel and B. Smit, *Understanding Molecular Simulations: From Algorithm to Applications*, Academic Press, San Diego, 2002.

[44] J.-P. Hansen and I.R. McDonald, *Theory of Simple Liquids*, Academic Press, London, 2008.

[45] S.K. Das, S. Puri and M.C. Cross, Phys. Rev. E **64**, 46206 (2001).

[46] R.L. Jack, M.F. Hagan and D. Chandler, Phys. Rev. E **76**, 021119 (2007).

[47] S. Paul and S.K. Das, EPL **108**, 66001 (2014).

[48] T. Vicsek, M. Shlesinger and Matsnshita (eds.) *Fractals in Natureal Sciences*, World Scientific, Singapore, 1994.

[49] T.A. Witten Jr. and L.M. Sander, Phys. Rev. Lett. **47**, 1400 (1981).

[50] M.E. Fisher and Michael N. Barber, Phys. Rev. Lett. **28** 1516 (1972).

[51] N. Goldenfeld, *Lectures on Phase Transitions and the Renormalization Group*, Addison-Wesley, 1992.

Chapter 5

Aging in ferromagnetic ordering: Full decay and finite-size scaling of autocorrelation

5.1 Introduction

Understanding of the decay of two-time $(t, t_w; t > t_w)$ correlations

$$C(t, t_w) = \langle \psi(\vec{r}, t)\psi(\vec{r}, t_w)\rangle - \langle \psi(\vec{r}, t)\rangle\langle \psi(\vec{r}, t_w)\rangle, \tag{5.1}$$

ψ being a space $(\vec{r})$ and time dependent field, is crucial in the study of equilibrium and nonequilibrium dynamics [1]. In equilibrium, this exhibits

time translation invariance, i.e., results do not change due to the displacement $t - t_w$. But in nonequilibrium situations [2–4], the above invariance breaks down. E.g., in kinetics of phase transitions, with a growing length ℓ, as the system approaches the new equilibrium, i.e., with increasing age t_w, often referred to as the waiting time, the decay of the order-parameter autocorrelation becomes slower [4]. Such aging phenomena is an active area of research [5–16], with systems of interest ranging from biology to cosmology.

In many nonequilibrium problems with growing ℓ, there exists scaling of $C(t, t_w)$ as [4, 5, 17–20]

$$C(t, t_w) \sim x^{-\lambda^{ag}}; \; x = \ell/\ell_w, \tag{5.2}$$

in the limit $x \to \infty$, where ℓ and ℓ_w are the characteristic lengths at t and t_w. However, agreements between analytical theories, computer simulations and experiments are poor for the values of the exponent λ^{ag}. The scaling form for arbitrary x, of course, is a more general question to ask, answer to which is unsatisfactory. This holds true even for the simplests of the model systems.

In this chapter, we address the issue of aging following quench of a system from para- to ferromagnetic phase, in space dimensions $d = 2$ and 3. For such a transition, the bounds

$$\frac{d}{2} \leq \lambda^{ag} \leq d, \tag{5.3}$$

provided by Fisher and Huse (FH) [18], justifiable (including the expectation

for a power law) [19] from the average order-parameter values at times t_w and t within a region of the system, work well. There also exist [19] analytical calculations that predict the values of λ^{ag} in various dimensions. Due to the lack of knowledge about the small x behavior of $C(t, t_w)$ and finite-size effects in computer simulations, these numbers are not appropriately confirmed. In this work, we obtain *a full form of the autocorrelation function*, empirically. Via finite-size scaling analysis [21, 22], using this full form, we *estimated* λ^{ag} *rather accurately,* for a Ginzburg-Landau model in $d = 2$ and 3, which is necessary to understand the behavior of autoresponse function as well. Further, our study provides *useful information on the finite-size effects.* The method used here to obtain the full form using the numerical data is unique. This full form facilitated the application of finite-size scaling. Due to the lack of a "workable" full form of the autocorrelation function, finite-size scaling study of the aging problem was never done before.

5.2 Models and Methods

At the atomistic level, one typically considers the nearest neighbor Ising model [2, 22]

$$H = -J \sum_{<ij>} S_i S_j; \;\; S_i = \pm 1; \;\; J > 0, \tag{5.4}$$

where $S_i = +1(-1)$ corresponds to an up (down) spin on regular lattice, at a site i. This spin variable is equivalent to the order parameter ψ. Following quench from a high temperature (T) random phase to a temperature below

the critical value T_c, one studies aging, related to the evolution of domains, rich in up or down spins, via spin-flip Glauber (used for nonconserved order-parameter dynamics) Monte Carlo (MC) simulations [22].

In this chapter we, however, have presented results from a macroscopic model, which is the coarse-grained version of the nonconserved Ising model, known as time-dependent Ginzburg-Landau (TDGL) equation [4]

$$\frac{\partial\psi(\vec{r},t)}{\partial t} = -\frac{\delta F[\psi(\vec{r},t)]}{\delta\psi(\vec{r},t)}, \tag{5.5}$$

where F is the standard Ginzburg-Landau (GL) free energy functional, given by

$$\frac{F}{k_B T} = \int d\vec{r}\,\Big[-\frac{1}{2}\left(\frac{T_c}{T}-1\right)\psi^2 + \frac{1}{12}\left(\frac{T_c}{T}\right)^3\psi^4 + \frac{T_c}{2qT}a^2(\vec{\nabla}\psi)^2\Big], \tag{5.6}$$

with k_B, a and q being respectively the Boltzmann constant, the lattice constant and coordination number. The TDGL equation is solved via the standard Euler discretization technique [4]. Since no noise term is present in Eq. (5.5), this belongs to the mean field variety and thus $T_c = qJ/k_B$. Typically, one uses a scaled version of the free energy where ψ is normalized by the equilibrium temperature dependent order parameter. Thermal noise being in-built in the MC simulations of the Ising model, this study provides us with a comparison of dynamics in the mean field and the "exact" models. Note that we will only state the Ising model results here, instead of presenting.

All simulations were performed at $T = 0.6T_c$. Periodic boundary conditions were applied in all the directions. The average domain size was calculated from the probability distribution function $P(\ell_k, t)$ as [23]

$$\ell(t) = \int d\ell_k \; \ell_k \; P(\ell_k, t), \tag{5.7}$$

ℓ_k being obtained as the distance between two successive interfaces in any direction, in units of lattice constant. For the TDGL equation, as we observe, even though the order-parameter varies continuously between -1 and 1, we have used hard-spin configurations for this and other calculations. Note that in principle the order-parameter can take any value between $+\infty$ and $-\infty$. Time was calculated in a suitable dimensionless unit and for the solutions of these equations, we have used the space and time discretizations $\Delta x = 1$ and $\Delta t \leq 0.025$, respectively. All presented observables were averaged over multiple independent initial configurations, for smallest systems the numbers being 200 in $d = 2$ and 100 in $d = 3$; while for the largest systems the numbers are 80 and 40.

5.3 Results

In Fig. 5.1 we show evolution snapshots from four different times, in $d = 2$, where the orange dots represent $\psi > 0$. The growth observed in Fig. 5.1 is quantitatively demonstrated in Fig. 5.2 where we show a log-log plot of $\ell(t)$ vs t. Here note that for nonconserved scalar order parameter, $\ell(t) \sim t^{1/2}$, driven by interface curvature. The discrepancy of the simulation data, from

the continuous line, representing $t^{1/2}$, particularly at early time, is due to the presence of a nonzero initial length ℓ_0, such that [23]

$$\ell(t) = \ell_0 + A_\ell t^{1/2}. \tag{5.8}$$

In fact, a value of ℓ_0 of the order of only a few lattice constants can provide a misleading look on a double-log plot, for orders of magnitude in time. For the form in Eq. (5.8), the instantaneous exponent [24], $\alpha_i = d\ln\ell/d\ln t$, has the behavior [23, 25]

$$\alpha_i = \frac{1}{2}\left(1 - \frac{\ell_0}{\ell}\right). \tag{5.9}$$

Thus, if one obtains a linear behavior for α_i, as a function of $1/\ell$, with slope and intercept respectively equaling $-\ell_0/2$ and $1/2$, the growth exponent is $1/2$ starting from the very initial time. This is depicted in the inset of Fig. 5.2, from where the value of ℓ_0 turns out to be $\simeq 2.6$ which is a very reasonable number for a random initial configuration.

Results for $C(t, t_w)$ are presented in Fig. 5.3, as a function of ℓ/ℓ_w, for different values of t_w, with $L = 1024$. In Fig. 5.3, a nice collapse of data from all values of t_w demonstrate that scaling is obtained from rather early time. Deviation from this scaling at late times is due to the finite-size effects. Interestingly, the decay becomes faster at the finite-size affected region. The solid line in Fig. 5.3 corresponds to a power-law decay with $\lambda^{ag} = 1.29$. This value for λ^{ag} was predicted by Liu and Mazenko (LM) [19] who, using a Gaussian auxiliary field ansatz, in the limit $t \gg t_w$, constructed

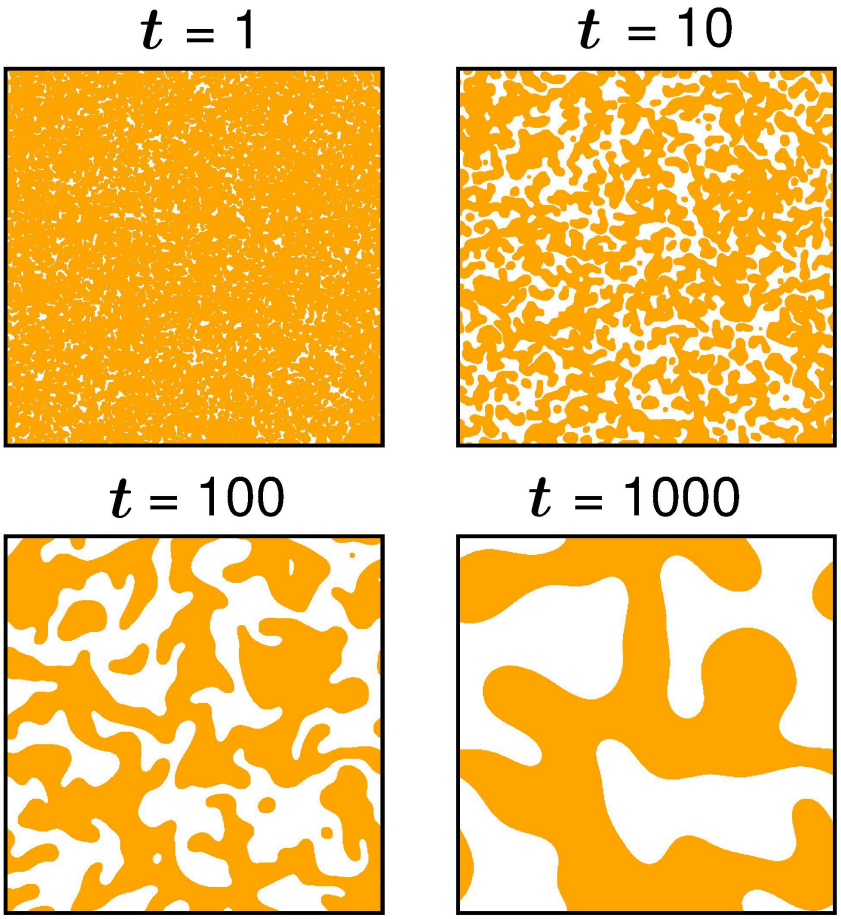

Figure 5.1: Evolution snapshots from TDGL equation simulations in $d = 2$ with $L = 1024$. Pictures from four different times are shown where the orange dots mark the locations of up spins.

the dynamical equation

$$\frac{\partial C(\vec{R}, t, t_w)}{\partial t} = \nabla^2 C(\vec{R}, t, t_w) + \frac{K}{t} C(\vec{R}, t, t_w), \tag{5.10}$$

where $C(\vec{R}, t, t_w)$ is a more general two-time correlation function involving two points separated by $\vec{R}$ in space, thus, $C(t, t_w) = C(0, t, t_w)$. In Eq. (5.10), $K = \pi/8\mu$, μ being a d-dependent constant $\simeq 1.1042$ and 0.5917 in $d = 2$ and

3, respectively [26]. In the asymptotic limit, from the solution of Eq. (5.10), LM obtained [19] $C(t,t_w) \sim \ell(t)^{-(d-\pi/4\mu)}$, which provides $\lambda^{ag} = 1.2887$ and 1.6726 in $d = 2$ and 3. These numbers certainly obey the FH bounds. In Fig. 5.3, a power-law fit to the region unaffected by finite system size provides a value much lower than 1.29. Nevertheless, the data appear to converge towards the exponent 1.29, from the lower-side. In such a situation, it is instructive to calculate the instantaneous exponent [18, 19, 24]

$$\lambda_i^{ag} = \frac{d\ln[1/C(t,t_w)]}{d\ln x}. \tag{5.11}$$

Results for λ_i^{ag}, with $L = 1024$ and $t_w = 100$, are presented in Fig. 5.4, as a function of ℓ_w/ℓ. Here we avoided data for very small x, related to decay to domain magnetization, and in region affected by finite system size. The presented data look quite linear

$$\lambda_i^{ag} = \lambda^{ag} - \frac{A_c}{x}, \tag{5.12}$$

which, however, does not have the same consequence as that in Eq. (5.9). Using Eqs. (5.11) and (5.12), one obtains a full scaling function as

$$C(t,t_w) = Bx^{-\lambda^{ag}} \exp(-A_c/x), \tag{5.13}$$

which, for $x \to \infty$, converges to the scaling form (5.2). By fixing $C(t,t_w)$ to 1 at $x = 1$, one can obtain the normalization constant B. But we will keep it soft, to avoid difficulty due to fast decay for x very close to 1. For

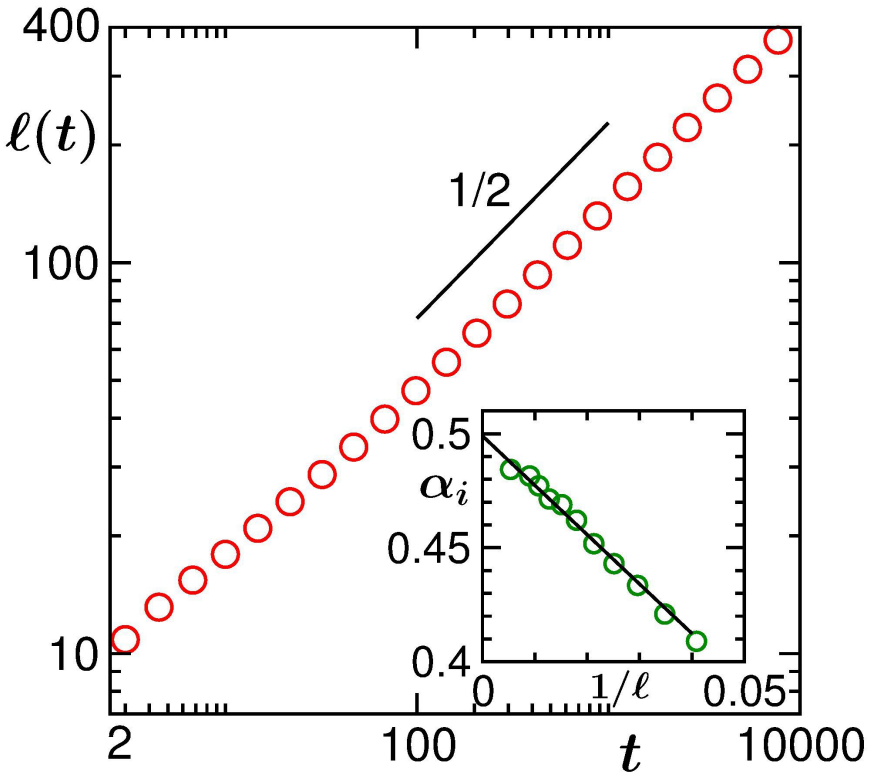

Figure 5.2: Plot of average domain size, $\ell(t)$, as a function of time, for $2-d$ TDGL equation with $L = 1024$. The continuous line there represents $t^{1/2}$ behavior. The inset shows corresponding instantaneous exponent, α_i, as a function of $1/\ell$.

simulation data, where one deals with finite systems, ℓ is never much larger than ℓ_w. In that case, knowledge of such correction is important. Here we mention that there have been efforts [5] to obtain the full scaling form of $C(t, t_w)$ from analytical theories. The best available expression [5], also shown [6] to be valid for q-state Potts model ($q > 2$), obtained by using local scale invariance, is certainly not simple and contains number of adjustable parameters more than five, excluding λ^{ag}. There [5, 6], value of λ^{ag}, to the best of our understanding, was obtained from the extrapolation of λ_i^{ag}, thus

accepting the exponential factor obtained by us. While we do not claim that Eq. (5.13) is the exact description of $C(t, t_w)$, accuracy of it can be checked from more sophisticated analysis, e.g., finite-size scaling (FSS) [21,22], which in turn can provide the value of λ^{ag}. Here we mention that FSS with only the power-law failed to obtain collapse of data from different system sizes. On the other hand, FSS with the expression of Ref. [5] is rather inconvenient due to the large number of adjustable constants. Of course, one could have obtained the value of λ^{ag} by extrapolating λ_i^{ag}. But often numerical derivatives involve huge errors and fluctuations. Also finite-size effects can lead one to wrong conclusions. We mention here that λ_i^{ag} in the Fig. 5.4 extrapolates to $\lambda^{ag} \simeq 1.30$, in very nice agreement with the LM value. Authenticity of this number, fearing any size effects, we aim to justify via application of FSS.

In the FSS analysis, to account for the size effects, we introduce a finite-size scaling function $Y(y = L/\ell)$ such that

$$Y(y) = C(t, t_w) x^{\lambda^{ag}} \exp(A_c/x). \tag{5.14}$$

When λ^{ag} and A_c are chosen appropriately, Y should be independent of the system size, thus, providing a collapse of data coming from different system sizes. In the large y limit, Y should be a constant providing the value of B. As the finite-size effects come (at small enough value of y), Y should start decreasing.

In Fig. 5.5 we show the finite-size data collapse in $d = 2$. Data from four different system sizes are used, all for $t_w = 100$. Here we have fixed λ^{ag} to the LM value and adjusted A_c. The data collapse certainly looks very good. The

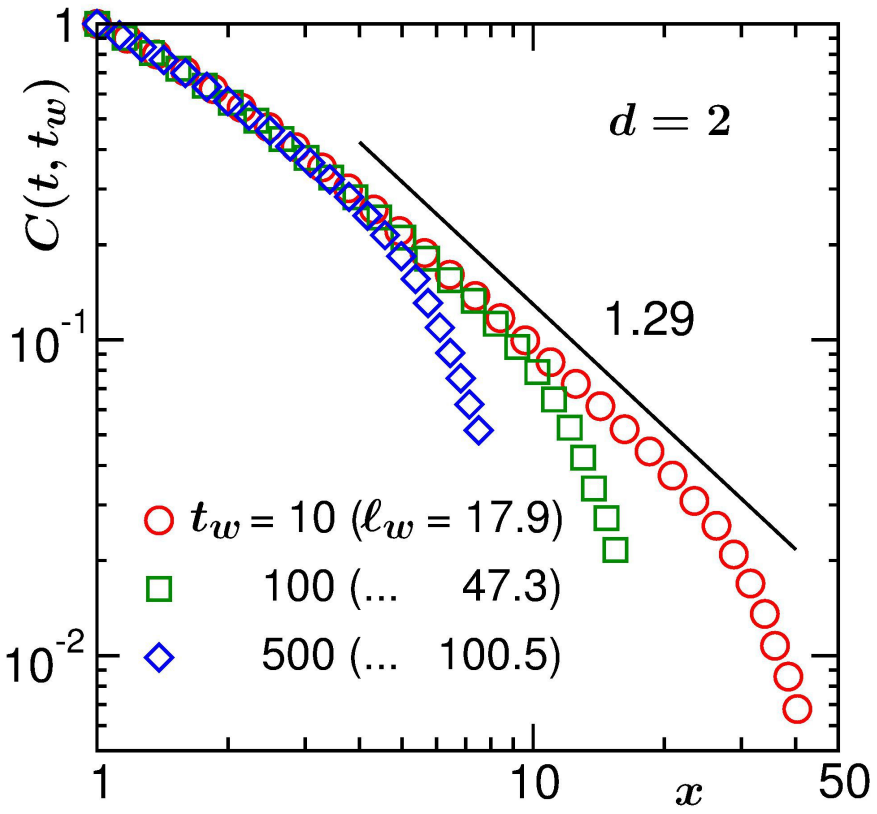

Figure 5.3: Plots of autocorrelation function, $C(t, t_w)$, vs x, for three different values of t_w, as indicated on the figure. These results are from the numerical solutions of $d = 2$ TDGL equation, with $L = 1024$. The results are normalized such that $C(t, t_w) = 1$ at $x = 1$.

best collapse, however, is obtained for $A_c = 0.68$ and $\lambda^{ag} = 1.30$. In Fig. 5.6, we demonstrate the same exercise for $d = 3$ TDGL equation, with $t_w = 10$, by fixing λ^{ag} to the LM value again. In this case, the best collapse parameters are $A_c = 0.96$ and $\lambda^{ag} = 1.66$. Needless to mention, in both the dimensions, values of λ^{ag} are in very good agreement with the LM predictions. Recalling that no noise term [2–4] was used in the TDGL equation, if the values of λ^{ag} quoted above are in agreement with the nonconserved Ising model, that contains noise in Monte Carlo simulations, one can conclude that, at least

asymptotically, the noise is irrelevant in such nonequilibrium dynamics. In the equilibrium critical phenomena, however, absence of noise makes the Ginzburg-Landau model belong to an universality class other than the Ising one. Another important observation here is that A_c is higher in $d = 3$, implying a stronger deviation from the power-law behavior, for small x, than in $d = 2$.

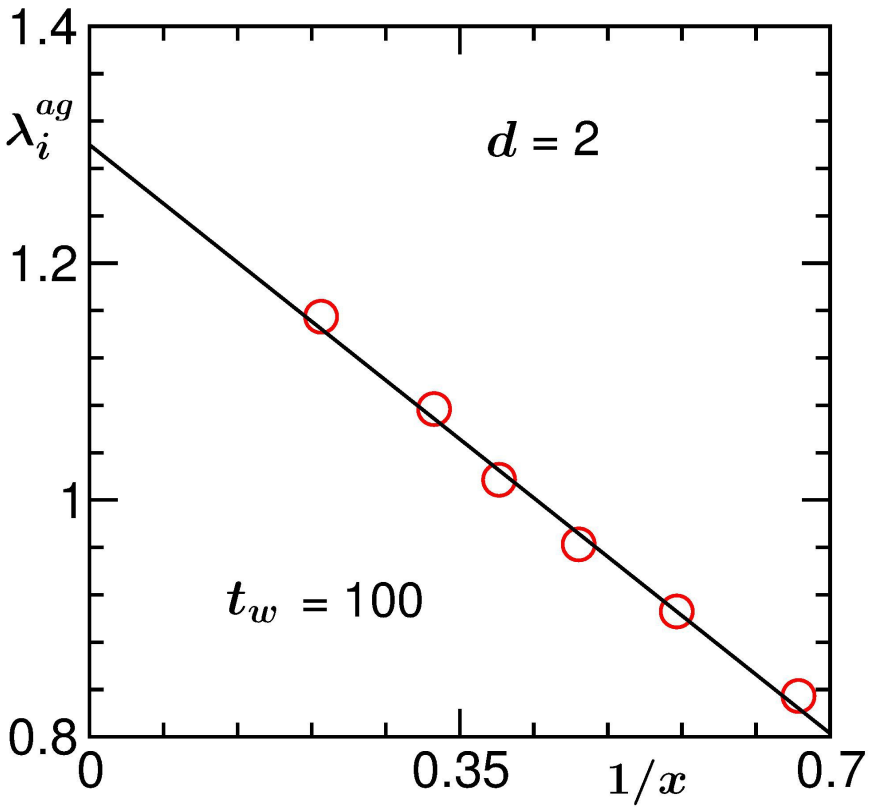

Figure 5.4: Plot of instantaneous exponent, λ_i^{ag}, as a function of $1/x$, for $d = 2$, $t_w = 100$ and $L = 1024$.

To obtain [27] the λ^{ag} values for the Ising model, the same analysis technique was used. There the best data collapse was obtained for $A_c = 0.80$ and $\lambda^{ag} = 1.32$ in $d = 2$; $A_c = 1.13$ and $\lambda^{ag} = 1.69$ in $d = 3$. These numbers

for λ^{ag} are certainly consistent with those obtained for the TDGL equation. However, the Ising values are systematically higher than the TDGL ones, albeit marginally, that can have route other than noise as well, e.g., truncation of the GL free energy after the fourth order term. Higher values of A_c, in both $d = 2$ and $d = 3$, is indicative of strong correction in Ising case than in TDGL.

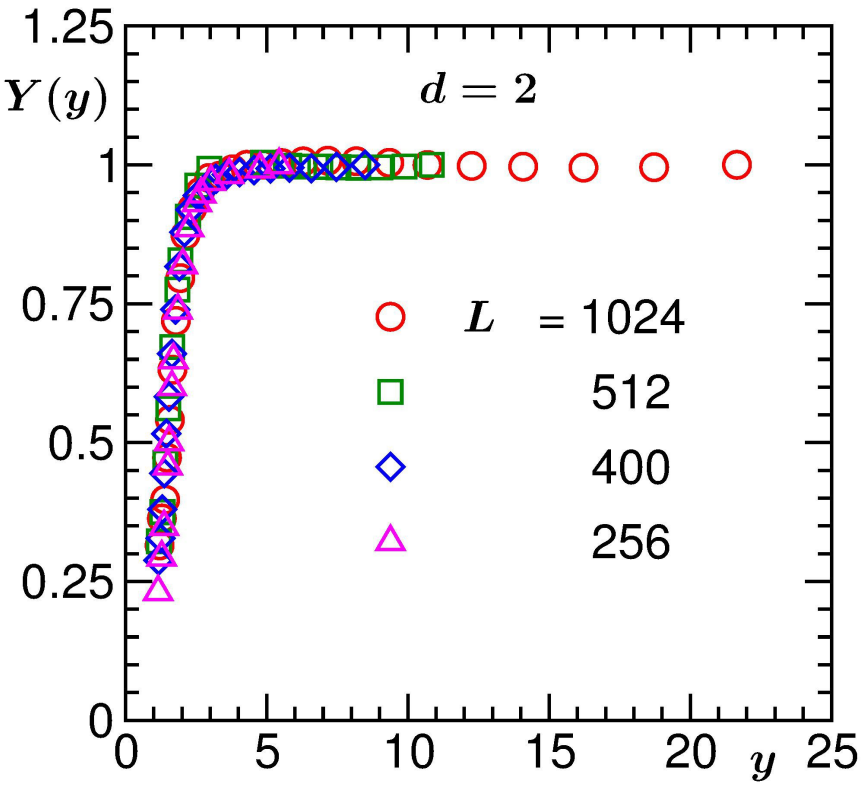

Figure 5.5: Finite-size scaling function Y is plotted vs y, for $d = 2$ TDGL equation. Data from four different system sizes are used.

From the deviation of flat behavior in these finite-size scaling plots, one can estimate the on-set of finite-size effects. This, for the TDGL equation appears when the average domain size becomes approximately 30% of the

system size. On the other hand, for Ising case, it has been checked that, finite-size effects appear when $\ell = 0.4L$. Whether this difference and the above are due to noise or truncation of higher order terms in the GL Hamiltonian requires very careful study.

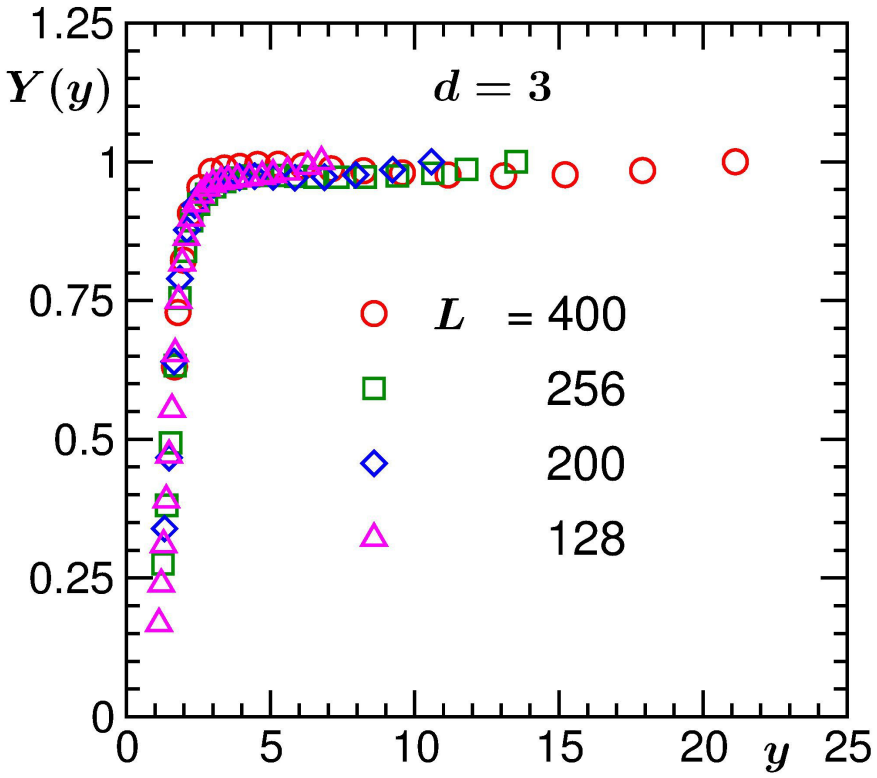

Figure 5.6: Finite-size scaling function Y is plotted vs y, for $d = 3$ TDGL equation. Data from four different system sizes, $L = 400, 256, 200$ and 128, are used.

Previously, a number of simulations reported values of λ^{ag} reasonably close to the LM one in $d = 2$, though did not exclude [5, 6] the possibility $\frac{5}{4}$. In data fitting procedure, the obtained value depends upon the chosen region, statistical fluctuation in the data, finite-size effects, etc. These negative features, however, are better taken care of by finite-size scaling analysis. On

the other hand, most reliable past study [19] in $d = 3$ reported a central value $= 1.84$ with huge error bar. Our estimates for λ^{ag} in both the dimensions are very close to LM values, showing deviation within 2% only.

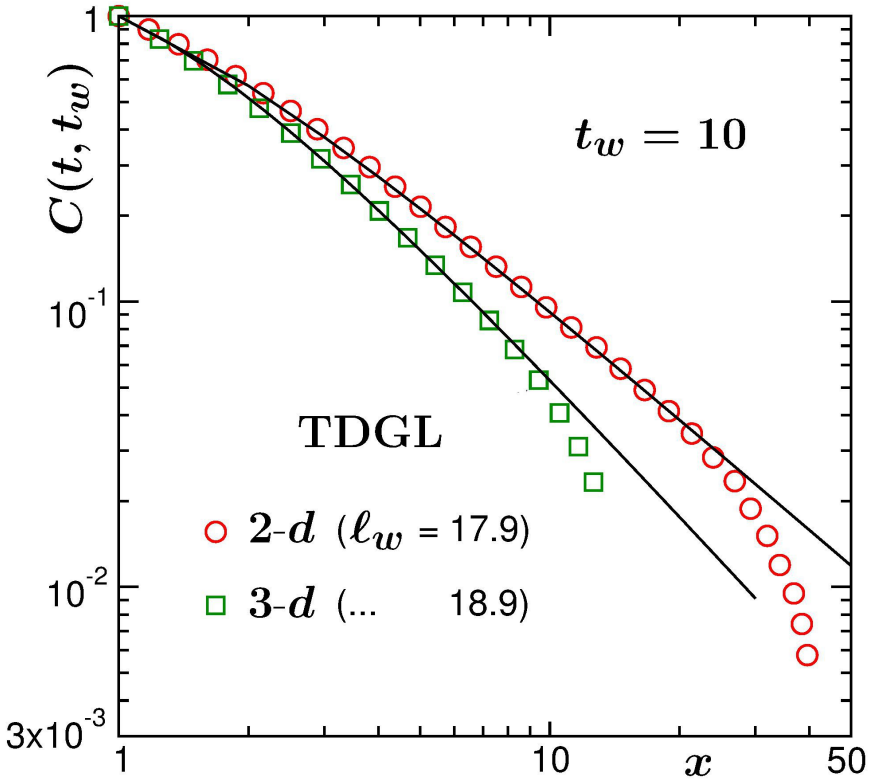

Figure 5.7: $C(t, t_w)$ vs x from TDGL equation solutions in $d = 2$ and 3. The value of t_w is mentioned on the figure. The continuous lines correspond to Eq. (5.13) with best parameter values, mentioned in the text.

Finally, in Fig. 5.7 we show the plots of $C(t, t_w)$ as a functions of ℓ/ℓ_w in $d = 2$ and $d = 3$. There, the continuous lines are the full form (5.13) with the best parameter values obtained from FSS. It is seen that a rather wide range of data are consistent with this functional form.

5.4 Summary

Aging in ferromagnetic ordering has been studied via time-dependent Ginzburg-Landau equation in $d = 2$ and 3. We have obtained a full scaling form of the autocorrelation function empirically. This was used to obtain the power-law exponent in the asymptotic limit via application of the finite-size scaling analysis. This study provides accurate information on the exponents for late time power-law decay of $C(t, t_w)$. These values are consistent with those from the Ising model both in $d = 2$ [$\lambda^{ag} = 1.30 \pm 0.03$ (TDGL); 1.32 ± 0.04 (Ising)] and 3 [$\lambda^{ag} = 1.66 \pm 0.03$ (TDGL); 1.69 ± 0.04 (Ising)], which are in excellent agreement with the theoretical calculations by Liu and Mazenko (LM) [19]. Even through, due to the approximate nature of the exponential correction factor, our analysis is unable to rule out the value $\lambda^{ag} = 5/4$ in $d = 2$, the closeness of our values, in both $d = 2$ and 3, to the LM theory is suggestive of validity of the latter. Unfortunately, despite more concrete nature of the work on the full form of the autocorrelation function in Ref. [5], it is not suitable for a finite-size scaling analysis. It will be interesting to apply our method to obtain the exponents for auto-response function. Even though there is a belief that the exponents for the two cases should be same, there is no proof for it [28]. Furthermore, we have obtained important information on the finite-size effects. Our study obtains slightly smaller aging exponents for the TDGL equation, that lacks thermal noise, compared to Ising model. This information should be subject to further check. A study of the time-dependent Ginzburg-Landau equation by incorporating noise, in accordance with fluctuation-dissipation rule, will

be useful in this context.

Even though the values of λ^{ag} are within the bounds predicted by Fisher and Huse [18], in case of conserved order-parameter dynamics this may not be the case. Yeung, Rao and Desai [17] obtained more general lower bounds, involving both conserved and nonconserved dynamics, from the analysis of the behavior of equal time structure factor. These converge to the Fisher and Huse bounds in the nonconserved case. Nevertheless, the situation with respect to the actual values of the autocorrelation exponent, and even an understanding whether the scaling of it, with respect to ℓ/ℓ_w, exists, are unsatisfactory for dynamics with conserved order-parameter. For the latter, some preliminary studies [15, 16] recently reported an exponential decay of $C(t, t_w)$ in the hydrodynamic regime of fluid phase separation. These studies are based on molecular dynamics simulations of atomistic models. Considering the demanding nature of molecular dynamics, it has only been possible to access a limited part in the hydrodynamic regime. Thus, further studies are needed to arrive at satisfactory understanding in these more complex systems.

Bibliography

[1] J.-P. Hansen and I.R. McDonald, *Theory of simple Liquids* (Academic Press, London) 2006.

[2] A. Onuki, *Phase Transition Dynamics* (Cambridge University Press, Cambridge) 2002.

[3] A.J. Bray, Adv. Phys., **51** (2002) 481.

[4] *Kinetics of Phase Transitions*, edited by S. Puri and V. Wadhawan (CRC Press, Boca Raton) 2009.

[5] M. Henkel, A. Picone and M. Pleiming, Europhys. Lett., **68** (2004) 191.

[6] E. Lorenz and W. Janke, Europhys. Lett., **77** (2007) 10003.

[7] R. Mathieu, P. Nordblad, D.N.H. Nam, N.X. Phuc and N.V. Khiem, Phys. Rev. B, **63** (2001) 1774405.

[8] B. Abou and F. Gallet, Phys. Rev. Lett., **93** (2004) 160603.

[9] M. Costa, A.L. Goldberger and C.-K. Peng, Phys. Rev. Lett., **95** (2005) 198102.

[10] G.G. Kenning, G.F. Rodriguez and R. Orbach, Phys. Rev. Lett., **97** (2006) 057201.

[11] L. Berthier, Phys. Rev. Lett., **98** (2007) 220601.

[12] D. El Masri, L. Berthier and L. Cipelletti, Phys. Rev. E, **82** (2010) 031503.

[13] E. Bouchbinder and J.S. Langer, Phys. Rev. E, **83** (2011) 061503.

[14] J. Bergli and Y.M. Galperin, Phys. Rev. B, **85** (2012) 214202.

[15] S. Ahmad, F. Corberi, S.K. Das, E. Lippiello, S. Puri and M. Zannetti, Phys. Rev. E, **86** (2012) 061129.

[16] S. Majumder and S.K. Das, Phys. Rev. Lett., **111** (2013) 055503.

[17] C. Yeung, M. Rao and R.C. Desai, Phys. Rev. E, **53** (1996) 3073.

[18] D.S. Fisher and D.A. Huse, Phys. Rev. B, **38** (1988) 373.

[19] F. Liu and G.F. Mazenko, Phys. Rev. B, **44** (1991) 9185.

[20] S.N. Majumderand D.A. Huse, Phys. Rev. E, **52** (1995) 270.

[21] M.E. Fisher in *Critical Phenomena*, editedby M.S. Green (Academic Press, London) 1971, p.1.

[22] D.P. Landau and K. Binder, *A Guide to Monte Carlo Simulations in Statistical Physics* (Cambridge University Press, 3rd Edition) 2009.

[23] S. Majumder and S.K. Das, Phys. Rev. E, **81** (2010) 050102.

[24] D.A. Huse, Phys. Rev. B, **34** (1986) 7845.

[25] J.G. Amar, F.E. Sullivan and R.D. Mountain, Phys. Rev. B, **37** (1988) 196.

[26] G.F. Mazenko, Phys. Rev. B, **42** (1990) 4487.

[27] J. Midya, S. Majumder and S.K. Das, J. Phys.: Condens. Matter, **26** 452202 (2014).

[28] G.F. Mazenko, Phys. Rev. E, **69** (2014) 016114.

Chapter 6

Dimensionality dependence of aging in kinetics of diffusive phase separation: Behavior of order-parameter autocorrelation

6.1 Introduction

Understanding of aging phenomena in out of equilibrium systems, except for special situations like steady state, is of fundamental importance [1]. There have been serious activities on this issue concerning living [2,3] as well as nonliving matters, especially in problems related to domain growth [1, 4–14] and glassy dynamics [15–19]. Among other quantities, aging phenomena

is studied via the two-time autocorrelation function [4]

$$C(t,t_w) = \langle \psi(\vec{r},t)\psi(\vec{r},t_w)\rangle - \langle \psi(\vec{r},t)\rangle\langle \psi(\vec{r},t_w)\rangle, \tag{6.1}$$

where ψ is a space ($\vec{r}$) and time dependent order parameter, t_w is the waiting time or age of the system, t ($> t_w$) is the observation time and the angular brackets represent statistical averaging over space and initial configurations.

In phase ordering systems [20], though time translation invariance is broken, $C(t,t_w)$ is expected to exhibit scaling with respect to t/t_w. Important examples are ordering of spins in a ferromagnet, kinetics of phase separation in a binary ($A+B$) mixture, etc., having been quenched to a temperature (T) below the critical value (T_c), from a homogeneous configuration. Though full forms are unknown even for very simple models, asymptotically $C(t,t_w)$ is expected to obey power-law scaling behavior as [4, 6]

$$C(t,t_w) \sim x^{-\lambda^{ag}};\ x = \ell/\ell_w. \tag{6.2}$$

In Eq. (6.2), ℓ and ℓ_w are the average sizes of domains, formed by spins or particles of similar type, at times t and t_w, respectively. Typically ℓ and t are related to each other via power-laws.

For nonconserved order-parameter dynamics, e.g., ordering in a ferromagnet, such scaling has been observed and the values of the exponent λ^{ag} have been accurately estimated [6, 14] in different space dimensions d. There the

exponents follow the bounds

$$\frac{d}{2} \leq \lambda^{ag} \leq d, \tag{6.3}$$

predicted by Fisher and Huse (FH) [4]. In kinetics of phase separation in solid mixtures, for which the order parameter is a conserved quantity, the state of understanding is far from satisfactory, due to various difficulties. There, values of λ^{ag} remain unknown, except for lower bounds discussed below.

Yeung et al. [7] put a more general lower bound on λ^{ag} as

$$\lambda^{ag} \geq \frac{(\beta' + d)}{2}, \tag{6.4}$$

where β' is the exponent for small wave-vector power-law enhancement of equal time structure factor which, depending upon the dynamics, becomes important for $t_w \gg 1$, as stated below. In nonconserved dynamics, $\beta' = 0$ and so the FH lower bound is recovered. For conserved order parameter dynamics, on the other hand, $\beta' = 4$ in both $d = 2$ and 3 at late time. Thus, the FH upper bound is violated. Simulations of the Cahn-Hilliard (CH) equation [20]

$$\frac{\partial \psi(\vec{r}, t)}{\partial t} = -\nabla^2 \Big[\psi(\vec{r}, t) + \nabla^2 \psi(\vec{r}, t) - \psi^3(\vec{r}, t) \Big], \tag{6.5}$$

by Yeung et al. [7], observed $\lambda^{ag} > 3$ in $d = 2$, consistent with their bound. From these simulations, the authors, however, did not accurately quantify λ^{ag}; scaling of $C(t, t_w)$ with respect to t/t_w was not demonstrated; focus was rather on the sensitivity of the aging dynamics to the correlations in the

initial configurations. Situation is far worse in $d = 3$, with respect to the CH equation as well as the conserved Ising model [1, 20]

$$H = -J \sum_{<ij>} S_i S_j;\ S_i = \pm 1;\ J > 0. \tag{6.6}$$

In this chapter, we have presented results from the CH model, used for understanding diffusive phase separation in solid mixtures, in $d = 2$ (on regular square lattice) and $d = 3$ (on simple cubic lattice), via extensive simulations, to quantify the decay of $C(t, t_w)$. Though the presented results are from CH model, the conserved Ising model results will be stated (without presenting) for comparison. We observe scaling of $C(t, t_w)$ with respect to x which tends to a power-law for large x. Via computations of the instantaneous exponent [21–23]

$$\lambda_i^{ag} = -\frac{d \ln[C(t, t_w)]}{d \ln x}, \tag{6.7}$$

and application of the finite-size scaling technique [24, 25], we find that $\lambda^{ag} \simeq 3.6$ in $d = 2$ and $\simeq 7.5$ in $d = 3$. Though these numbers respect the bounds of Yeung et al. [7], the high value in $d = 3$ is surprising. Furthermore, a general form for the full scaling functions has been obtained empirically.

Rest of the chapter is organized as follows. We describe the methodology in section II. Results are presented in section III. Finally, section IV concludes the chapter with a brief summary and discussion.

6.2 Methods

We numerically solve the CH equations on a regular lattice (applying the periodic boundary conditions in all possible directions) via Euler discretization method. Due to the coarse-grained nature of the CH equation, one can explore large effective length in simulations. There the order parameter corresponds to a coarse-graining [26] of the Ising spins, typically over the equilibrium correlation length ξ. Then, a positive value of ψ means an A-rich region and for a B-rich region, ψ will have a negative number. For the calculation of $C(t, t_w)$, we have used hardened configurations for ψ with numbers $+1$ and -1. A noise term is intentionally omitted to investigate if there is any strong effect of the latter, since in the Ising model it is automatically included and the results will be discussed in comparison with the latter. We state at the beginning, within the accuracy of the simulations, we do not observe any significant difference between the CH model and the conserved Ising model results.

The average domain length, ℓ, was measured from the first moment of domain size distribution, $P(\ell_d, t)$, as [23]

$$\ell = \int \ell_d \; P(\ell_d, t) \; d\ell_d, \tag{6.8}$$

where ℓ_d is the distance between two successive domain boundaries in any direction. Throughout the chapter, all lengths are presented in units of the lattice constant a. The time t is expressed in dimensionless units [27]. All results, for both the dimensions, are presented after averaging over at least 50 initial realizations, for quenches from random configurations, mimicking

$T = \infty$, to $T = 0.6T_c$. Such value, instead of 0, of T was chosen to avoid metastability that is often encountered in conserved dynamics at low T.

6.3 Results

In Fig. 6.1 we show evolution snapshots from two different times, for the $d = 2$ CH equation, where the orange and the white colors represent A- and B-rich regions, respectively. The growth of domains that we observe in Fig. 6.1 is quantitatively demonstrated in Fig. 6.2 where we have plotted ℓ as a function of t, on log-log scale. In this figure, the late time simulation data are very much consistent with the solid line, that corresponds to a power-law with exponent 1/3. This confirms the validity of the Lifshitz-Slyozov growth-law which is expected for conserved order-parameter dynamics with single particle diffusion.

In Fig. 6.3 we present quantitative results for the structure shown in Fig. 6.1. There we have plotted $\ell^{-d}S(k,t)$ as a function of $k\ell$. Recall that $S(k,t)$ is the Fourier transform of the two point equal time correlation function $C(r,t)$. Nice collapse of data from different times implies self-similarity. The solid line in the large $k\ell$ region corresponds to the Porod law. On the other hand, the power-law enhancement in the small abscissa region has the exponent $\beta' = 4$, confirming the expectation for conserved dynamics, as stated above. This value remains the same in $d = 3$. In the inset of this figure we show the corresponding results for the TDGL equation. In this case we have $\beta' = 0$.

In Fig. 6.4, we present the plots of $C(t, t_w)$, vs x, for different values of t_w, from the solutions of the CH model in $d = 2$. As seen, one needs

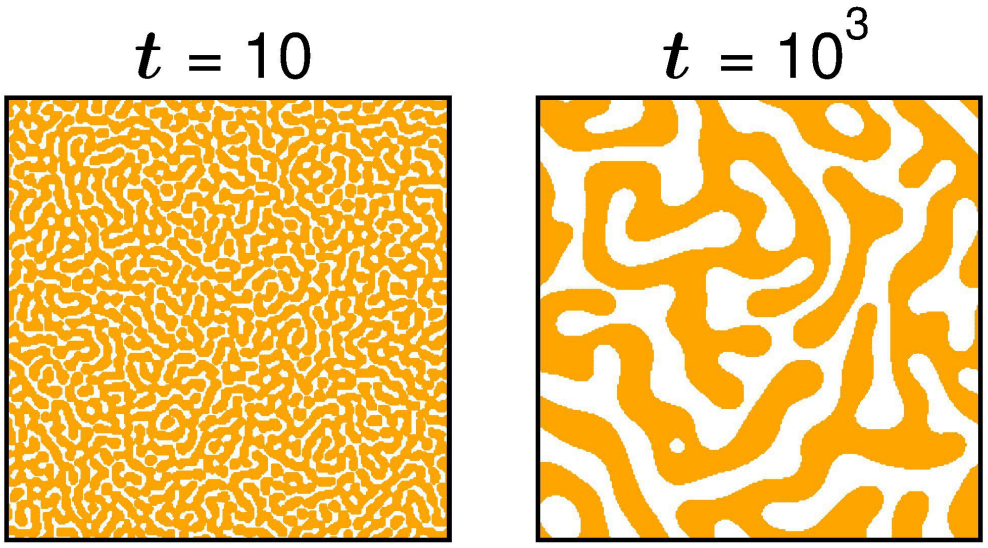

Figure 6.1: Evolution snapshots at two different times from the $d = 2$ CH model with $L = 400$. In the figure the orange and the white dots are marking the locations of the A- and B-types of particles, respectively.

large enough value of t_w to observe appropriate scaling behavior (collapse of data), compared to ordering in ferromagnets [14]. It appears that late occurrence of scaling in conserved dynamics is due to slow domain growth. Our observation suggests, scaling is visible from $\ell_w \simeq 10$ lattice constants, irrespective of conservation of the order parameter. Between the two data sets with largest values of t_w, the deviation from each other, for large x, is due to the finite-size effects. Similar plots for $d = 3$ are presented in Fig. 6.5. Here we have chosen t_w values from the scaling regime only. Compared to $d = 2$, scaling in $d = 3$ starts earlier because of the fact that the domain growth amplitude is larger in the latter dimension. Again, deviation from the master curve, starting at different values of x for different t_w, are primarily related to the finite-size effects. In both these figures, 6.4 and 6.5, the system sizes are kept fixed, only the values of t_w are varied. A similar observation,

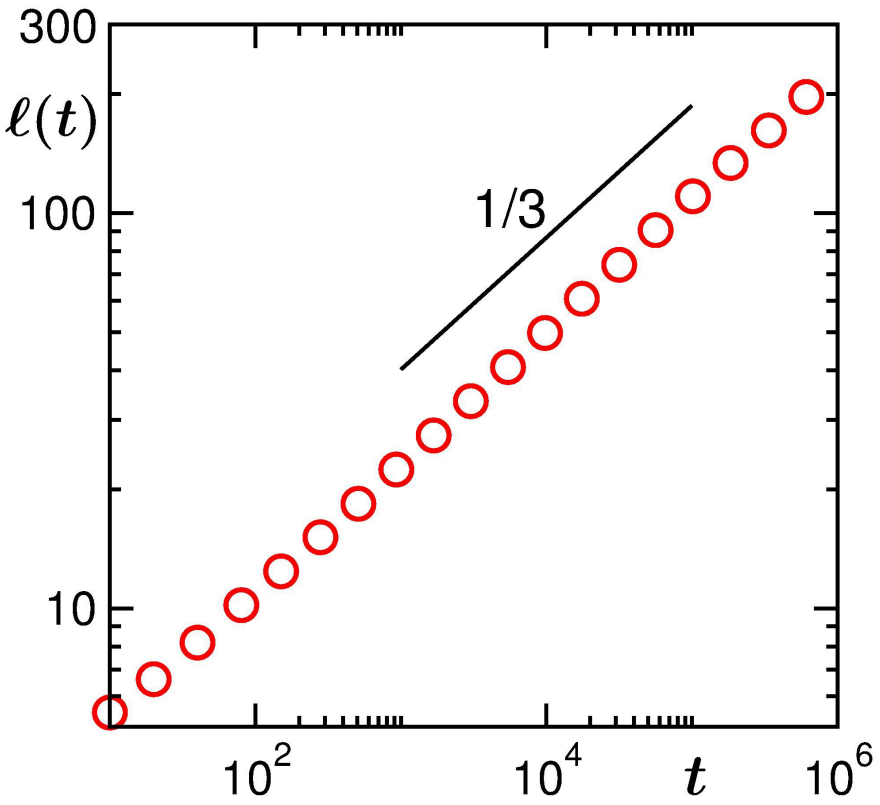

Figure 6.2: Plot of average domain length, ℓ, vs t, on log-log scale, for $d = 2$ CH equation. The simulation data are nicely consistent with the solid line that corresponds to a power-law with exponent 1/3.

with respect to the above mentioned deviation for different choices of t_w, can be made, when, for same value of t_w, data are presented for different system sizes.

In the scaling parts, both in Figs. 6.4 and Fig. 6.5, continuous bending is observable, in these log-log plots. Thus, power-laws, if exist, carry corrections. The solid lines in these figures are power-law decays with exponents 3 and 3.5, respectively, corresponding to the bounds of Yeung et al. [7]. For large x, simulation data in $d = 2$ appear reasonably consistent with the bound. The asymptotic exponent, in $d = 3$, on the other hand, appear much

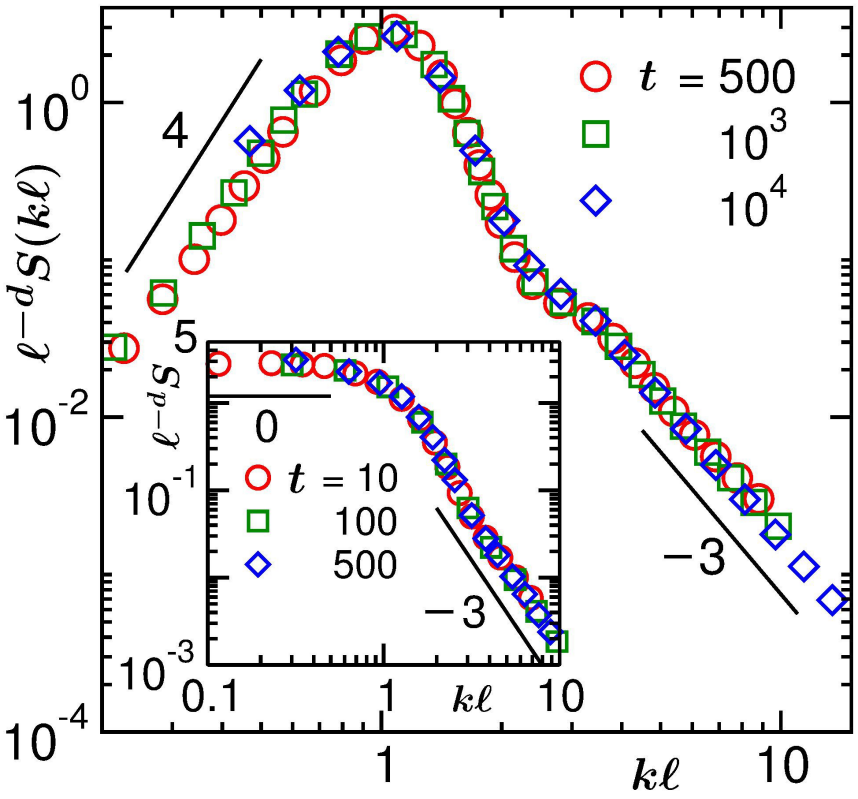

Figure 6.3: Scaling plot of the structure factor, $\ell^{-d}S(k\ell)$ vs $k\ell$, for the 2D CH equation. The solid lines correspond to power-laws with exponents 4 and -3. The inset shows the same exercise for the 2D TDGL equation. The solid lines there have power-law exponents 0 and -3.

higher than 3.5.

With the expectation that power laws indeed exist asymptotically, in Fig. 6.6 we present plots of instantaneous exponents [6, 14, 21–23] λ_i^{ag}, for both $d = 2$ and 3, vs $1/x$. In addition to providing λ^{ag}, from the extrapolations to $x = \infty$, such exercise may be useful for obtaining crucial information on the full forms of $C(t, t_w)$. For $d = 2$, the data are obtained for $t_w = 5 \times 10^3$, and for $d = 3$, the data correspond to $t_w = 10^3$. In both the cases, the results appear reasonably linear [6, 14]. The solid lines there are extrapolations to

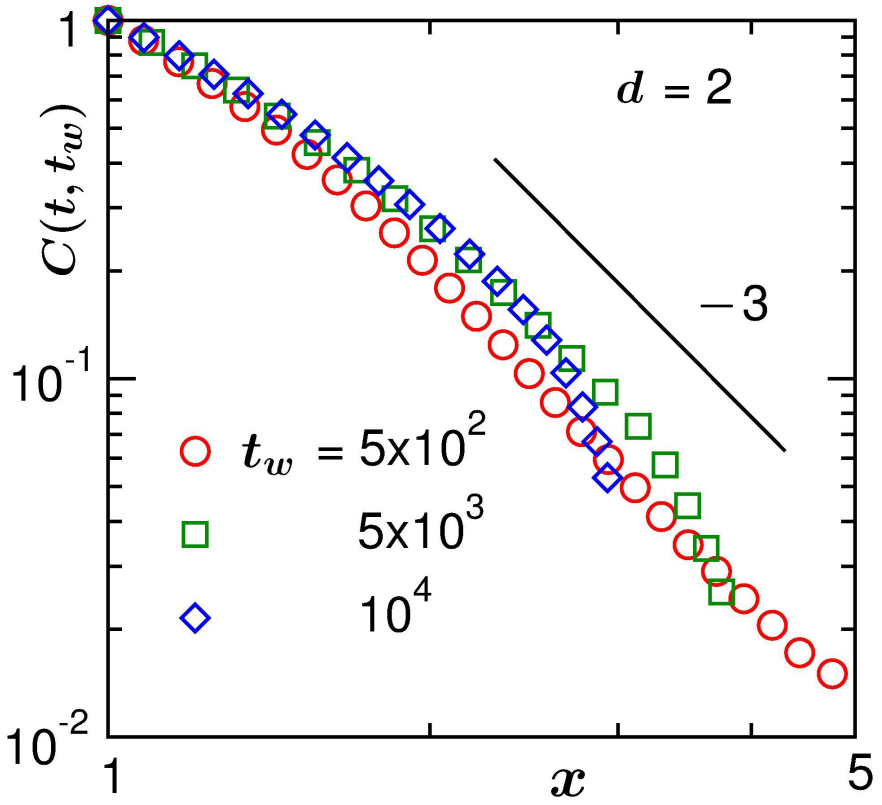

Figure 6.4: Autocorrelation function, $C(t, t_w)$, from the $d = 2$ Cahn-Hilliard model, are plotted vs x $(= \ell/\ell_w)$, for different values of t_w (fixing the L value at 256). The solid line there corresponds to a power-law decay with exponent 3.

$x = \infty$, accepting the linear trends. These indicate $\lambda^{ag} \simeq 3.60$ in $d = 2$ and $\simeq 7.80$ in $d = 3$. Again, while the value in $d = 2$ is consistent and close to the bound of Yeung et al. [7], the observation of surprisingly high number in $d = 3$ is certainly interesting. We intend to obtain more accurate values via appropriate finite-size scaling analyses [24, 25]. This is considering the fact that the choice of the regions in Fig. 6.6, for performing least-square fitting, is not unambiguous due to finite-size effects and strong statistical fluctuations at large x. Also, for very small x (data excluded), there is rapid

decay of $C(t, t_w)$ related to the fast equilibration of domain magnetization ψ. Here note that this latter contribution decays from $(1 - \psi^2)$ to 0. At this temperature (noting that critical phenomena is typically observed within 10% of T_c, we are significantly below the critical regime), thus, the time scale of this equilibration is short and so the analysis gets affected only very close to $x = 1$.

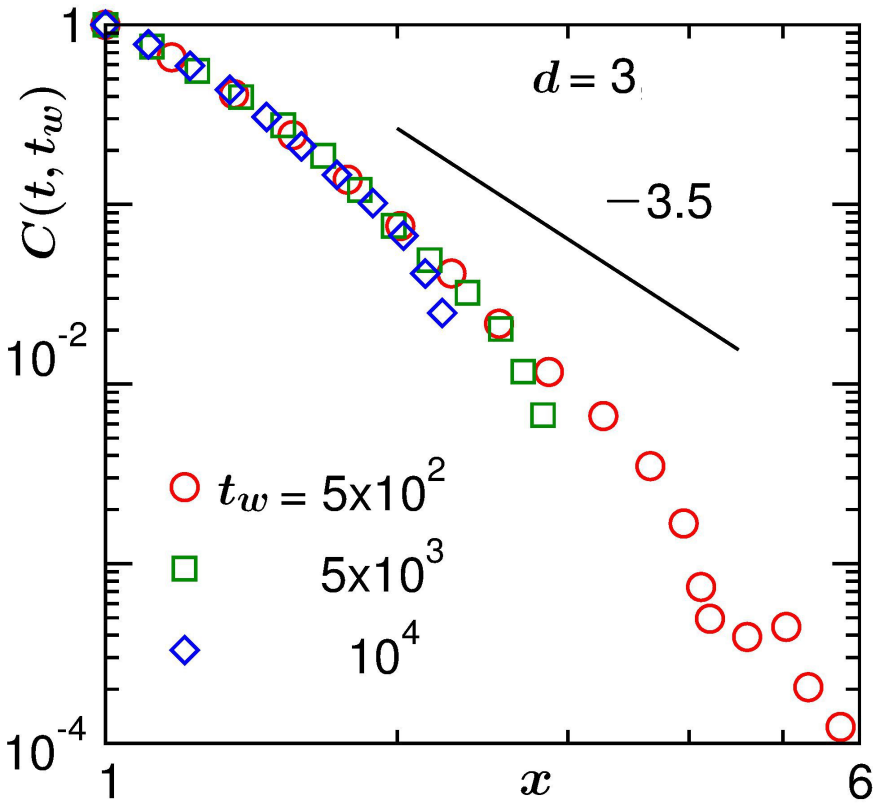

Figure 6.5: Same as 6.4 but for the $d = 3$ CH model with $L = 200$. The solid line there has a power-law decay exponent 3.5.

Since the corrections to the asymptotic decay laws are seen to be strong for finite x, a reasonable idea about the full forms of the decays is essential for accurate finite-size scaling analyses. Those, however, are nonexistent in

the literature. Here we obtain the forms empirically. Assuming power-law behavior of the data sets in Fig. 6.6, we write

$$\lambda_i^{^{ag}} = \lambda^{^{ag}} - \frac{A_c}{x^{\gamma'}}, \tag{6.9}$$

A_c, γ' being constants. This, via Eq. (6.7), provides

$$C(t, t_w) = C_0 \exp\Big(- \frac{A_c}{\gamma'} x^{\gamma'} \Big) x^{-\lambda^{^{ag}}}, \tag{6.10}$$

C_0 being a constant. For finite-size scaling analysis, one needs to introduce a scaling function

$$Y(y) = C(t, t_w) \exp\Big(\frac{A_c}{\gamma'} x^{\gamma'} \Big) x^{\lambda^{^{ag}}}; \quad y = L/\ell. \tag{6.11}$$

The variable y gets separated from x because of the fact that $y = \frac{L/\ell_w}{x}$ and x contains ℓ_w in the denominator. For appropriate choices of A_c, γ' and $\lambda^{^{ag}}$, one should obtain a master curve for Y, when data from different system sizes are used. If the above mentioned factorization between x and y truly holds, we should obtain collapse of data for different values of t_w as well. We will demonstrate that this indeed is true. The behavior of Y should be flat in the finite-size unaffected region and a deviation from it will mark the onset of finite-size effects.

By examining the data in Fig. 6.6, we fix γ' to 1. In Fig. 6.7, we show a finite-size scaling plot for data from the $d = 2$ CH model, using different values of L and t_w. The presented results correspond to best collapse, obtained for $A_c = 2.25$ and $\lambda^{^{ag}} = 3.47$. The value of t_w used for different L is

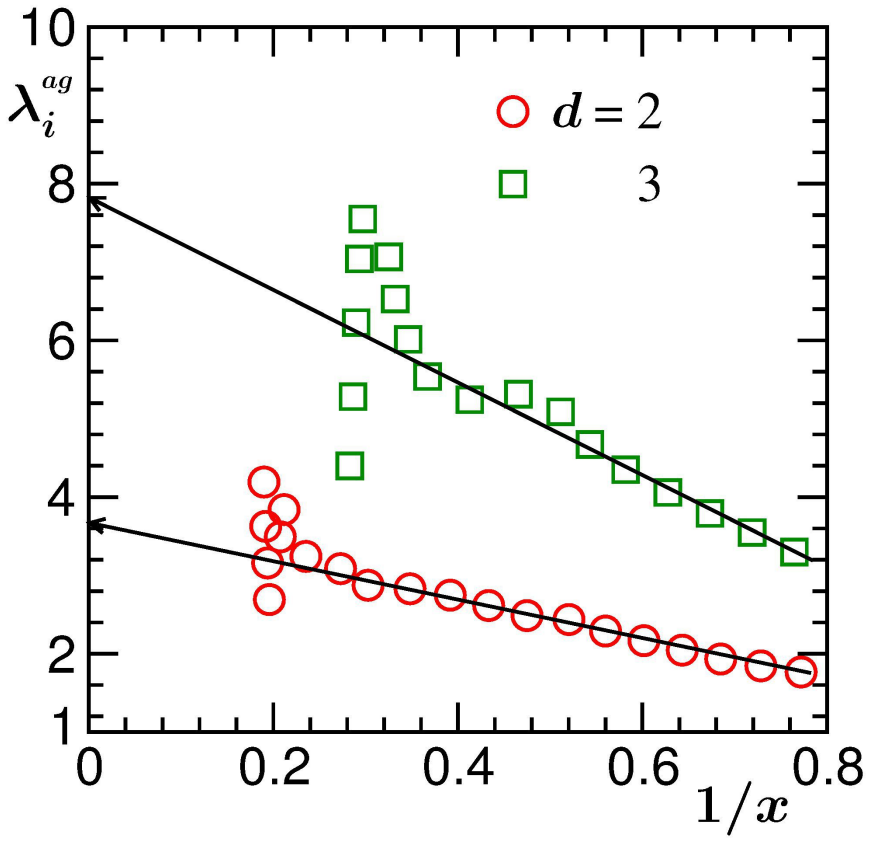

Figure 6.6: Instantaneous exponents λ_i^{ag} are plotted vs $1/x$, in both $d = 2$ and 3. The solid lines are guides to the eye. The $d = 2$ data are for $t_w = 5 \times 10^3$ with $L = 400$. In $d = 3$ the numbers are 10^3 and 200.

10^4. For $L = 200$ we have used two different t_w values, viz., 10^4 and 5×10^3. A similar exercise for the $d = 3$ CH data is presented in Fig. 6.8. In this case we have fixed t_w and varied only L. Again the data collapse looks quite reasonable and was obtained for $A_c = 5.1$ and $\lambda^{ag} = 7.30$. The value of t_w, in this case, was set to 10^3. The reason behind choosing smaller value of t_w in $d = 3$, than in $d = 2$, is computational difficulty. It is extremely difficult to accumulate data for further decades in time, starting from very high value of t_w, particularly in $d = 3$. Nevertheless, this chosen value of t_w falls within the

scaling regime. As already mentioned, for similar temperatures, amplitude of growth is larger in $d = 3$ and the scaling of $C(t, t_w)$ is related more closely to the value of ℓ_w.

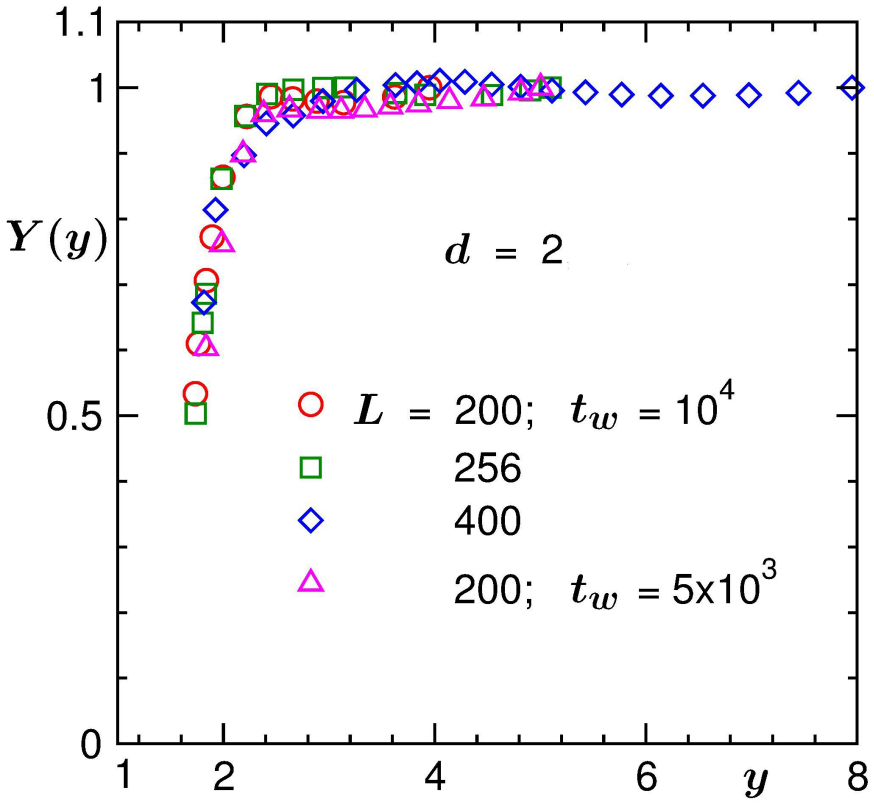

Figure 6.7: Finite-size scaling plot of $C(t, t_w)$ for $d = 2$ CH model. The scaling function Y is plotted vs y, using data from different system sizes and t_w values. The optimum collapse of data, the presented one, was obtained for $\lambda^{ag} = 3.47$.

The scaling of $C(t, t_w)$ has also been studied [28] for conserved Ising model in $d = 2$ and 3. There it is observed that, unlike the CH model, the scaling starts for large t_w values and data exhibit stronger statistical fluctuations (because of lack of coarse-graining in space and time). Despite these, it is shown that the decay of $C(t, t_w)$ follows a power-law, at late time, as a

function of x. In this case, various methods of analysis provided $\lambda^{ag} \simeq 3.60$ and $\simeq 7.30$ in $d = 2$ and 3, respectively. These values are in agreement with the ones obtained for the CH model.

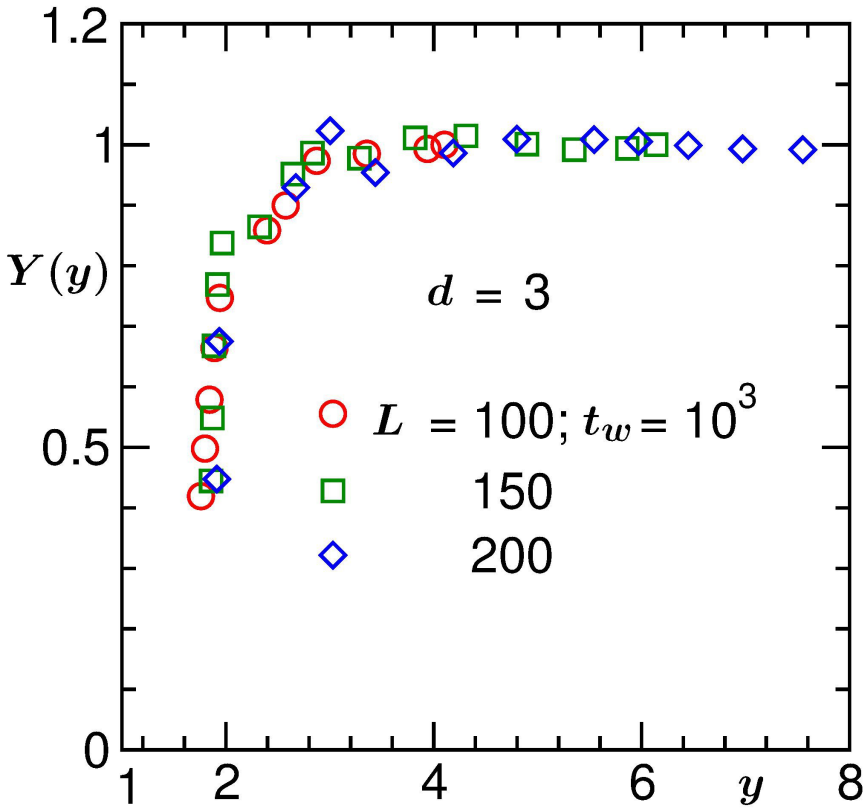

Figure 6.8: Same as Fig. 6.7, but for the CH model in $d = 3$. Here the value of λ^{ag} is 7.30.

In Fig. 6.9 we show plots of $C(t, t_w)\exp(A_c/x)$, from $d = 2$, on log-log scale, vs x $(= \ell/\ell_w)$. The result is consistent with the power-law with $\lambda^{ag} = 3.6$, represented by the solid line. The value of L here is much larger than the previous figures. This value of L was used with the objective of confirming the finite-size scaling conclusions (from relatively smaller systems) via brute force method. Given that the scaling starts for large t_w, range of x

is significant. As shown in the inset, the results span several decades in t/t_w.

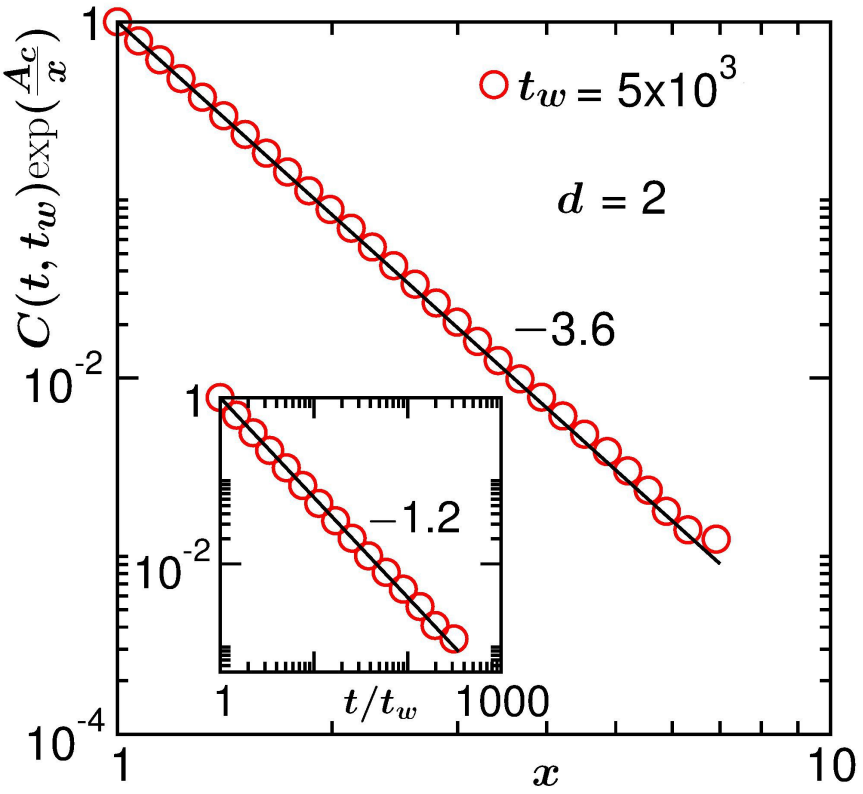

Figure 6.9: $C(t,t_w)\exp(A_c/x)$ is plotted vs x, for the $d = 2$ CH model, on log-log scale. Results from $L = 1024$ are shown. The solid line represents a power-law decay with $\lambda^{ag} = 3.6$. The inset shows the same result vs t/t_w. The solid line there has a power-law decay with exponent 1.2.

Figure 6.9 verifies that the conclusions drawn from the finite-size scaling analyses, involving smaller systems, indeed are appropriate. The exponents for the power-law decays in the main frame and the inset are consistent with each other, since $\alpha = 1/3$ (see Fig. 6.2). Analogous results from $d = 3$ CH model are shown in the Fig. 6.10. In both the Figs. 6.9 and 6.10, we have used the earliest available values of t_w for which scaling is observed. This

helps exploring reasonably large range for x, without encountering finite-size effects, i.e., ℓ being significantly smaller than L. In Fig. 6.9, e.g., data for more than two decades in t/t_w correspond to $L/\ell > 5$. This picture holds for more than a decade in t/t_w in Fig. 6.10. We note here, recently it was convincingly demonstrated [23] that finite-size effects in conserved order-parameter dynamics appear only when ℓ is as large as 3/4th of the equilibrium limit. Thus, presented results in Figs. 6.9 and 6.10 are free from finite-size effects.

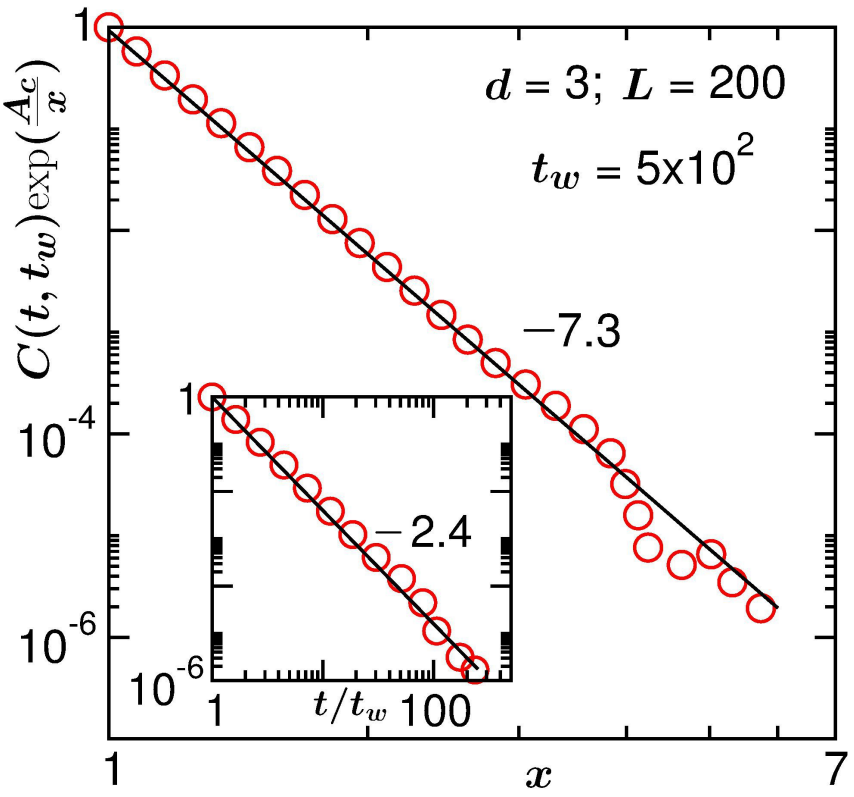

Figure 6.10: Same as Fig. 6.9 but from $d = 3$. The decay exponents for the solid lines are mentioned on the figure. In the plots we have used the values of A_c as obtained from the finite-size scaling analyses in $d = 3$.

6.4 Summary

We have studied aging dynamics for the phase separation in solid binary mixtures via Cahn-Hilliard model. Results for the two-time autocorrelation, $C(t, t_w)$, are presented from simulations in both $d = 2$ and 3. Decays of $C(t, t_w)$ appear power law in large x limit. The exponents for these power laws were obtained via various different analyses, including finite-size scaling. For the finite-size scaling analysis, full forms of the autocorrelations were essential which we obtained empirically. All these methods provide consistent values of the decay exponent λ^{ag}. These are $\lambda^{ag} \simeq 3.6$ in $d = 2$ and $\lambda^{ag} \simeq 7.5$ in $d = 3$, within 5% error. To construct a dimension dependent expression for λ^{ag}, one needs to study the phenomena in more dimensions. In this context, in $d = 1$ one should exercise the caution that β' $(= 2)$ has a different value [29].

Bibliography

[1] *Kinetics of Phase Transitions*, edited by S. Puri and V. Wadhawan (CRC Press, Boca Raton, 2009).

[2] R.M.Z. dos Santos and A.T. Bernardes, Phys. Rev. Lett. **81**, 3034 (1998).

[3] M. Costa, A.L. Goldberger and C.-K. Peng, Phys. Rev. Lett. **95**, 198102 (2005).

[4] D.S. Fisher and D.A. Huse, Phys. Rev. B, **38**, 373 (1988).

[5] G.F. Mazenko, Phys. Rev. B **42**, 4487 (1990).

[6] F. Liu and G.F. Mazenko, Phys. Rev. B **44**, 9185 (1991).

[7] C. Yeung, M. Rao and R.C. Desai, Phys. Rev. E **53**, 3073 (1996).

[8] G.F. Mazenko, Phys. Rev. E **69**, 016114 (2004).

[9] J.F. Marko and G.T. Barkema, Phys. Rev. E **52**, 2522 (1995).

[10] S. Puri and D. Kumar, Phys. Rev. Lett. **93**, 025701 (2004).

[11] S. van Gemmert, G.T. Barkema and S. Puri, Phys. Rev. E **72**, 046131 (2005).

[12] S. Ahmad, F. Corberi, S.K. Das, E. Lippiello, S. Puri and M. Zannetti, Phys. Rev. E **86**, 061129 (2012).

[13] S. Majumder and S.K. Das, Phys. Rev. Lett. **111**, 055503 (2013).

[14] J. Midya, S. Majumder and S.K. Das, J. Phys.: Condens. Matter, **26**, 452202 (2014).

[15] B. Abou and F. Gallet, Phys. Rev. Lett. **93**, 160603 (2004).

[16] G.G. Kenning, G.F. Rodriguez and R. Orbach, Phys. Rev. Lett. **97**, 057201 (2006).

[17] L. Berthier, Phys. Rev. Lett. **98**, 220601 (2007).

[18] E. Buchbinder and J.S. Langer, Phys. Rev. E **83**, 061503 (2011).

[19] J. Bergli and Y.M. Galperin, Phys. Rev. B **85**, 214202 (2012).

[20] A.J. Bray, Adv. Phys. **51**, 481 (2002).

[21] D.A. Huse, Phys. Rev. B, **34**, 7845 (1986).

[22] J.G. Amar, F.E. Sullivan and R.D. Mountain, Phys. Rev. B **37**, 196 (1988).

[23] S. Majumder and S.K. Das, Phys. Rev. E **81**, 050102 (2010).

[24] M.E. Fisher in *Critical Phenomena*, editedby M.S. Green (Academic Press, London, 1971).

[25] D.P. Landau and K. Binder, *A Guide to Monte Carlo Simulations in Statistical Physics*, Cambridge University Press, 3rd Edition (2009).

[26] A. Onuki, *Phase Transition Dynamics* (Cambridge University Press, Cambridge, 2002).

[27] K. Binder, S. Puri, S.K. Das and J. Horbach, J. Stat. Phys. **73**, 182 (1994).

[28] J. Midya, S. Majumder and S.K. Das, Phys. Rev. E **92**, 022124 (2015).

[29] S.N. Majumdar, D.A. Huse and B.D. Lubachevsky, Phys. Rev. Lett. **138**, 51 (2010).